Physical and Space Geodesy
Kluyverweg 1
2629 HS Delft
The Netherlands
http://www.lr.tudelft.nl/psg

PSG-2012-1370340

M.Sc. Thesis

A Sensitivity Study into Strapdown Airborne Gravimetry

Pedro Inácio B.Sc.

Abstract

Airborne gravimetry is an important tool for the geodesy and geophysics communities. Able to provide medium to high-resolution measurements over large areas, it is the link between the low-resolution satellite measurements and expensive terrestrial campaigns, especially in remote areas. To explore the potential of airborne gravimetry, the Gravimetry using Airborne Inertial Navigation (GAIN) project was recently established at the faculty of Aerospace Engineering at TU-Delft, and is currently building and testing an in-house strapdown airborne gravimetry system with the objective of providing low-cost, high-accuracy gravity data for use in a wide range of applications in geodesy and geophysics. Within this thesis, the inertial sensors that will be used within the GAIN strapdown IMU are calibrated and modeled with a simulator to predict the accuracy of the airborne system when completed. A sensitivity study of several campaign parameters is done to understand which parts of the hardware and operating conditions are critical to the performance of the system.

Of the list of applications for airborne gravity data, natural resource exploration is one of the more demanding in terms of accuracy and resolution, with a requirement of 0.5-2 mGal at 2 km resolution. This is beyond the range of current strapdown systems, so in addition to assessing the performance of the current strapdown system, additional tests were made to see what would be needed to achieve this higher level of accuracy.

The simulation results suggest that the performance of the GAIN strapdown system, under ideal conditions, would be 1.4 mGal at 2 km resolution. Furthermore, the performance is limited by the accelerometers whose accuracy must improve by a factor of three before the 0.5 mGal level can be achieved; however, other options were identified that could also be used to achieve this.

A Sensitivity Study into Strapdown Airborne Gravimetry

Thesis

submitted in partial fulfillment of the
requirements for the degree of

Master of Science

in

Aerospace Engineering

by

Pedro Inácio B.Sc.
born in Santa Maria da Feira, Portugal

This work was performed in:

Physical and Space Geodesy Group
Department of Remote Sensing
Faculty of Aerospace Engineering
Delft University of Technology

Delft University of Technology

Delft University of Technology
Department of
Remote Sensing

The undersigned hereby certify that they have read and recommend to the Faculty of Aerospace Engineering for acceptance a thesis entitled **"A Sensitivity Study into Strapdown Airborne Gravimetry"** by **Pedro Inácio B.Sc.** in partial fulfillment of the requirements for the degree of **Master of Science**.

Dated: 27th August 2010

Chairman: _____
Prof.dr.ir.habil. R. Klees

Advisor: _____
Dr. B.C. Gunter

Committee Members: _____
Dr.ir. E. Schrama

_____

Abstract

Airborne gravimetry is an important tool for the geodesy and geophysics communities. Able to provide medium to high-resolution measurements over large areas, it is the link between the low-resolution satellite measurements and expensive terrestrial campaigns, especially in remote areas. To explore the potential of airborne gravimetry, the Gravimetry using Airborne Inertial Navigation (GAIN) project was recently established at the faculty of Aerospace Engineering at TU-Delft, and is currently building and testing an in-house strapdown airborne gravimetry system with the objective of providing low-cost, high-accuracy gravity data for use in a wide range of applications in geodesy and geophysics. Within this thesis, the inertial sensors that will be used within the GAIN strapdown IMU are calibrated and modeled with a simulator to predict the accuracy of the airborne system when completed. A sensitivity study of several campaign parameters is done to understand which parts of the hardware and operating conditions are critical to the performance of the system.

Of the list of applications for airborne gravity data, natural resource exploration is one of the more demanding in terms of accuracy and resolution, with a requirement of 0.5-2 mGal at 2 km resolution. This is beyond the range of current strapdown systems, so in addition to assessing the performance of the current strapdown system, additional tests were made to see what would be needed to achieve this higher level of accuracy.

The simulation results suggest that the performance of the GAIN strapdown system, under ideal conditions, would be 1.4 mGal at 2 km resolution. Furthermore, the performance is limited by the accelerometers whose accuracy must improve by a factor of three before the 0.5 mGal level can be achieved; however, other options were identified that could also be used to achieve this.

Acknowledgments

I would like to thank my supervisor Dr. B.C. Gunter for his support, patience and availability during the work and writing of this thesis. I would like to also thank Dr. Q.P. Chu, R. Reudink, A. Muis, Ir. F. Postema and Ir. P. Buist for their knowledge, support and direct or indirect involvement in the work presented in this thesis. I would like to extend my gratitude to Prof.dr.ir.habil. R. Klees and Dr.ir. E. Schrama for their contribution and involvement in my graduation.

On a personal note, I would like to thank my parents, Ana Miragaia and José Inácio, my brother and all my family for their infinite care, love and support at all times.

Finally I thank my girlfriend and all my friends who have eased my most difficult moments and with whom I share so many unforgettable moments in these last years of my academic life.

Obrigado!

Pedro Inácio B.Sc.
Delft, The Netherlands
27th August 2010

Contents

List of Figures

List of Tables

Nomenclature

A/D	Analog-to-Digital
C&S	Control and Simulation
CHAMP	Challenging Minisatellite Payload
CoM	Centre of Mass
DCM	Direction Cosine Matrix
DGPS	Differential Global Positioning System
DORIS	Doppler Orbit determination and Radiopositioning Integrated on Satellite
ECEF	Earth Centered Earth Fixed Frame
FOG	Fiber-Optic Gyroscope
GAIN	Gravimetry using Airborne Inertial Navigation
GAST	Greenwich Apparent Sidereal Time
GOCE	Gravity field and steady-state Ocean Circulation Explorer
GPS	Global Positioning System
GRACE	Gravity Recovery and Climate Experiment
GRS80	Geodetic Reference System 1980, a widely used model used to approximate the size, shape and gravity field of the Earth
ICRS	International Celestial Reference Frame
IERS	International Earth Rotation and Reference Systems Service
IMU	Inertial Measurement Unit
INS	Inertial Navigation System
ITRF	International Terrestrial Reference System
L&R	Aerospace Faculty of the Technical University of Delft
LAMBDA	Least Squares Ambiguity Decorrelation Adjustment
LLR	Lunar Laser Ranging
mas	milliacrsecond, angular unit equivalent to $1/60/60/1000^\circ$.
mGal	milliGal, acceleration unit defined as: $1\,\text{mGal} \equiv 1\times10^{-5}\,\text{m/s}^2$
PSD	Power-Spectral Density
RISG	Rotation Invariant Scalar Gravimetry
SINS	Strapdown Inertial Navigation System
SISG	Strapdown Inertial Scalar Gravimetry

SLR	Satellite Laser Ranging
ZUPT	Zero Velocity Update

1 Introduction

The gravity field of the Earth is not constant; it is complex and varies from point to point over the Earth's surface. The most visible effect of this is caused by the flattening of the Earth (due to rotation) causing the polar regions to experience a higher gravitational pull as they are nearest to the center of the Earth. However, smaller and more localized variations of the gravity field exist, reflecting the Earth's morphology, topography, hydrology, ice masses and every phenomenon that involves movement of masses. The link between mass-distribution and the gravity field of the Earth is what makes its determination so valuable to the scientific community.

To study the gravity field one must first be able to represent it in a mathematical model. The concept of *spatial frequency* often arises in the domain of gravity field modeling. The concept of frequency is normally applied to signals that extend over the time domain; any signal in the time domain can be expressed as the sum of all the frequencies that compose it, where each frequency corresponds to a sinusoid extending over a certain period of time. The same analogy can be applied to describe Earth's gravity field, but now using this concept of spatial frequency; the gravity field extends over the surface of the Earth (and not over time) and it can be divided into independent frequency components each corresponding to a sinusoid that extends over a certain surface length, or wavelength. When talking about spatial frequencies of the gravity signal it is common to use the *half-wavelength* measure because it is roughly equivalent to the spacing between observations required to observe this frequency. For example, if a grid of gravity measurements is uniformly spaced with 5 Km interval, than the maximum half-wavelength observable from such dataset corresponds to roughly 5 Km. The maximum half-wavelength that can be observed is also called *resolution*. In this thesis the terms *low-frequency*, *medium-frequency* and *high-frequency* are directly related to the gravity field of the Earth and refer to spatial resolutions above 150 km, 5 to 150 km and below 5 km respectively.

For many applications in the Earth sciences, accurate knowledge of the gravity field can be used to determine both the shape (i.e., heights) and sub-surface properties (densities, mass transport, etc.) of a region. Oddly enough, the intuitive concept of height is interlaced with the gravity field of the Earth. The geoid is the equipotential surface of the gravity field which most closely follows the mean sea level and it is used as a height reference in many different applications; it is used to precisely determine the orbits of satellites, in the unification of countries' height reference systems, in inertial navigation and precise attitude determination, sea level monitoring and leveling by Global Positioning System (GPS). Each of

these applications have different requirements in the accuracy of the known geoid (Bruton, 2000). For local and regional geoid calculation, the requirements in the knowledge of the local gravity field can be placed at 2 mGal (1 mGal $= 1\times10^{-3}$ Gal, where 1 Gal $= 1\times10^{-2}$ m/s^2) accuracy for spatial resolutions of 5-14 Km (Kennedy, 2002). Any change in the gravity field with time can be directly attributed to any mass-transport phenomenon and, if continuous measurements of the gravity field are made at different time epochs, then one can begin to monitor the evolution of ice masses, ground water and tectonics. The requirements for these applications are placed at 1-3 mGal with a spatial resolution of 5-10 Km (Kennedy, 2002). One of the more demanding applications in geophysics involves natural resources exploration. Typical gravity field accuracy requirements for petroleum and gas exploration range from 0.5-2 mGal at 1-2 Km half-wavelengths (Kennedy, 2002).

Global models of the gravity field exist, which have been computed from many years of data from various sources (e.g., satellite laser ranging (SLR) data or radar altimetry of the sea surface) and more recently from three gravity dedicated missions, Challenging Minisatellite Payload (CHAMP) in 2000, Gravity Recovery and Climate Experiment (GRACE) in 2003 and the recently launched Gravity field and steady-state Ocean Circulation Explorer (GOCE) in 2009 (Rummel et al., 2002) all of them still collecting measurements. Satellite data provides global coverage but, signal strength, especially in the higher frequencies, is seriously attenuated with increasing height and therefore dedicated satellites are confined to improve the knowledge over the long wavelengths (Rummel, 2003). Ground measurements (i.e., single-point observations), with a very high accuracy are capable of measuring the high-resolution features of the geoid but campaigns are very expensive and hard to perform in remote and inaccessible locations. This is where airborne gravimetry comes in.

Airborne gravimetry is the act of measuring the gravity signal from onboard an aircraft. It is the link between satellite measurements and ground measurements. It combines the advantage of being cheaper than ground measurements and more accurate that satellite data in the medium to high-frequency part of the gravity spectrum. For these reasons, airborne gravimetry is an important tool to effectively measure relatively large regions that may be difficult to access, e.g., Greenland.

Low and medium-frequency resolution is most relevant for geodesy applications where the shape of the Earth and its gravity field are of interest, while the medium and high-frequency part of the spectra are of interest in geophysics to resolve and characterize sub-terrain features. The most stringent requirements are placed by resource exploration, and if these are met by airborne gravimetry, then all other applications are automatically enabled.

Traditional gravimetry is done with very precise accelerometers, very precisely aligned at the surface of the Earth. An accelerometer can be thought of a spring-mass system inside a casing. Whenever a force comes into *contact* with the casing, the inertia of the proof mass will deform the spring, and the deformation of the spring is a direct measurement of the force acting on the accelerometer. An illustration of an accelerometer is given in Figure 1.1. Consider an accelerometer

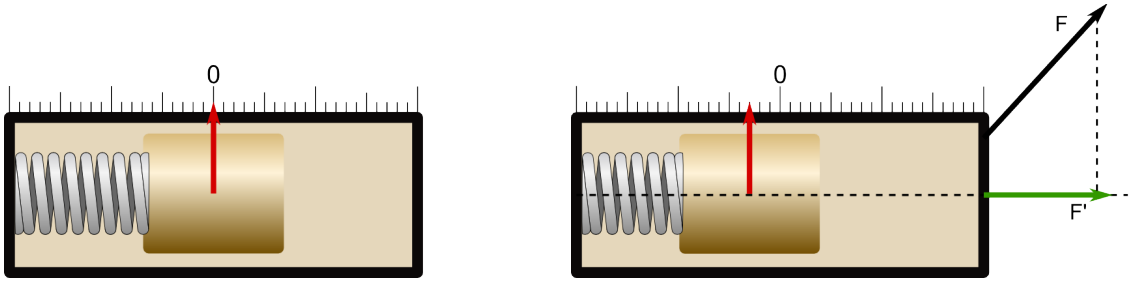

(a) (b)

Figure 1.1: Illustration of an accelerometer. In (a) no forces act on the casing and the elastic deformation is null. In (b) the component of the force acting on the sensitive axis of the instrument, $\mathbf{F}'$, deflects the spring-mass system.

in the inertial frame, or i-frame, whose equation of motion can be written using Newton's 2$^{\text{nd}}$ Law in the inertial frame[1] (Schwarz and Li, 1997).

$$m\frac{\mathrm{d}\mathbf{r}^2}{\mathrm{d}t^2} = m\ddot{\mathbf{r}} = \mathbf{F} + m\mathbf{g}(\mathbf{r}) \tag{1.1}$$

Where,

- $\mathbf{r}$ – the position of the proof mass in the i-frame.
- m – the mass of the proof-mass.
- $\mathbf{F}$ – the sum of all the contact forces acting in the accelerometer casing.
- $\mathbf{g}$ – the gravitational acceleration at the position of the proof mass.

Defining the specific force measured by the accelerometer $\mathbf{f} \equiv \frac{\mathbf{F}}{m}$ one can write,

$$\ddot{\mathbf{r}} = \mathbf{f} + \mathbf{g}(\mathbf{r}) \tag{1.2}$$

and finally,

$$\mathbf{f} = \ddot{\mathbf{r}} - \mathbf{g}(\mathbf{r}) \tag{1.3}$$

to realize that the output of the accelerometer is the sum of the kinetic acceleration of the accelerometer, $\ddot{\mathbf{r}}$, and the gravitational vector, $\mathbf{g}(\mathbf{r})$.

We then see that the forces acting on the accelerometer are divided in two types,

Specific forces f which are measured by the accelerometer. As seen in Figure 1.1 the accelerometer measures the elastic deformation of the spring. This type of forces acts in *contact* with the accelerometer casing. As the casing is accelerated, the inertia of the proof-mass causes a deformation on the spring which is then picked up by the instrument. Specific forces found onboard an airplane are, e.g., the lift exerted on the wings of the airplane or vibrations of the engines on the airplane structure.

[1] Eqn. 1.1 will be derived later in Section 2.1.1 after a proper definition of the inertial frame.

Gravitational forces g which are *not* sensed by the accelerometer. The gravitational field of the Earth acts simultaneously on the accelerometer casing and on the proof mass such that no elastic deformation is observed between both of them.

Some confusion might be clarified with the following question. Assume, for simplicity, that the Earth is not rotating and consider a static accelerometer, vertically aligned, on the surface of the Earth,

What is the specific force measured by the accelerometer?

Since it has been established that an accelerometer does not sense gravitational forces, one might be inclined to answer that the specific force measured by the accelerometer is null. This is, however, not true. In fact, the measured specific force is equal to the magnitude of the local gravity vector. The explanation for this fact lies in the subtle detail that the accelerometer in the stated conditions is not directly measuring the gravity vector, but rather the *reaction* exerted by the surface of the Earth on the accelerometer, stopping it from free-falling towards the center of the Earth.

Ground measurements of the gravity vector are very precise mostly because, by placing a static accelerometer in the surface of the Earth, $\ddot{\mathbf{r}}$ becomes constant and it becomes possible to compute $\ddot{\mathbf{r}} = \boldsymbol{\omega}_e \times \boldsymbol{\omega}_e \times \mathbf{r}$ with great precision, where $\boldsymbol{\omega}_e$ is the angular velocity of the Earth and $\mathbf{r}$ is the position of the accelerometer in the surface of the Earth. While Eqn. 1.3 works very well for a static accelerometer, it is not limited to this situation. The concept can be extended to any moving platform as long as accurate knowledge of $\ddot{\mathbf{r}}$ exists. This is generally called *moving-base gravimetry*, and airborne gravimetry is the equivalent onboard an aircraft. This has been for many years the biggest challenge in airborne gravimetry, the accurate knowledge of the aircraft's acceleration $\ddot{\mathbf{r}}$ in the inertial frame.

Notice however that using Eqn. 1.3 to compute the gravity vector $\mathbf{g}(\mathbf{r})$ requires all components of the specific force vector $\mathbf{f}$ to be measured. An accelerometer only senses the specific force component along its sensitive axis and therefore is unable to measure the full vector. This drawback is easily solved by using a triad of orthogonal accelerometers sensing all three components of the specific force vector $\mathbf{f}$.

The computation of the gravity vector through Eqn. 1.3 requires two conceptual problems to be solved:

1. The ability to express the specific force vector $\mathbf{f}$ as measured by the accelerometer triad in the i-frame frame where the equation is valid. This can be equivalently expressed as a requirement for the attitude of the accelerometer sensors relative to inertial space.

2. The separation of gravitational and non-gravitational accelerations.

Solving the attitude problem is normally tackled by using gyroscopes (i.e., 'gyros'). Gyros are inertial sensors that measure the angular velocity along its sensitive axis. One immediately sees that, by building a triad of orthogonal gyros,

the angular velocity vector $\boldsymbol{\omega}$ becomes readily available. A device that combines accelerometers and gyros, capable of measuring the angular velocities and accelerations is called an *Inertial Measurement Unit* (IMU). Typically added to an IMU is a computer system dedicated to processing the angular velocities and accelerations to obtain the kinetic state of the system, i.e., the position and velocity of the platform in a relevant frame. The combination of an IMU and onboard computer is typically called an *Inertial Navigation System* (INS). The first rudimentary INS system was applied by German rocket pioneer Wernher von Brown during the second World War for the control and guidance of the V-2 ballistic missile. Since then INS's have been continually perfected and have found applications in spacecraft, aircraft, ships, submarines, etc.

At this point it is important to realize that, as any real sensor, the considered accelerometers and gyros are not perfect instruments. An accelerometer with no specific force applied will, in general, yield measurements different than zero; the observed offset is normally called a *bias*. Furthermore the accelerometer's measurements need to be transformed into acceleration units using a so-called *scale factor*. The scale factor can be thought of as the scale of the ruler in Figure 1.1. Finally the accelerometer electronics introduce *noise* in the measurements. All of these parameters reflect the fact that the accelerometer is not a perfect instrument, and this is identically true for the gyros where the same parameters are found.

There are two to different concepts of INS systems differing on the way they handle the angular velocity measurements. The *gimbaled* or *stabilized* INS concept consists in the physical realization of the frame in which the accelerometer measurements are required. This is accomplished with a feedback of the gyro's signal into a mechanical platform which continuously aligns itself to the desired frame; any rotation sensed by the gyros is immediately counteracted by the platform where the accelerometers stand in such a way that their measurements are related to the frame of choice.

In a *strapdown* INS, or SINS, the instrument platform is fixed to the vehicle and relies on the computation of the attitude of the body using the gyro measurements. Knowing the attitude of the body frame allows the specific force measurements to be correctly transformed to the frame of choice.

In conclusion, the problem of expressing the specific for vector in the i-frame is solved by using an INS system which has the capability of rotating, either mechanically or mathematically, the specific force measurements from the body frame to the i-frame. An illustration of both principles is given in Figure 1.2

Regarding the second problem, the separation of gravitational and non-gravitational acceleration, the solution is accomplished by using an additional system which provides purely kinematic information. The difference between the specific force provided by the INS, $\mathbf{f}$, and the kinematic acceleration, $\ddot{\mathbf{r}}$, is the gravity vector, $\mathbf{g}$, as implied by Eqn. 1.3. The kinematic acceleration can be obtained by double differentiation of the position measurements done by a GPS receiver aboard the airplane. Alternatives to GPS exist, like radar-altimeters, laser-altimeters, LORAN (a terrestrial radio navigation system), etc., and have been used before GPS

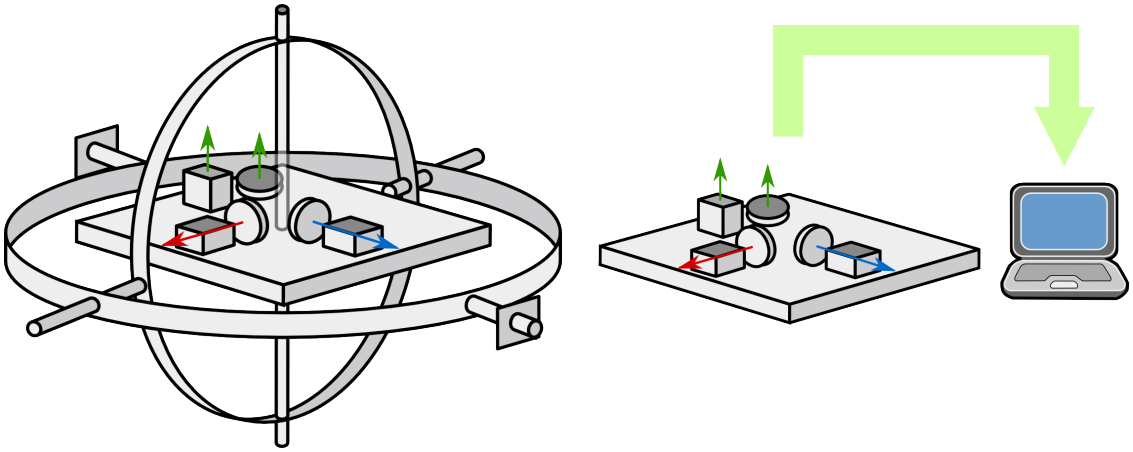

(a) Stabilized Platform (b) Strapdown INS

Figure 1.2: A stabilized platform (a) and the strapdown concept (b). Common to both are the three accelerometers and three gyroscopes orthogonally oriented.

was available, however, nowadays they lose to GPS's precision, availability and tridimensionality.

A distinction is made here between *scalar* and *vector* gravimetry. Vector gravimetry attempts to recover the full gravity vector while scalar gravimetry recovers only one of the components (normally along the vertical direction of the navigation frame, or n-frame) or the magnitude of the gravitational vector. The main advantage of vector gravimetry is that by measuring also the horizontal components of the gravity vector a more direct and precise computation of the geoid becomes possible with a much smaller survey area (Senobari, 2010). The first stabilized platforms typically contained only one very precise accelerometer which was mechanically aligned with the vertical direction of the local-level frame. These kinds of platforms do not allow vector gravimetry applications, while the strapdown concept, which requires a triad of accelerometers, inherently enables vector gravimetry.

Airborne gravimetry has been studied and tested since the 1950's with the first reported flight experiments by Nettleton et al. (1960) and Thompson and LaCoste (1960). At the time there was not enough accuracy in the navigation data to subtract the aircraft movement from the gravimeter signal. This lack of accurate navigation data has hampered attempts for many years and a number of different methods were tested until GPS became widely available. Rose and Nash (1972) attempted to use shipborne INS with navigation data from LORAN. In the early 1980's, renewed interest in airborne gravimetry was enabled by advances in the technology. Stabilized platforms were mounted on aircrafts keeping the inertial sensors fixed in the navigation frame. The main technical advantage of stabilized platforms is the dramatic reduction in the measuring range of the gyros which maximizes their performance (King, 1998). To obtain precise measurements

of the vertical acceleration, very accurate accelerometers along the vertical direction were coupled with multiple combinations of navigational aids like radar altimeters, LORAN-C, radar transponders and even the first prototypes of GPS receivers (LaCoste et al., 1982; Brozena, 1984). With the establishment of GPS, precise kinematic data was finally available and the integration of INS and GPS for airborne gravimetry immediately became the standard. According to Senobari (2010) results have been obtained at 3-5 mGal at the 10 km resolution with stabilized platforms.

Evolutions in strapdown technology, facilitated through the increasing performance of optical gyros technology (King, 1998), allowed reliable use of strapdown INS systems for airborne gravimetry. The main advantages of a SINS are mostly related to the absence of any precision mechanical parts: SINS are more reliable, cheaper and lighter. They need a lower power supply, require less maintenance and have a bigger operational flexibility. In Wei and Schwarz (1998) and Glennie and Schwarz (1999) the integration of SINS and GPS systems is shown to match the performance of their stabilized counterpart with an accuracy of 2-4 mGal at 5-7 km resolution.

The first results at vector gravimetry were published by Jekeli and Kwon (1999) with a claimed accuracy of 7-8 mGal for the horizontal components and 3 mGal for the vertical components at 10 km resolution. Li (2007) argues that the main difficulty with vector gravimetry is the strong coupling between the attitude accuracy and the errors in the horizontal accelerometers. To obtain absolute attitude observations, Mangold (1997) integrated the INS with a star tracker with the purpose of improving the attitude resolution for vector gravimetry. The latest results are described in Senobari (2010) where a wave estimator is used with a claimed accuracy of 2.4-4.2 mGal in the horizontal components at 10 km resolution. The wave estimator is an estimator where the input disturbances are modeled deterministically instead of statistically and the state vector is estimated with forward estimation and backward restoration processes within a time window.

Recall Eqn. 1.3, and for simplicity omit the dependence of the gravity vector on the position $\mathbf{g} \equiv \mathbf{g}(\mathbf{r})$. Additionally, denoting with a superscript the frame where the vectors are defined, one can write,

$$\ddot{\mathbf{r}}^i = \mathbf{f}^i + \mathbf{g}^i \tag{1.4}$$

As argued above, the specific force vector $\mathbf{f}$ is measured by a triad of accelerometers which are onboard an aircraft. Since the aircraft's attitude is different than the attitude of the inertial-frame, the measured specific force has to be appropriately rotated to the i-frame. The rotation of vectors between frames is accomplished using Direction Cosine Matrices (DCM) covered in Section 2.2. Assume that the accelerometer triad is tied to the body-frame, or b-frame (properly defined in Section 2.1.4), and consider C_b^i, the DCM that transforms any vector from the b-frame to the i-frame, one can write,

$$\ddot{\mathbf{r}}^i = C_b^i \, \mathbf{f}^b + \mathbf{g}^i \tag{1.5}$$

Solving for the gravity acceleration yields,

$$\mathbf{g}^i = \ddot{\mathbf{r}}^i - C_b^i \, \mathbf{f}^b \tag{1.6}$$

to obtain the principle of gravimetry where it is seen that the gravity vector $\mathbf{g}$ can be computed from the difference between the kinematic acceleration $\ddot{\mathbf{r}}$ and the specific force vector $\mathbf{f}$ correctly specified in the same frame.

Jekeli (2001) presents the two different approaches to the moving-base gravimetry problem. Directly using Eqn. 1.6 to compute the gravity disturbance vector is called *accelerometry* and the details of this approach are described in Section 1.2. Despite being simpler, the accelerometry approach relies on the knowledge of the kinematic acceleration $\ddot{\mathbf{r}}$ which has only become possible with the establishment of GPS technology. Previous attempts at airborne gravimetry could not provide accurate enough kinematic acceleration and the *inertial positioning* method was used instead where the gravitational vector is estimated from accumulated positioning errors. This method is described in Section 1.1.

1.1 Inertial Positioning

The inertial positioning approach relies on the difference between the position/velocity indicated by the INS and any external kinematic information, to observe the gravity vector. This is the most indirect way of computing the gravitational vector and it was the first method to be introduced at a time where no widespread kinematic measurement system, like GPS, was available.

The output of an INS system can be formalized by integrating both sides of Eqn. 1.6 yielding the velocity and position of the platform at any point in time, given some initial starting values (r_0,$\dot{r}_0$),

$$\dot{\mathbf{r}}^i_{INS}(t) = \dot{\mathbf{r}}^i_0 + \int_{t_0}^{t} C_b^i \, \mathbf{f}^b + \boldsymbol{\gamma}^i dt' \tag{1.7}$$

$$\mathbf{r}^i_{INS}(t) = \mathbf{r}^i_0 + \dot{\mathbf{r}}^i_0 (t - t_0) + \int_{t_0}^{t} \int_{t_0}^{t} C_b^i \, \mathbf{f}^b + \boldsymbol{\gamma}^i dt' dt' \tag{1.8}$$

This is the task performed by the INS onboard computer. The first step is the calculation of the C_b^i matrix from the gyro measurements and the second is the numerical integration of the forces acting on the platform. Notice that the gravity vector $\mathbf{g}^i$ is unknown to the INS system and for that reason an approximate model, i.e., the normal gravity model $\boldsymbol{\gamma}^i$, is used in the integration instead.

The difference between an external observation of the position/velocity, at time instant t_k, and the INS position/velocity is a direct observation of the errors in the INS and GPS systems and of the difference between the assumed gravity model γ and the real field $\mathbf{g}$. The observation of the error is used in a Kalman filter that simultaneously estimates the errors in the INS and the gravity disturbance vector, which is the deviation of the true field $\mathbf{g}^i$ from the assumed one $\boldsymbol{\gamma}^i$. The

Kalman filter is an optimal estimation technique especially suited to this kind of problem and more details about its role in airborne gravimetry can be found in Section 4.3.3.

Before GPS existed, one of the ways of obtaining precise observations of the kinetic state of the platform was to use **Z**ero Velocity **Up**da**t**e points or ZUPT's. ZUPT's are pre-specified points along the trajectory where the platform is held static for a short amount of time. The ZUPT's coordinates are very accurately known and, since the platform is static, the true position and velocity are completely determined. Nowadays however, GPS is available and it can be used instead of (or in parallel with) the ZUPT's to obtain accurate measurements of the kinetic state of the platform.

This method is suitable for applications where the used vehicle has the operational flexibility to stop, like a car or a helicopter, or in areas where GPS coverage is scarce (e.g., forest, city) such that an additional source of kinematic observations is required.

One of the main advantages of this method is the numerical integration of the specific force measurements which smooths the noise in the measured specific force vector.

The main disadvantage of this approach is the requirement for a stochastic model for the gravity disturbances in the Kalman filter. Whether the gravity disturbance can be interpreted as a stochastic process or not is an open discussion. The gravity field is regarded by many as a purely deterministic quantity and Jekeli (2001) states that even if the gravity field is accepted as a stochastic process, it still cannot be properly described in a linear differential equation, or as a finite-order model, as required in the Kalman filter. Another disadvantage is the instability of the INS system along the vertical channel which, unless provided with very frequent observations as given by GPS, disables the estimation of the gravity disturbance along the vertical direction.

The first demonstration of this method was carried out by Rose and Nash (1972) using LORAN observations aboard a ship. More recently Li (2007) also applies this error model with GPS kinematic position and velocities observation for a land-based vehicle.

1.2 Accelerometry

The accelerometry approach is conceptually the simplest one. It is the direct application of Eqn. 1.6. The inherent simplicity of this method is however counteracted by the noise present in the specific force and kinematic acceleration measurements. Establishing a comparison with the inertial positioning, the requirements for the noise in the measurements are much more strict with this approach. The specific forces measured by the accelerometers are no longer smoothed by the integration operation while the double differentiation of GPS positions into kinematic accelerations highly magnifies the noise present in the measurements. Many publications

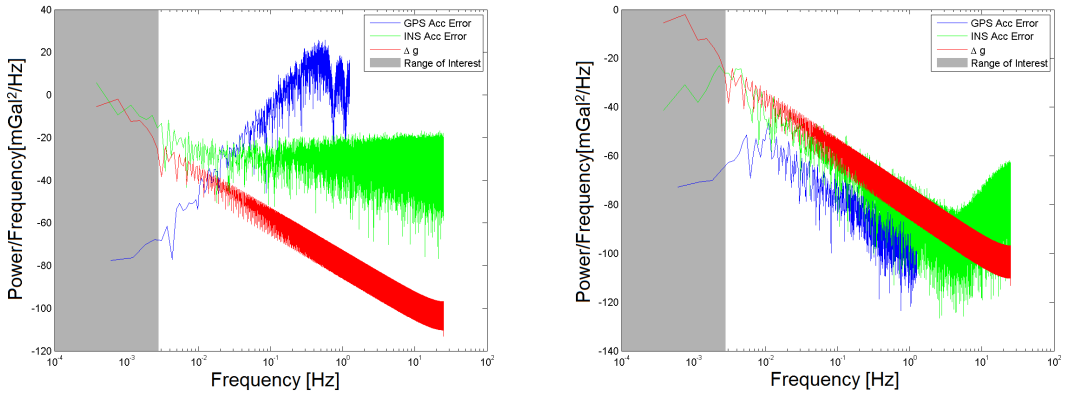

(a) (b)

Figure 1.3: Spectra of the errors in the GPS and INS measurements vs. the gravity disturbance signal. Panel (a) shows the errors in the raw measurements and panel (b) the corrected measurements.

address the determination of GPS acceleration, e.g., Kennedy (2002); Bruton et al. (1999); Jekeli and Garcia (1997), which is the critical task in the accelerometry approach.

According to Kaula's rule (Kaula, 1966) the power of the gravity field significantly decreases with spatial frequency. Most of the power is concentrated at the low frequency part of the spectrum. To effectively measure the gravity signal up to the range of interest the errors in the IMU and GPS systems have to be kept below the power of the gravity disturbance signal. In the low-frequency part of the spectrum the IMU errors are dominant due to the very static nature of the biases and scale factors present in the inertial sensors. Over the high-frequency part, the GPS errors dominate due to the double differentiation process. Also the INS errors have some energy at these frequencies due to the noise in the inertial sensors. In practice this means that only a small medium-frequency window of possibility exists for airborne gravimetry and to use it one must properly handle the errors in both measuring systems.

As a simple illustration of the noise levels involved consider the following spectrums computed from the simulations done later in this thesis. In Figure 1.3a you can compare the power spectral density (PSD) of the errors in the INS and GPS systems without any filtering vs. the gravity disturbance signal. In Figure 1.3b the same plot is show after low-pass filtering both IMU and GPS systems to remove the high-frequency errors, and after correcting the IMU for low frequency errors. The gravity disturbance signal is now stronger than the system errors within the frequency range of interest. The used low-pass filtering will be discussed later in Section 4.3.1 and the correction of the INS measurements will be discussed in Section 5.3

Even within the accelerometry approach slightly different ways of evaluating

Eqn. 1.6 can be found in the literature. Two different scalar approaches of this accelerometry method are compared in Wei and Schwarz (1998). The Rotation Invariant Scalar Gravimetry (RISG) is the accelerometric approach where no attitude information is necessary. The need for attitude information is dismissed by comparing the norm of the specific force to the norm of the kinematic acceleration. The output of this method is the magnitude of the gravitational vector and the potential advantage is the removal of the errors introduced by the gyroscopes, while tolerating the errors of all three accelerometers, which add up in the norm computation. In the Strapdown Inertial Scalar Gravimetry (SISG) approach only the vertical component of the gravity vector in the n-frame is computed. In the same publication the conclusions show that the RISG approach offers a lower level of performance than the SISG method.

Jekeli and Kwon (1999) present the first results in airborne vector gravimetry. Low pass filtering is applied to the GPS and INS measurements to reduce the high frequency noise and a wavenumber correlation filter is used to decorrelate the gravity signal from the INS system errors. In a later publication, Kwon and Jekeli (2001) use a Kalman filter, similar to the one typically used in the inertial positioning method, to estimate the low-frequency errors of the IMU. The Kalman filter observations are the differences between the INS and GPS accelerations. This publication proposes the evaluation of Eqn. 1.6 in the inertial frame, as adopted in this thesis, contrasting with previous methods where the more complex navigation frame is used to compute the gravity vector. In this publication a comparison is also done between using, or not using, a stochastic gravity model in the Kalman filter. The results were found to be slightly better when no gravity model is assumed.

1.3 The GAIN Project

In 2007, the Physical and Space Geodesy (PSG) chair at TU-Delft, in cooperation with the Mathematical Geodesy and Positioning (MGP) and Control and Simulation (C&S) groups, initiated the Gravimetry using Airborne Inertial Navigation (GAIN) project. The goal of the project is to develop, implement and operate a strapdown airborne gravimetry system capable of matching the performance of commercial airborne gravimeters both in accuracy and resolution but at a fraction of the cost. The short term goal is to develop an in-house, low-cost IMU capable of measuring data suited to all applications of airborne gravimetry. This places the accuracy requirement of system at the 0.5 mGal level at the 2 km spatial resolution. The long term goal of the project is to miniaturize the strapdown system and install it aboard unmanned aerial vehicles (UAVs). Using multiple small UAV's equipped with this miniaturized system would result in cheaper, simpler and faster airborne gravimetry surveys compared with the more complex logistics involved in any current airplane/helicopter surveys.

While several well-known commercial strapdown INS systems are available on the market, building an in-house IMU is motivated by the fact that commercial

INS's, besides being more expensive, do not allow the retrieval of raw data from the inertial sensors. The output of the system is filtered with proprietary algorithms suited for inertial navigation applications. Much more will be learned in the construction and calibration of the IMU and the access to the raw instrument data allows the development and benchmarking of different algorithms aimed at airborne gravimetry.

The GAIN project makes use of the Cessna Citation II airplane partially owned and operated by the aerospace (L&R) faculty, and which is equipped with a triad of GPS antennas capable of providing measurements of the airplane's in-flight attitude. This is one of the innovations being developed in the context of airborne gravimetry. Solving the attitude of the airplane involves computing two baselines between the three antennas mounted on the wing, nose and fuselage of the airplane. The method used in this calculation, the constrained Least Squares AMBiguitity Decorrelation Adjustment (LAMBDA) is described in Teunissen (2006), and the accuracy of the GPS attitude solutions delivered by the MGP group is better than 0.1° (Alberts et al., 2010).

The inertial sensors planned for the GAIN project include a set of recently purchased Fizoptika VG951 fiber-optic gyroscopes, three Honeywell QA3000 accelerometers, a similar (but cheaper) set of JAE Type-3 accelerometers, along with a state-of-the-art 2-axis calibration table. This hardware will be used to construct and calibrate an in-house IMU.

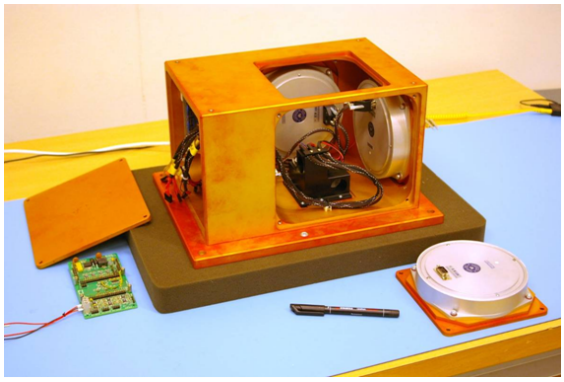

Figure 1.4: The GAIN IMU

Figure 1.5: The Cessna Citation

1.4 Statement of the Problem

The research carried out in this thesis is relevant in the context of the GAIN project, and seeks to address the following two research questions:

1. Considering the purchased inertial sensors and under ideal conditions, what is

the expected level of performance of the GAIN strapdown airborne gravimetry system?

2. What improvements are necessary to achieve the 0.5 mGal accuracy at 2 km resolution, that will enable all current applications of airborne gravimetry data?

These questions are relevant in the context of the GAIN project, because as the IMU is being built, the work done in this thesis will quantify the performance level one can expect from the system in development and it will allow us to understand where improvements are necessary to achieve the accuracy goal of 0.5 mGal at 2 km wavelength required for applications such as petroleum exploration.

To answer these questions a model of the complete strapdown system is implemented and, through simulations, the accuracy level of the system is estimated. The inertial sensors that will be used in the IMU are calibrated in this thesis to estimate their overall level of performance and error behavior. The gyros are calibrated with the recently purchased rate table at the L&R faculty. The accelerometers availability was severely delayed within the time span of this thesis and for that reason only a limited calibration of them was performed. The performance of the GPS system is estimated by personal communication with the MGP experts in the field here at the L&R faculty. All of the knowledge gathered about each component of the strapdown/DGPS system is then transported to the simulations domain where an estimate of the performance can be obtained. Simulated flights are made where the corresponding data measured by the IMU and GPS systems is created. This data is made realistic by adding errors similar to the ones expected from the real instruments and these noisy measurements are then processed, using the appropriate techniques, into gravity disturbance vectors along the flight path. The differences between the "real" gravity anomaly and the computed one will provide an estimate of the overall performance level of the system.

Expected improvements in the GPS solutions such as the GPS Block III satellites and the European Galileo constellation and possible improvements in inertial sensor technology will determine the evolution of the strapdown system over the next few years. This motivates the sensitivity study that was also carried out, where the accuracies of each component (accelerometers, gyros, GPS) are varied and the limiting factors of the system's accuracy are identified. Any future improvements in the GPS and/or inertial sensors can be mapped into the corresponding improvement of the strapdown system with this sensitivity study.

An additional advantage of the implemented simulator is that it allows further studies about the behavior of the system regarding the various parameters that involve any campaign without actually performing an expensive flight campaign. Another consequence of the simulator, is that as soon as a real campaign has been completed it can be processed within the software implemented in this thesis. Many improvements might be necessary until this is possible but the groundwork has been already laid out.

While the validity of the results might be deemed too optimistic because any simulated environment is always a simplification of reality, it was at all times ensured that the maximum level of realism is kept through the simulator and that every simplification made is clearly stated in this report. The results are then subject to all the simplifications made, and therefore they represent the lower bound of the system's accuracy, the best performance that one can expect under ideal conditions.

An overview has been given about the two main methods used in airborne gravimetry: inertial positioning and accelerometry. While both of the methods have been implemented (their underlying models are very similar), it was seen that the accelerometry approach is simpler, faster and easier to obtain results with; there are less numerical integrations and the Kalman filter becomes smaller and easier to tune. For that reason the accelerometry approach has been used in the results presented in this thesis.

Within the Kalman filter used in the accelerometry approach a choice has to be made whether a gravity model is used or not. The alternative of not using any model is seen in Kwon and Jekeli (2001) where the author recovers the gravity anomalies from the Kalman filter residuals. The advantages of using a stochastic model within the Kalman filter are that by estimating the gravity disturbances this signal will not interfere with other parameters' estimation as might happen when no model is used. Using a model also provides statistical information about the estimated gravity disturbance which does not happen in the alternative. However, using a model of the gravity field increases the number of parameters to be estimated within the Kalman filter resulting in a bigger model, making it slower to iterate and very hard to tune. Furthermore, as pointed out before, the gravity signal cannot be formally expressed in a suitable way inside the Kalman filter and imposing a certain expected model can deteriorate the results; Jekeli (1994) shows the estimation of the gravity field to be sensitive to the chosen model and in Kwon and Jekeli (2001) poorer results are obtained when using typical gravity models than when using no model. From the above discussion it is argued that the advantages of the no-model approach are stronger and this is the choice made in this thesis.

In this report a comprehensive introduction to the mathematical tools relevant to airborne gravimetry is given in Chapter 2. In Chapter 3 the calibrations of the inertial sensors are reported and an error model is built describing the errors in the used inertial sensors. In Chapter 4 an overview of the implemented software is provided and in Chapter 5 the results of several simulations are shown. Finally, in Chapter 6 the conclusions of this thesis are gathered and some recommendations for future work are made.

2 Background Information

In this chapter the mathematical principles behind the concepts of airborne gravimetry will be illustrated. Several topics will be approached, many of which the reader might already be familiar with. In the following sections the following topics will be elucidated,

- Reference frames relevant to airborne gravimetry.
- Rotations and transformations between frames.
- Numerical differentiation.
- Numerical integration.
- Linear perturbations.

2.1 Reference Frames

2.1.1 The *i*-frame

The inertial frame, or i-frame, considered throughout this work is based on the International Celestial Reference System, ICRS (2010). The ICRS defines the International Celestial Reference Frame (ICRF) as a cartesian right-handed system located at the barycenter of the solar system where,

- z-axis points towards the celestial sphere pole;
- x-axis direction is along the celestial equator in a direction fixed by the mean right ascension of 23 quasars at the time of creation of the ICRF.
- y-axis such that the three axes define a right-handed orthogonal cartesian system.

The current realization of the ICRF is maintained by the International Earth Rotation and Reference Systems Service (IERS), which continuously measures the positions of distant stars and quasars to keep the ICRF fixed relative to inertial space (read distant stars and quasars) within $\pm\,20\,\text{mas}$, or milliarcsecond defined as $1/3.6{\times}10^6\,^\circ$. More details about the ICRF can be found in ICRS (2010).

The i-frame used throughout this report can then be defined as a shifted version of the ICRF placed at the center of mass of the Earth.

In a Newtonian sense, an inertial frame is defined as a reference frame where Newton's 1^{st} Law is valid. It states,

> In the absence of force, a body either remains at rest or moves in a straight line with constant speed.

In the light of this, the defined i-frame in fact, *not* an inertial frame. Any body placed at rest in the proximity of the Earth, with no forces applied, will gradually accelerate towards the center of mass, thus violating Newton's 1st Law. The gravitational acceleration experienced by the body is not the result of a physically applied force but rather the result of the Earth's gravitational *field* (Jekeli, 2001). In practice this means that Newton's Laws have to be modified to be valid in this *pseudoinertial* i-frame.

Newton's 2nd Law can be written as,

$$F = \frac{d}{dt}(m\dot{\mathbf{r}}) \tag{2.1}$$

Without any loss of generality, one can assume that the mass remains constant,

$$F = m\ddot{\mathbf{r}} \tag{2.2}$$

In the i-frame Eqn. 2.2 is then modified to include the gravitational acceleration $\mathbf{g}$,

$$m_g\,\mathbf{g}(\mathbf{r}) + \mathbf{F} = m_i\,\ddot{\mathbf{r}} \tag{2.3}$$

where,

m_g – is the gravitational mass
m_i – is the inertial mass

Using the Weak Principle of Equivalence, both kinds masses are assumed to be equal and one can simplify Eqn. 2.3, defining the *specific force* $\mathbf{f} = \frac{\mathbf{F}}{m}$,

$$\ddot{\mathbf{r}} = \mathbf{f} + \mathbf{g}(\mathbf{r}) \tag{2.4}$$

Eqn. 2.4 is Newton's 2nd Law in the considered i-frame. It can be applied to describe the movement of any of any body in the inertial frame and applying it to the movement of an accelerometer is the concept behind moving-base gravimetry.

2.1.2 The *e*-frame

The e-frame is defined by the International Terrestrial Reference System (ITRS), and is more commonly known as Earth Centered Earth Fixed (ECEF) frame. The e-frame is realized by locating the center of mass (CoM) of the Earth and by measuring its rotation in inertial space with the help of satellite laser ranging (SLR), GPS, very long baseline interferometry (VLBI), lunar laser ranging (LLR) and Doppler Orbit determination and Radiopositioning Integrated on Satellite (DORIS) measurements taken by various centers distributed around the world IERS (2010). The frame is further adjusted with a no-net-rotation condition which corrects for tectonic motions on the surface of the Earth.

The origin of the e-frame is then at the center of mass of the Earth,

- z-axis coincides with the mean polar axis, close to the Earth's spin axis.
- x-axis points towards the intersection of the mean Greenwich meridian and the equatorial plane.
- y-axis such that the three axes define a right-handed orthogonal cartesian system.

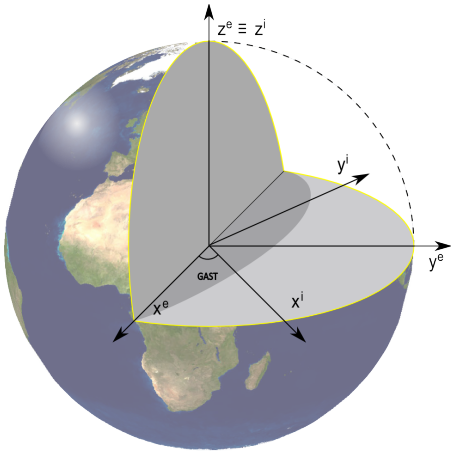

Figure 2.1: Illustration of the e-frame and the relation with the i-frame.

The angle between the e-frame and the i-frame is called Greenwich Apparent Sidereal Time (GAST) and it is the angle between the Greenwich Meridian and the xz-plane of the i-frame.

2.1.3 The n-frame

The navigation frame, or n-frame, is one of the frames commonly used to express the navigation of a vehicle. It is also known as a *local-coordinate* frame or *local-level* frame which stems from the fact that its orientation depends on the vehicle's current position and hence it has a local nature.

The starting point towards the definition of the n-frame is the geodetic reference system. The geodetic reference system defines an ellipsoid of revolution which is shaped to be as close as possible to the Earth's geoid. There are several geodetic reference systems that have been proposed throughout the years. In the following work the Geodetic Reference System 1980 (GRS80) will be used which is the internationally adopted Earth-approximating ellipsoid (Moritz, 1992).

On the reference ellipsoid a set of coordinates is defined; the geodetic latitude, ϕ, is the angle between the equatorial plane and the ellipsoidal normal which intersects the vehicle. The geodetic longitude, λ, is the angle between the Greenwich meridian plane and the local meridian plane and h is the height above the ellipsoidal surface. This orthogonal trio of coordinates in combination with the defined reference ellipsoid define the location of a point in three-dimensional (3D) space.

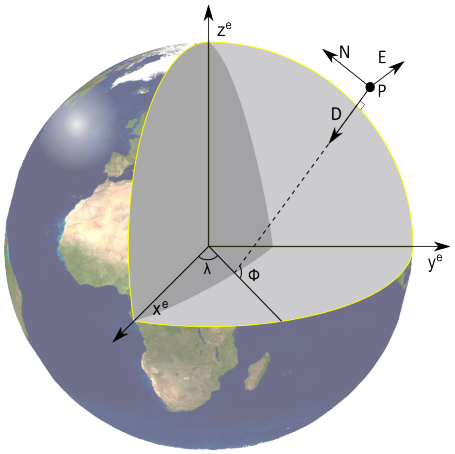

Figure 2.2: The n-frame

The origin of the n-frame is the vehicle,

- z-axis is aligned with the local ellipsoidal normal in the down direction.
- x-axis is aligned along the plane tangent to the local meridian in the North direction.
- y-axis is also defined in the tangent plane but now in the East direction.

The n-frame is depicted in Figure 2.2. Another name used to describe this frame is the NED frame because its axes point respectively towards the **N**orth, **E**ast and **D**own directions. Notice that the ellipsoidal normal does not, in general, point towards the center of the ellipsoid or analogously the center of the Earth.

The usefulness of such a frame is that the horizontal and vertical directions are decoupled into different axes for all the points on the surface of the Earth. This means that a strongly vertical phenomenon, like gravity, will be almost fully confined to the vertical axis of the n-frame.

2.1.4 The *b*-frame

The body frame, or b-frame, is defined in the vehicle to be navigated; in the case of airborne gravimetry this vehicle is an airplane. In general the body frame is defined with its origin in the CoM of the airplane or alternatively on the same location as the INS system onboard the airplane,

- x-axis is defined in the forward direction of the airplane.
- z-axis is defined vertical in the down direction.
- y-axis is such that the coordinate system becomes right-handed.

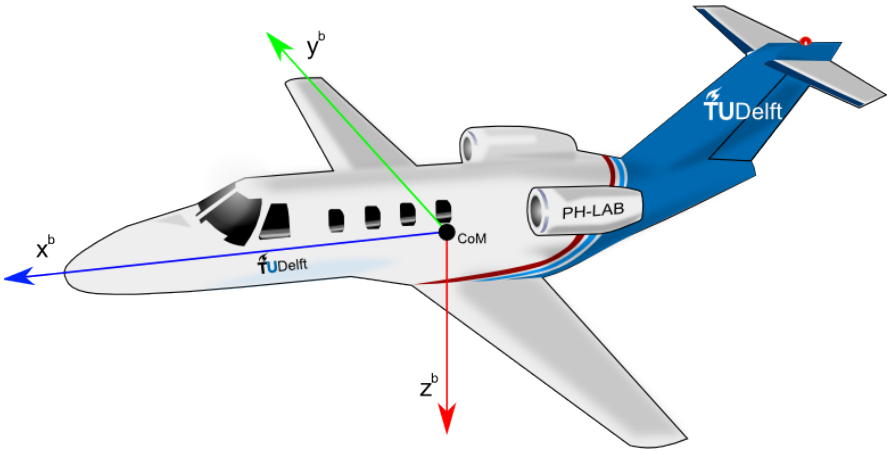

Figure 2.3: Illustration of the b-frame aboard the Cessna Citation.

The b-frame is depicted in Figure 2.3. For a real system the definition of the b-frame has to be more rigorously defined so that after a thorough calibration it becomes possible to translate the measurements taken by the inertial sensors (accelerometers and gyroscopes) from their sensitive axes to the b-frame. However the rigorous definition the b-frame in this thesis will be relaxed to the definition provided above. This is possible because we will assume that the INS system has been perfectly calibrated such that it now provides all the measurements directly in the b-frame.

All the relevant frames have been presented and the next step is to establish the framework which allows us to translate the quantities written in one frame into any of the other frames.

2.2 Frame Transformations

The relation between frames with different attitudes is of primary importance in airborne gravimetry. The attitude of a frame (relative to another one) can be expressed in many ways and the ones used throughout this thesis will be briefly discussed,

- Direction Cosine Matrices
- Quaternions
- Euler angles

Each of the techniques will be only briefly explained and the more unfamiliarized reader is referred to Jekeli (2001) where the content and notation used in the following sections is based upon.

2.2.1 Direction Cosine Matrices

A direction cosine matrix, or DCM, is simply a matrix that transforms a vector coordinatized in one frame into another frame. The matrix can be constructed in the following way.

Consider two frames, s and f, and an arbitrary vector $\mathbf{r}$ which can be appropriately written in both considered frames,

$$\mathbf{r}^s = r_x^s \mathbf{e}_x^s + r_y^s \mathbf{e}_y^s + r_z^s \mathbf{e}_z^s \tag{2.5}$$
$$\mathbf{r}^f = r_x^f \mathbf{e}_x^f + r_y^f \mathbf{e}_y^f + r_z^f \mathbf{e}_z^f \tag{2.6}$$

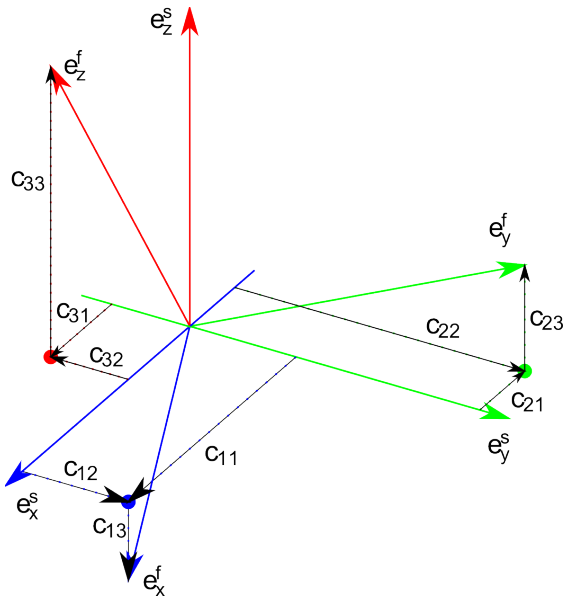

Figure 2.4: Projection of f-frame basis into the s-frame

Furthermore it is possible to write the base vectors of the f-frame in the s-frame. This is done by projecting each of the f-frame basis vectors into the s-frame basis as,

$$\begin{aligned}
\mathbf{e}_x^f &= c_{11}\mathbf{e}_x^s + c_{12}\mathbf{e}_y^s + c_{13}\mathbf{e}_z^s \\
\mathbf{e}_y^f &= c_{21}\mathbf{e}_x^s + c_{22}\mathbf{e}_y^s + c_{23}\mathbf{e}_z^s \\
\mathbf{e}_z^f &= c_{31}\mathbf{e}_x^s + c_{32}\mathbf{e}_y^s + c_{33}\mathbf{e}_z^s
\end{aligned} \tag{2.7}$$

where, e.g., c_{11} is the projection of e_x^f into e_x^s obtained as,

$$c_{11} = e_x^f \cdot e_x^s = \| e_x^f \| \| e_x^s \| \cos\alpha = \cos\alpha \tag{2.8}$$

and α is the angle between the two basis vectors. Each of the c_{ij} coefficients is represented in Figure 2.4.

Replacing Eqn. 2.7 in Eqn. 2.6 and rearranging,

$$\begin{aligned}\mathbf{r}^f = &\left(c_{11}r_x^f + c_{12}r_y^f + c_{13}r_z^f\right)\mathbf{e}_x^s \\ &\left(c_{21}r_x^f + c_{22}r_y^f + c_{23}r_z^f\right)\mathbf{e}_y^s \\ &\left(c_{31}r_x^f + c_{32}r_y^f + c_{33}r_z^f\right)\mathbf{e}_z^s\end{aligned} \tag{2.9}$$

And comparing with Eqn. 2.5 one can finally write,

$$\begin{bmatrix} r_x^s \\ r_y^s \\ r_z^s \end{bmatrix} = \begin{bmatrix} c_{11} & c_{12} & c_{13} \\ c_{21} & c_{22} & c_{23} \\ c_{31} & c_{32} & c_{33} \end{bmatrix} \cdot \begin{bmatrix} r_x^s \\ r_y^s \\ r_z^s \end{bmatrix} \tag{2.10}$$

Or using matrix notation,

$$\mathbf{r}^s = C_f^s \cdot \mathbf{r}^f \tag{2.11}$$

C_f^s is the linear transformation that rewrites an arbitrary vector from the f-frame (the lower index) into the s-frame (the upper index). Additionally C_f^s is an orthogonal matrix and the inverse transformation can be easily obtained,

$$C_s^f = (C_f^s)^{-1} = (C_f^s)^T \tag{2.12}$$

2.2.2 Euler Angles

A transformation between two frames with arbitrary attitudes can be described by 3-angles along some or all of the coordinate axes.

The elementary rotations along each axis are well known from algebra and they are written as follows,

$$R_x(\alpha) = \begin{bmatrix} 1 & 0 & 0 \\ 0 & \cos\alpha & \sin\alpha \\ 0 & -\sin\alpha & \cos\alpha \end{bmatrix} \tag{2.13}$$

$$R_y(\alpha) = \begin{bmatrix} \cos\alpha & 0 & -\sin\alpha \\ 0 & 1 & 0 \\ \sin\alpha & 0 & \cos\alpha \end{bmatrix} \tag{2.14}$$

$$R_z(\alpha) = \begin{bmatrix} \cos\alpha & \sin\alpha & 0 \\ -\sin\alpha & \cos\alpha & 0 \\ 0 & 0 & 1 \end{bmatrix} \tag{2.15}$$

When transforming a vector from one coordinate frame to another the order in which the rotations are done is not arbitrary. Therefore a set of 3-angles is meaningless until a rotation sequence is defined. There are many possible rotation sequences but the 321 (or zyx) sequence will be used as is usual in navigation applications. Under this convention the angle of rotation over the x-axis is called *roll* and is denoted as η; the *pitch*, χ, is the rotation over the y-axis and the *yaw*, α, is the rotation over the z-axis.

The transformation from the s-frame to the f-frame is the successive rotation over the 3-axis in the specified order,

$$\mathbf{r}^f = R_z(\eta)R_y(\chi)R_x(\alpha)\,\mathbf{r}^s \tag{2.16}$$

To establish a bridge between direction cosine matrices and the defined Euler angles one compares equations (2.11) and (2.16) from where it follows,

$$C_s^f = R_z(\eta)R_y(\chi)R_x(\alpha) \tag{2.17}$$

and expanding on the right hand side,

$$C_s^f = \begin{bmatrix} \cos\eta\cos\chi & \cos\eta\sin\chi\sin\alpha + \sin\eta\cos\alpha & -\cos\eta\sin\chi\cos\alpha + \sin\eta\sin\alpha \\ -\sin\eta\cos\chi & -\sin\eta\sin\chi\sin\alpha + \cos\eta\cos\alpha & \sin\eta\sin\chi\cos\alpha + \cos\eta\sin\alpha \\ \sin\chi & -\cos\chi\sin\alpha & \cos\chi\cos\alpha \end{bmatrix} \tag{2.18}$$

Equation (2.18) shows the equivalence between the DCM and the defined Euler angles notation. The inverse relationship is the following,

$$\begin{aligned} \alpha &= \tan^{-1}\left(\frac{-c_{32}}{c_{33}}\right) \\ \chi &= \sin^{-1}(c_{31}) \\ \eta &= \tan^{-1}\left(\frac{-c_{21}}{c_{11}}\right) \end{aligned} \tag{2.19}$$

2.2.3 Quaternions

A quaternion is an extension of the complex numbers in the same manner as the complex numbers are an extension of the real numbers. While a complex number can be written as $z = a + bi$ a quaternion introduces two new imaginary "axes", j and k, such that a quaternion q can be written as,

$$q = a + bi + cj + dk \tag{2.20}$$

where a,b,c and d are real numbers. Under this notation a is called the *scalar* part, while b,c and d are the *vector* part of quaternion q.

The concept of quaternions is attributed to Sir William Hamilton, who in 1843 established the following fundamental relationship of quaternion algebra,

$$i^2 = j^2 = k^2 = ijk = -1 \tag{2.21}$$

All the properties of quaternion algebra start with this equality, and despite being an interesting domain of mathematics, they will not be covered in much detail and the reader is referred to e.g., Kuipers (1999), for additional details. Relevant to

the topic of frame rotations and transformations are the definitions of quaternion multiplication and the conjugate operator.

The conjugate of a quaternion, q^*, is defined as the same quaternion q with negative vector part,

$$q^* = a - bi - cj - dk \tag{2.22}$$

The multiplication of two quaternions is derived using the distributive property of multiplication and Eqn. 2.21. Using appropriate multiplications of $ijk = -1$ the following equalities can be derived,

$$\begin{aligned} ij &= -ji = k \\ jk &= -kj = i \\ ki &= -ik = j \end{aligned} \tag{2.23}$$

Denoting the multiplication of two quaternions with the operator symbol, $\otimes$, one can write,

$$q_1 \otimes q_2 = (a_1 + b_1 i + c_1 j + d_1 k).(a_2 + b_2 i + c_2 j + d_2 k) \tag{2.24}$$

and applying the identities in Eqn. 2.21 and 2.23 to Eqn. 2.24, one can define quaternion multiplication explicitly as,

$$\begin{aligned} q_1 \otimes q_2 = \quad & (a_1 a_2 - b_1 b_2 - c_1 c_2 - d_1 d_2) \\ & + i\,(a_1 b_2 + a_2 b_1 + c_1 d_2 - c_2 d_1) \\ & + j\,(a_1 c_2 + a_2 c_1 - b_1 d_2 + d_1 b_2) \\ & + k\,(a_1 d_2 + a_2 d_1 + b_1 c_2 - c_1 b_2) \end{aligned} \tag{2.25}$$

How does all this relate to attitude and frame transformations? Quaternions can be used to transform vectors between differently oriented frames. Consider the relation between the s-frame and the f-frame as depicted in Figure 2.5. The relation between frames s and f is such that the f-frame can be obtained by rotating the s-frame along the vector $\mathbf{v}$ by an angle α.

With this in mind, the following quaternion is defined,

$$q \equiv a + bi + cj + dk = \cos\frac{\alpha}{2} + e_{v_x}\sin\frac{\alpha}{2}i + e_{v_y}\sin\frac{\alpha}{2}j + e_{v_z}\sin\frac{\alpha}{2}k \tag{2.26}$$

where $e_{v_k},\ k \in (x, y, z)$ are the components of the unit vector $\mathbf{e}_v$ defined as,

$$\mathbf{e}_v \equiv \frac{\mathbf{v}}{\parallel \mathbf{v} \parallel}$$

Notice that by definition the norm of $\mathbf{q}$ is 1,

$$\begin{aligned} \parallel \mathbf{q} \parallel &= \sqrt{a^2 + b^2 + c^2 + d^2} = \sqrt{\cos\left(\frac{\alpha}{2}\right)^2 + \sin\left(\frac{\alpha}{2}\right)^2 \left(e_{v_x}^2 + e_{v_y}^2 + e_{v_z}^2\right)} \\ \parallel \mathbf{q} \parallel &= 1 \end{aligned} \tag{2.27}$$

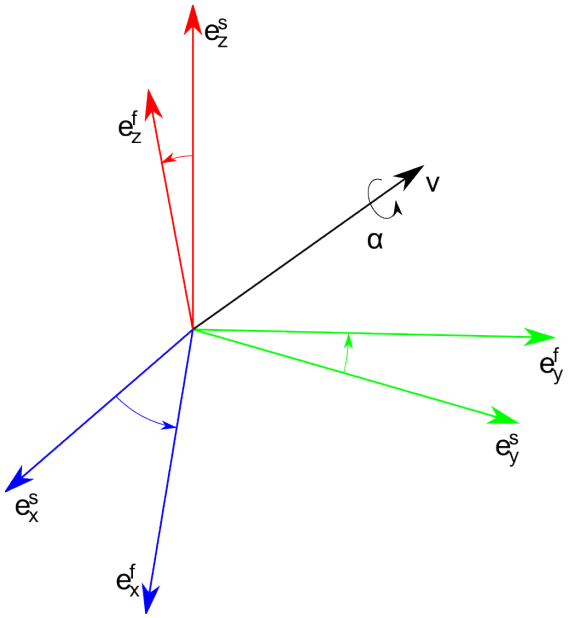

Figure 2.5: The s-frame and f-frames. The f-frame is obtained by rotating the s-frame along direction $\mathbf{v}$ by an angle α.

The final step before transforming the arbitrary vector $\mathbf{r}^s$ into the f-frame is to define a quaternion r_s whose vector part is the vector $\mathbf{r^s}$,

$$r^s = 0 + r^s_x i + r^s_y j + r^s_z k \tag{2.28}$$

The vector $\mathbf{r}^f$ can be obtained from the vector part of the quaternion r^f computed as,

$$r^f = q \otimes r^s \otimes q^* \tag{2.29}$$

To establish the relationship between the DCM and the corresponding quaternion we can replace the arbitrary vector $\mathbf{r}$ for each of the base vectors of the s-frame, $\mathbf{e}_k,\ k \in (x, y, z)$. Transforming each one of them using Eqn. 2.29 and gathering them in a matrix yields the following,

$$C^f_s = \begin{bmatrix} a^2+b^2-c^2-d^2 & 2bc-2ad & 2ac+2bd \\ 2ad+2bc & a^2-b^2+c^2-d^2 & 2cd-2ab \\ 2bd-2ac & 2ab+2cd & a^2-b^2-c^2+d^2 \end{bmatrix} \tag{2.30}$$

The inverse of this relationship is done by noticing that the trace of matrix $C \equiv C^f_s$,

$$\operatorname{tr} C = 3a^2 - b^2 - c^2 - d^2$$

using Eqn. 2.27,

$$\begin{aligned} \operatorname{tr} C + 1 &= 4a^2 \\ a &= \frac{1}{2}\sqrt{\operatorname{tr} C + 1} \end{aligned} \tag{2.31}$$

Knowing the value of a,

$$\begin{aligned} b &= \frac{1}{4a}\left(C_{2,3} - C_{3,2}\right) \\ c &= \frac{1}{4a}\left(C_{3,1} - C_{1,3}\right) \\ d &= \frac{1}{4a}\left(C_{1,2} - C_{2,1}\right) \end{aligned} \tag{2.32}$$

2.2.4 Transformation between the *i*- and *e*-frames

The e-frame is attached to the Earth and constantly rotates with it while the i-frame has a fixed attitude relative to inertial space. The angular velocity of the Earth, $\boldsymbol{\omega}_e$, is, by definition of both frames, along the z-axis. The transformation between these two frames is then accomplished by rotating along the z-axis by the appropriate angle,

$$\begin{aligned} C_i^e &= R_z(\omega_e \Delta t) \\ C_e^i &\equiv (C_i^e)^{-1} = R_z(-\omega_e \Delta t) \end{aligned} \tag{2.33}$$

where Δt is the time interval since both frames were coincident and $\omega_e = 7.2921159 \times 10^{-5}$ rad.s^{-1} is one of the defining constants of the GRS80 ellipsoid (Moritz, 1992).

2.2.5 Transformation between the *e*- and *n*-frames

The coordinates in the n-frame are the geodetic latitude ϕ, geodetic latitude λ, and height above reference ellipsoid h. This is not a cartesian coordinate set (like the e-frame) so the transformation of coordinates cannot be accomplished with a rotation of the position vector. Additional quantities that describe the considered ellipsoid have to be defined before the coordinate transformation can be applied. As mentioned in Section 2.1.3 the adopted ellipsoid is the GRS80 with the following defining constants,

$$\begin{aligned} a &= 6378137 \text{ m} \\ f &= 1/298.257222101 \end{aligned} \tag{2.34}$$

where a is the semimajor axis of the ellipsoid, and f is the ellipsoidal flattening.

The square of the ellipsoid eccentricity, e^2, is computed as,

$$e^2 = 2f - f^2 \tag{2.35}$$

and, just like the flattening term f, the eccentricity e describes how much the ellipse deviates from being circular.

The radius of curvature of the ellipsoid in the prime vertical N can be computed as in Eqn. 2.36. This is the distance along the ellipsoidal normal, from the ellipsoid surface to the polar axis.

$$N = \frac{a}{\sqrt{1 - e^2 \sin^2 \phi}} \tag{2.36}$$

The transformation between the two sets of coordinates is then given by (Jekeli, 2001),

$$\begin{bmatrix} x^e \\ y^e \\ z^e \end{bmatrix} = \begin{bmatrix} (N+h)\cos\phi\cos\lambda \\ (N+h)\cos\phi\sin\lambda \\ (N(1-e^2)+h)\sin\phi \end{bmatrix} \tag{2.37}$$

The inverse relationship is of an iterative nature and it can be written as,

$$\begin{bmatrix} \phi \\ \lambda \\ h \end{bmatrix} = \begin{bmatrix} \tan^{-1}\left(\dfrac{z^e}{\sqrt{x^{e2}+y^{e2}}}\left(1+\dfrac{e^2 N \sin\phi}{z^e}\right)\right) \\ \tan^{-1}\left(\dfrac{y^e}{x^e}\right) \\ \sqrt{x^2+y^2}\cos\phi + (z^e + e^2 N \sin\phi)\sin\phi - N \end{bmatrix} \tag{2.38}$$

The iteration is done in the ϕ equation with the starting assumption that $h = 0$ such that,

$$\phi_0 = \tan^{-1}\left(\frac{z^e}{\sqrt{x^{e2}+y^{e2}}}\frac{1}{1-e^2}\right) \tag{2.39}$$

this typically converges to the real value of ϕ in one or two iterations after which h can be computed as shown. The expression for the computation of h has a more robust form that the one presented in Jekeli (2001) as it avoids the singularity at high latitude values[1].

The transformation matrix that relates the n-frame with the e-frame is obtained in the following way,

- rotate the n-frame along the y-axis (pointing East) until the xy-plane is parallel to the equatorial plane; this happens for the angle of $\lambda + \pi/2$
- rotate this intermediate frame along the z-axis until it is oriented with the e-frame; this happens for the angle $-\lambda$

[1]This was a suggestion in the implementation notes by Rob Comer (`rob.comer@mathworks.com`) of the `ecef2geodetic` function of the Mapping Toolbox for MATLAB R2007b

Refer to Figure 2.2 for a better visualization of the sequence of rotations involved in the transformation. The transformation matrices between both frames can then be defined as,

$$\begin{aligned} C_n^e &= R_z(-\lambda)R_y(\phi + \pi/2) \\ C_e^n &\equiv (C_n^e)^{-1} = R_z(\lambda)R_y(-\phi - \pi/2) \end{aligned} \tag{2.40}$$

2.2.6 Transformation between the *b*- and *n*-frames

The b-frame relates to the n-frame by the roll, pitch and yaw angles of the platform(η, χ and α respectively). The transformation of vectors between these to frames is then accomplished simply by,

$$\begin{aligned} C_n^b &= R_z(\alpha)R_y(\chi)R_x(\eta) \\ C_b^n &\equiv (C_n^b)^{-1} = R_z(-\alpha)R_y(-\chi)R_x(-\eta) \end{aligned} \tag{2.41}$$

2.2.7 Small Angles Approximation

If an angle β is very small the following approximations are valid,

$$\cos\beta \approx 1 \tag{2.42}$$

$$\sin\beta \approx \beta \tag{2.43}$$

Consider now Eqn. 2.18 representing the DCM in terms of the Euler attitude angles. If these attitude angles are very small the matrix expression can be simplified to,

$$C_s^f = \begin{bmatrix} 1 & \eta & -\chi \\ -\eta & 1 & \alpha \\ \chi & -\alpha & 1 \end{bmatrix} = I - \Psi \tag{2.44}$$

where Ψ is the skew-symmetric matrix of the small Euler angle vector $\boldsymbol{\psi} = \begin{bmatrix} \alpha & \chi & \eta \end{bmatrix}^T$ defined as,

$$\Psi \equiv [\boldsymbol{\psi}\times] = \begin{bmatrix} 0 & -\eta & \chi \\ \eta & 0 & -\alpha \\ -\chi & \alpha & 0 \end{bmatrix} \tag{2.45}$$

2.2.8 Differential Equation of the Rotation

When considering frames that rotate with respect to each others it becomes important to be able to describe the changing attitude in terms of rotational transformations (Jekeli, 2001). Lets consider the motion of frame f relative to frame s. To do this, the derivative of the attitude matrix between s- and f-frames, $\dot{C}_s^f$, is evaluated using the definition of derivative,

$$\dot{C}_s^f = \lim_{\delta t \to 0} \frac{C_s^f(t + \delta t) - C_s^f(t)}{\delta t} \tag{2.46}$$

The attitude at time $(t + \delta t)$ can be seen as two consecutive rotations, the attitude at time t and the change in the attitude of the f-frame during time δt, δC^f, such that,

$$C_s^f(t + \delta t) = \delta C^f \, C_s^f(t) \tag{2.47}$$

Since δt is an infinitesimal amount of time, the change in the attitude is very small and δC^f can be evaluated using the small angle approximation in Eqn. 2.44 as,

$$\delta C^f = I - \Psi^f \tag{2.48}$$

Substituting in Eqn. 2.46,

$$\begin{aligned}
\dot{C}_s^f &= \lim_{\delta t \to 0} \frac{C_s^f(t + \delta t) - C_s^f(t)}{\delta t} \\
&= \lim_{\delta t \to 0} \frac{(I - \Psi^f) \, C_s^f(t) - C_s^f(t)}{\delta t} \\
&= - \lim_{\delta t \to 0} \frac{\Psi^f}{\delta t} \, C_s^f(t)
\end{aligned}$$

Since Ψ is the skew symmetric matrix of the attitude angles, $\lim_{\delta t \to 0} \frac{\Psi^f}{\delta t}$ represents an infinitesimal angular displacement over an infinitesimal amount of time which is the definition of angular velocity. This term can then be written as the skew symmetric matrix of the angular velocity vector that describes the angular velocity of f- relative to s- and coordinatized in the s-frame $\Omega_{sf}^f \equiv [\boldsymbol{\omega}_{sf}^f \times]$,

$$\dot{C}_s^f = -\Omega_{sf}^f \, C_s^f(t)$$

Using the fact that $\boldsymbol{\omega}_{sf}^f = -\boldsymbol{\omega}_{fs}^f$ the following equalities apply,

$$\Omega_{sf}^f = -\Omega_{fs}^f = -C_s^f \, \Omega_{fs}^s \, C_f^s \tag{2.49}$$

and Eqn. 2.50, known as Puasson equation (Salychev, 1998), can be written,

$$\dot{C}_s^f = C_s^f \Omega_{fs}^s \tag{2.50}$$

This is the equation that will later be used to translate the angular velocity vector measured by the IMU gyros in the b-frame, $\boldsymbol{\omega}_{ib}^b$, into the attitude of the platform relative to the inertial frame C_b^i.

2.3 Numerical Differentiation

Numerical differentiation is used in several quantities throughout this report. It will be used to compute accelerations from given positions (i.e., , simulated GPS positions) and to compute angular velocities from a given set of attitude angles.

All the quantities mentioned are of a discrete nature; they are time-series of measurements and the exact computation of their derivatives is not possible. The sought derivatives are approximated using finite differences methods.

The numerical differentiation is done by first considering an arbitrary continuous function, $f(x)$. Writing the Taylor expansion series of $f(x \pm h)$ yields,

$$\begin{cases} f(x+h) = f(x) + hf'(x) + \dfrac{h^2}{2}f''(x) + O(h^3) \\ f(x-h) = f(x) - hf'(x) + \dfrac{h^2}{2}f''(x) + O(h^3) \end{cases} \tag{2.51}$$

Using the linear combination,

$$\begin{cases} f(x+h) + f(x-h) = 2f(x) + h^2 f''(x) + O(h^3) \\ f(x+h) - f(x-h) = 2hf'(x) + O(h^3) \end{cases} \tag{2.52}$$

now we solve the system of equations for f' and f'',

$$\begin{cases} f''(x) = \dfrac{f(x+h) - 2f(x) + f(x-h)}{h^2} + O(h^3) \\ f'(x) = \dfrac{f(x+h) - f(x-h)}{2h} + O(h^3) \end{cases} \tag{2.53}$$

Considering h as the sampling period of the data series to be differentiated, Eqn. 2.53 gives expressions for the 1^{st} and 2^{nd}-order derivatives exact up to the order of h^3. In the same way, but using more data points, more accurate expressions of the derivatives could be obtained.

2.4 Numerical Integration

Throughout this report numerical integration will be used to process the discrete measurements of the inertial sensors into the relevant quantities, namely the angular velocity measured by the gyros is integrated into the attitude of the platform. Although not implemented in this thesis similar procedure could be applied to integrate the specific force measurements into the position and velocity of the platform.

A very compact introduction to the numerical integration methods used in this work is provided in the following paragraphs. This is by no means a complete reference of numerical integration methods. The intent is simply to state the methods that were used. For a better insight on Runge-Kutta methods the reader is referred to Jekeli (2001, chap. 2) where the Runge-Kutta methods are thoroughly explained or to a more specific numerical methods reference (e.g., Chapra and Canale (2010)).

The class of problems which need to be numerically integrated in the context of airborne gravimetry can be represented as a system of linear first-order differential equations,

$$\dot{y} = f(t, y(t)) \tag{2.54}$$
$$y(t_n) = \mu \tag{2.55}$$

where f is a linear function of time, t, y is the variable to be integrated and μ are the initial conditions of y.

Applying a Taylor series expansion to $y(t_n)$ allows us to write,

$$y(t_{n+1}) = y(t_n) + h\dot{y}(t_n) + \frac{h^2}{2!}\ddot{y}(t_n) + \cdots + \frac{h^m}{m!}y^{(m)}(t_n) + \cdots \tag{2.56}$$

Where,

t_n – is the initial time of the integration step.
t_{n+1} – is the final time of the integration step.
h – is the integration step size, $h \equiv t_{n-1} - t_n$.

Noticing Eqn. 2.54, one can write the derivatives of y in terms of f,

$$\begin{aligned} \ddot{y}(t_n) &= f_t + f_y f \\ \dddot{y}(t_n) &= f_t t + f_{ty} f + f\left(f_{yt} + f_{yy} f\right) + f_y\left(f_t + f_y f\right) \\ &= f_{tt} + 2f_{ty} f + f_{yy} f^2 + f_t f_y + {f_y}^2 f \\ &\vdots \end{aligned} \tag{2.57}$$

where $f_j \equiv \frac{\mathrm{d}f}{\mathrm{d}j}$.

Equation Eqn. 2.56 shows us that the variable y can be evaluated at time t_{n+1} having only the initial conditions, $y(t_n)$, and all the derivatives of function f up to order m. In general these high-order derivatives are not accessible and this is where the Runge-Kutta integration methods steps in.

The idea behind the Runge-Kutta methods is to replace the knowledge of the high-order derivatives of y by the evaluating f at several points in the neighborhood of t_n. The general form of a Runge-Kutta method is the following,

$$y_{n+1} = y_n + h(\alpha_1 k_1 + \alpha_2 k_2 + ... + \alpha_m k_m) \tag{2.58}$$

with,

$$\begin{aligned} k_1 &= f(t_n, y_n) \\ k_2 &= f(t_n + \beta_2 h, y_n + \epsilon_{2,1} h k_1) \\ k_3 &= f(t_n + \beta_3 h, y_n + \epsilon_{3,1} h k_1 + \epsilon_{3,2} h k_2) \\ &\vdots \end{aligned} \tag{2.59}$$

Where,

- h – is the integration step size
- k_i – is a slope of y (the value of f) at some intermediate point $\tau \in [t_0\,;\,t]$
- α_i – are constants that weight each of the slopes k_i

The values of α_i, β_i and $\epsilon_{i,j}$ are chosen such that the difference between the integrated y_{n+1} and the real value $y(t_{n+1})$ is smaller than a certain power of h,

$$|y_{n+1} - y(t_{n+1})| \leq O(h^{m+1}) \tag{2.60}$$

The above condition describes an m-order Runge-Kutta algorithm. A 4^{th}-order Runge-Kutta algorithm has an error magnitude smaller than the fifth power of the integration step size, h^5.

The value of the parameters is determined by making the Taylor expansion of $f(t, y)$ around the point (t_n, y_n) in Eqn. 2.59. The expanded expressions for k_1, k_2 and k_3 are then substituted in Eqn. 2.58. Finally by comparing this with Eqn. 2.56, where the derivatives of y are replaced by the corresponding derivatives in f as in Eqn. 2.57, a set of constraints is obtained for the values of α_i, β_i and $\epsilon_{i,j}$. These conditions are not independent, and therefore some degree of freedom still exists in the choice of these parameters. In fact different choices of parameters create then different Runge-Kutta methods.

For the sake of brevity, we will simply state the different values of the parameters for the integration methods that will be used. The simplest integration method we will use is a 2^{nd}-order method known as *the midpoint rule*. The integration is done using only the derivative at the middle of the integration interval ($\alpha_1 = 0$ and $\alpha_2 = 1$),

$$\begin{aligned} y_{n+1} &= y_n + hk_2 \\ k_2 &= f(t_n + \frac{h}{2},\, y_n + \frac{h}{2} f(t_n,\, y_n)) \end{aligned} \tag{2.61}$$

Another method that will be used is a 3^{rd}-order method with the following structure,

$$\begin{aligned} y_{n+1} &= y_n + \frac{h}{6}\,(k_1 + 4k_2 + k_3) \\ k_1 &= f(t_n,\, y_n) \\ k_2 &= f(t_n + \frac{h}{2},\, y_n + \frac{h}{2} k_1) \\ k_3 &= f(t_n + h,\, y_n - hk_1 + 2hk_2) \end{aligned} \tag{2.62}$$

This method is also known as *Simpson's rule* when $f(t, y(t)) \equiv f(t)$.

2.5 Linear Perturbations

To analyze the performance of the strapdown system, it is important to estimate the errors in the inertial sensors from the output of the IMU. To do this a model

must exist that describes how the errors in the measurements propagate to the output to the system. In general the equations that rule the behavior of errors in the modeled system are obtained by applying the theory of *linear perturbation*.

Consider the following differentiable function f evaluated at a given set of parameters $(\alpha, \beta, \cdots, \omega)$.

One defines the perturbation of f around an arbitrary nominal point $(\alpha_0, \beta_0, \cdots, \omega_0)$ as,

$$\delta f = f(\alpha_0 + \delta\alpha, \beta + \delta\beta, \cdots, \omega + \delta\omega) - f(\alpha_0, \beta_0, \cdots, \omega_0) \tag{2.63}$$

The first term of Eqn. 2.63 is expanded in a Taylor series around the nominal point. Only the first order terms are kept, and the differentials are understood as small deviations from the nominal value, normally seen as *errors*,

$$\delta f = f(\alpha_0, \beta_0, \cdots, \omega_0) + \frac{\partial f}{\partial \alpha}\delta\alpha + \frac{\partial f}{\partial \beta}\delta\beta + \cdots + \frac{\partial f}{\partial \omega}\delta\omega - f(\alpha_0, \beta_0, \cdots, \omega_0) \tag{2.64}$$

and the derivatives are evaluated at the nominal point $\{\alpha_0, \beta_0, \cdots, \omega_0\}$.

The linear perturbation of function f can be simply written as,

$$\delta f = \frac{\partial f}{\partial \alpha}\delta\alpha + \frac{\partial f}{\partial \beta}\delta\beta + \cdots + \frac{\partial f}{\partial \omega}\delta\omega \tag{2.65}$$

With Eqn. 2.65 one can understand of how the errors of each parameter propagate into an error of the function (or model).

3 Calibration

In this chapter the calibration of the JAE Type-3 accelerometers and the Fizoptika VG951 gyroscopes is detailed. The purpose of the calibration is to understand how the instrument outputs can be related to the physical quantity they are measuring and to characterize the parameters involved in the transformation. Additionally during the calibration the noise level of the instruments can be visualized which will then be replicated in the simulations. In the final section of this chapter an error model for the inertial sensors is defined, later applied to the Kalman filter.

It should be noted that the calibration of the accelerometers was not thorough and many details remain to be clarified. The major reason for this is owed to the late availability of the instruments for calibration. The necessary electronics that convert the analog signal provided by the instrument into a digital form to be logged over time are still under development and only a prototype interface was available for the work done in this thesis. The gyro calibrations were more complete; however, there are still some aspects that require more testing and validation. Nonetheless most of the specifications of the instruments were cross-checked against the manufacturer's specifications and this knowledge could later be propagated into the simulation domain.

3.1 The Accelerometer Calibration

To simulate a working INS, knowledge about the accelerometers and how to correctly transform the measured voltages into the corresponding accelerations is essential to obtain any useful results. The accelerometers used in the present section are the JAE JA-5 Type III servo accelerometer, which are very similar to the Honeywell QA-3000. The accelerometer datasheet states the following,

- The instrument bias, b_a, is smaller than $4\,\mathrm{mG} \approx 4000$ mGal.
- The instrument nominal scale factor, κ_a, is stated to be between 1.197 and 1.463 $\mathrm{mA.G^{-1}}$, which can be translated into 0.4326 to $0.5287\,\mathrm{mGal.}\mu\mathrm{V^{-1}}$ where the readout resistor used was $1580\,\Omega$. G is defined as the normal gravity at 45° latitude, i.e., $\mathrm{G} \equiv 9.80665$ $\mathrm{m.s^{-2}}$.
- The root mean square of the instrument's noise is stated to be smaller than 5 mV for sampling frequencies below 500 Hz and with the maximum scale factor this value can be computed to about 2592 mGal.

The interface electronics used in the following experiments were created by René Reudink, a research technician within the Physical and Space Geodesy group at

TU-Delft. The accelerometer signal is digitized through an analog/digital (A/D) converter and then sent to a microprocessor responsible for displaying, storing and communicating with the computer through a HyperTerminal[1] interface. The system is completed with a power supply in the form of a simple battery. The sampling rate is 4 Hz and two kinds of measurements are taken: the voltage, V, at the terminals of the readout resistance and the working temperature, T.

The voltage V measured by the accelerometer is a function of the specific force, f, along the sensitive axis of the instrument and the temperature of the instrument, T. Additionally the accelerometer contains a constant bias term V_b and a noise parameter μ_V. Explicitly,

$$V = V_b + \kappa_a f + V(T) + \mu_V \tag{3.1}$$

Where,

- V_b – is a voltage bias of the accelerometer
- κ_a – is the scaling factor between the input specific force and the measured voltage.
- $V(T)$ – is a function relating the voltage output of the instrument to the working temperature.
- μ_V – is the accelerometer noise parameter.

Model Eqn. 3.1 reflects the relation $V = \mathrm{f}(f, T)$, however a more useful model is the one used to compute the specific force from the measured voltage, $f = \mathrm{f}(V, T)$. Therefore one can rewrite Eqn. 3.1 in the following way,

$$f = \frac{1}{\kappa_a}\left(V - V_b - V(T) - \mu_V\right)$$

and noticing the change in notation the sought model is found to be,

$$f = \kappa_v V - b - \mathrm{f}(T) - \mu_a \tag{3.2}$$

Where,

- $\kappa_v \equiv \kappa_a^{-1}$ – is scaling factor between the measured voltage and the input specific force.
- $b \equiv \frac{V_b}{\kappa_a}$ – is the accelerometer bias.
- $\mathrm{f}(T) \equiv \frac{V(T)}{\kappa_a}$ – is a function describing the temperature dependency of the sensor.
- $\mu_a \equiv \frac{\mu_V}{\kappa_a}$ – is the noise of the instrument.

The accelerometer is a very temperature sensitive instrument, and therefore the temperature model $\mathrm{f}(T)$ needs to be carefully studied to obtain useful results from the instrument; however, in the context of this thesis, a temperature controlled facility where relevant testing could be done was not available and therefore a

[1] a computer communication software normally bundled with Windows up to and including Windows XP.

temperature calibration of the instrument was not carried out. In the absence of knowledge about the temperature model, the following approach was taken in the calibration procedures. If the measured temperature, T, changes only by a small amount, then the first-order Taylor expansion around the mean temperature $\bar{T}$ is valid,

$$\mathrm{f}(T) \approx \mathrm{f}(\bar{T}) + \left.\frac{\mathrm{df}}{\mathrm{d}T}\right|_{T=\bar{T}} \delta T \tag{3.3}$$

and δT are the deviations of the recorded temperature from the nominal one. Replacing Eqn. 3.3 in model Eqn. 3.2, notice that $\mathrm{f}(\bar{T})$ is a constant value and can be included in the bias term.

$$\begin{aligned} f &= \kappa_v V - \underbrace{b - \mathrm{f}(\bar{T})}_{\text{const.}} - \left.\frac{\mathrm{df}}{\mathrm{d}T}\right|_{T=\bar{T}} \delta T - \mu_a \\ f &= \kappa_v V - b_{\bar{T}} - \kappa_{\bar{T}} \delta T - \mu_a \end{aligned} \tag{3.4}$$

In the first few experiments the accelerometer was left, vertically positioned, logging the voltage and working temperature. This kind of static experiment, without any acceleration reference for calibration, were mainly carried out with the purpose of verifying the working capability of the system. In the absence of any external observation of the acceleration any estimation procedure is compromised; however, one can try to estimate the noise level of the system by noticing that, in this static setup, the accelerometer is excited by the local gravity vector, g_l, which is unknown but *constant*. Replacing f in equation Eqn. 3.1 by g_l and linearizing the temperature model as in Eqn. 3.4, the following is obtained,

$$\begin{aligned} V &= \underbrace{V_b + \kappa_a\, g_l + V_{\bar{T}}}_{b \equiv \text{const.}} + \kappa_T\, \delta T + \mu_V \\ &= b + \kappa_T\, \delta T + \mu_V \end{aligned}$$

This model can be translated in a typical least-squares (LS) form,

$$\begin{cases} y &= A.x \\ y &\equiv V \\ A &\equiv \begin{bmatrix} 1 & \delta T \end{bmatrix} \\ x &\equiv \begin{bmatrix} b & \kappa_T \end{bmatrix}^T \end{cases} \tag{3.5}$$

The estimate is computed as,

$$\hat{x} = \left(A^T A\right)^{-1} A^T y \tag{3.6}$$

And the noise of the instrument can finally be estimated from the residuals of the fit as,

$$\sigma(\mu_V) = \sigma(y - A\hat{x}) \tag{3.7}$$

The initial testing of the accelerometer was conducted in the L&R faculty. The accelerometer was left, in the vertical position, recording 22 hours of data at the 2nd floor of the building. The gathered data is shown in Figure 3.1.

With the results of this static experiment, it was possible to approximate the scale factor of the instrument. The average of the recorded voltage was $\bar{V} = 2.072151$ V, and the local magnitude of the gravity vector is $G_L = 9.8124\,\mathrm{m.s^{-2}}$. With these values, the scale factor κ_a can be estimated as,

$$\kappa_a = \frac{G_L}{\bar{V}} = \frac{G_L}{G.\bar{V}}.G = 0.4828\ \mathrm{mGal}.\mu\mathrm{V}^{-1} \tag{3.8}$$

which is within the instrument specifications. The quietest period of the night (from 23h to 05h) was selected in Figure 3.1, and the instrument noise was estimated as in Eqn. 3.7. The standard deviation of the noise in the measurements was found to be $85.65\,\mu$V, and using the estimated scale factor, this value can be translated into 44.41 mGal.

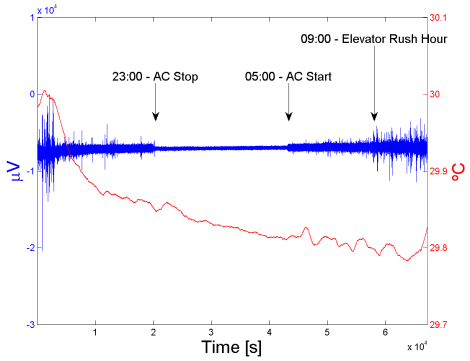

Figure 3.1: Data logged from the accelerometer at the L&R faculty.

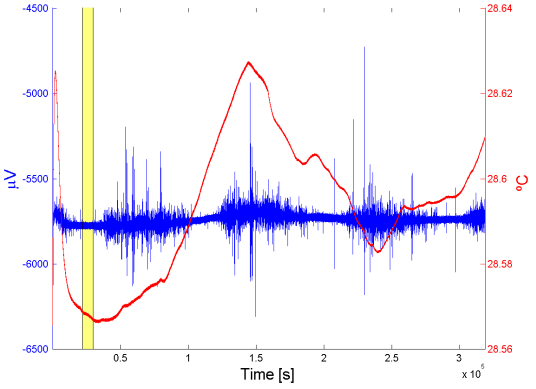

Figure 3.2: Accelerometer measurements spanning 3 days.

It was seen from the results that the building was constantly experiencing small vibrations, especially when the elevators were moving. Even during the night, when the elevators are stopped and the AC is turned off, the movement of the building is enough to mask the noise of the instrument. For this reason, the location of the following experiments was changed to a 6-floor building in the vicinity chosen for its structural rigidity and ease of access. In this location, two experiments were carried out.

The first experiment (in the new location) was another static test, conducted over 3 days in the basement of the aforementioned building, with the main purpose of evaluating the long-term stability of the logging system. Additionally, by recording data during the night, when the inhabitants are sleeping and the elevators are still, the variations in the recorded signal can be attributed to the system's noise. The basement is where the conditions are the quietest and the temperature

is relatively stable over long periods. In Figure 3.2 the gathered dataset is shown. Notice the scaling of the axes in comparison with the ones in Figure 3.1 taken at the L&R building, to see a significantly smaller magnitude of the measured accelerations and much more stable temperature.

The marked area in Figure 3.2 represents about 2h 15min and it was selected to estimate the level of noise of the instrument because of its relatively stable signal and small temperature variation. The standard LS approach is used once again to estimate the system noise level as in equation Eqn. 3.7. The standard deviation of the system noise in the basement was found to be 6.02 μV. Once again, using the estimated scale factor, this value can be translated to 3.12 mGal.

The second experiment was done to observe the sensitivity of the instrument and to have an idea of the magnitude of the temperature influence on the measurements. This was done by using a very precise, relative gravimeter, the Scintrex CG-5, and taking 30 min samples of data with both instruments on the 1st, 3rd and 6th floors (see Figure 3.3).

The gravity gradient along the radial direction of the Earth at surface height is approximately -0.33 mGal.m^{-1}. This means that in the distance between 2 floors (ca. 6-7m), one can expect a change in the gravity vector of about 2 mGal. From the measurements taken by the relative gravimeter the change in gravity was 2.3 mGal.

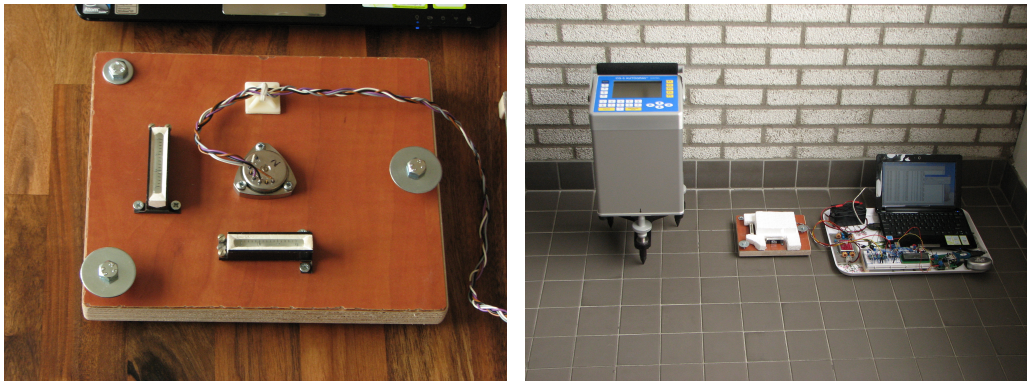

(a) The accelerometer platform

(b) Accelerometer and Gravimeter recording measurements.

Figure 3.3: On the left the accelerometer platform with two perpendicular water-levels and two adjustable screws for tilt correction. On the right a picture of both systems logging data side-by-side

The temperature differences between the floors were quite high and, given the high temperature sensitivity of the accelerometer, a large signal variation can be seen in the measurements between floors and even for the same floor while the accelerometer temperature stabilizes. The logged accelerations and temperatures from the three floors are shown in Figure 3.4a. The figure highlights the strong correlation between the measured temperature and acceleration.

With the relative gravimeter a very accurate reference of the local gravity acceleration is available to calibrate the accelerometer. Estimating the parameters of the model in Eqn. 3.2 in a LS sense yields the values in Table 3.1. The calibrated accelerometer is plotted against the gradiometer reference value in Figure 3.4b

Parameter		Value	
Scale Factor	κ_v	0.05628	mGal.μV^{-1}
Bias	b	-5559.67	mGal
Temperature Coefficient	κ_T	74.2751	mGal.°C^{-1}
STD Residuals	$\sigma(\mu_a)$	1.03902	mGal

Table 3.1: Estimated Accelerometer Parameters

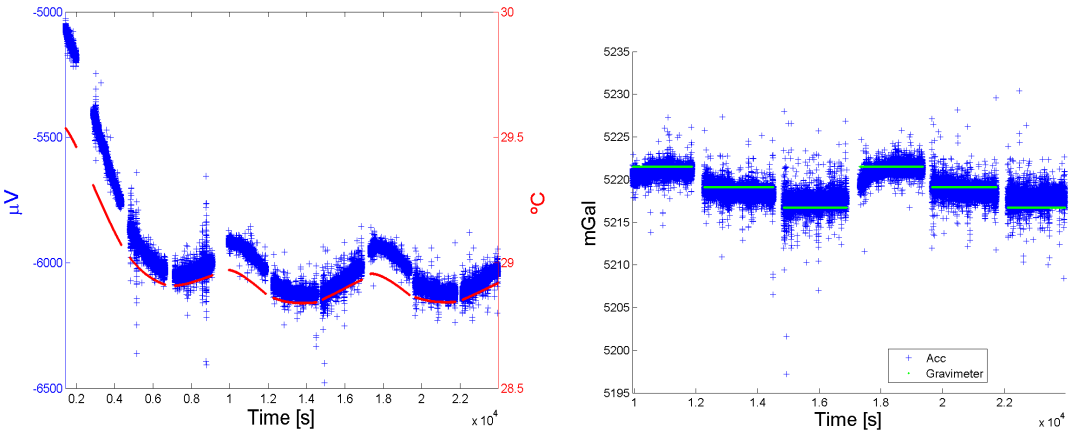

(a) Acceleration and temperature plots

(b) Accelerometer vs. Gravimeter

Figure 3.4: In Figure 3.4a the raw acceleration (blue) is clearly correlated with measured temperature (red). Figure 3.4b plots the calibrated accelerometer (blue), obtained after the LS fit, and the acceleration measured by the gravimeter (green).

The estimated bias is above the datasheet specification of ± 4000 mGal, but not significantly. Furthermore, due to the temperature model linearization, part of the estimated bias is actually temperature dependent and in that sense it not actually a proper bias. Since the temperature was not controlled during the experiment, it is not possible to know if the instrument bias is within specifications or not.

In an attempt to better model the temperature dependency, a second order polynom of the temperature was used in the fit, with no real improvement. It seems that the temperature inside the accelerometer casing experiences a time delay relative to the one measured by the temperature sensor embedded in the external part of the accelerometer casing. The actual temperature inside the casing seems to change slower than the one recorded by the thermometer. This is not clearly seen in any of the shown figures and therefore it is left as a matter of future investigation using more thorough calibrations of the accelerometer. The temperature modeling

was not further pursued in the context of this thesis, but it became apparent from these experiments that the temperature has a very big impact on the measured acceleration, and it requires careful modeling and/or control to reach the maximum performance of the sensor under a more dynamic environment. This is also clearly stated in Meyer et al. (2003, sec. 6.2.3) where the similar Honeywell QA3000 accelerometers were tested.

The estimated scale factor, $0.05\,\text{mGal}.\mu\text{V}^{-1}$, is one order of magnitude smalled than the datasheet specification, between 0.43 and $0.52\,\text{mGal}.\mu\text{V}^{-1}$. The explanation can be attributed once again to the temperature dependency of the sensor. Since each floor had a different temperature, a large correlation between the gravity and temperature signals exists which might have lumped most of the of scale factor together with the temperature coefficient. This would explain the large discrepancy between the obtained value and the previously estimated one. Further testing will clarify this issue. The experiment can be improved by exploring a larger working range of the accelerometer (instead of the small $\approx$5 mGal variation used in this experiment) while keeping the temperature of the instrument as steady as possible.

The standard deviation of the residuals leads to the conclusion that the noise level of the instrument is 1 mGal *at 4 Hz sampling rate*. This value is 2 to 3 orders of magnitude smaller than the specified 2592 mGal value *at 500 Hz sampling rate*. Since the sampling rates are quite different it is not possible to conclude whether the instrument is operating within specs.

From this experiment it becomes clear that variations in the temperature seriously degrade the quality of the accelerometer measurements and therefore accurate knowledge about the temperature model is required for further calibration activities. From the first static experiment it was possible to observe that the accelerometer scale factor (the only observable parameter in this kind of test) is within the range specified in the datasheet. With additional experiments, the bias and noise level of the instrument still could not be correctly compared with the datasheet specifications; it is assumed for the remaining of this thesis that the JAE JA-5 Type III accelerometers are working within specifications.

The Honeywell QA3000 accelerometers have also been purchased by the GAIN project and while being very similar to the previous ones, they claim better performance. The stated bias and scale factors are the same as the ones stated for the JAE JA-5, but the noise level is claimed to be <70 mGal, two orders of magnitude smaller. These accelerometers were not calibrated in the course of this thesis because they were unavailable during this period. Assuming again that the Honeywell accelerometers will also perform within specifications, they are more accurate than the JAE's and therefore these are the accelerometers that will be considered for the simulations of the GAIN strapdown airborne gravimetry system.

3.2 The Gyro Calibration

The Fizoptika VG951 fiber-optic gyroscopes (FOG) have been calibrated using the Acutronic AC2237 rate table at the L&R faculty. Similarly to the accelerometer calibration, the parameters of interest in the FOG are the bias, scale factor and noise level.

The basic idea behind any calibration is to find the relation between the instrument's output and the physical quantity that it measures. Since, in general, the physical quantity is not available directly (that's why the sensor is needed in the first place) the sensor is calibrated against a more precise reference. In this case, the rate table is the reference and the gyro is placed on top of it. By simultaneously logging the table and the gyro it becomes possible to find this relation.

Figure 3.5: Picture of the gyro calibration on the rate table

Several problems were identified during the course of this study regarding the data logging process, and have been corrected to the best possible extent. First, and for comparison purposes, a fit without considering any of the problems is shown. The phenomenon that adversely affect the fit will be identified and a final fit will be shown where the observed problems have been dealt to the furthest extent.

The fit between the gyro and the table is done using the following 3$^{\text{rd}}$-order model (Fizoptika, 2010),

$$\Omega = \Omega_0 + SF_1 V + SF_3 \frac{V^3}{V_M^2} + \mu_g \tag{3.9}$$

where,

V – raw gyro output [V]
V_M – gyro output voltage at maximum working range [V]
Ω – rate table angular velocity [deg.s^{-1}]
Ω_0 – gyro bias [deg.s^{-1}]
SF_i – the i$^{\text{th}}$-order scale factor [deg.s^{-1}.V^{-1}]
Ω_0 – gyro bias [deg.s^{-1}]
μ_g – gyro noise [deg.s^{-1}]

The VG951 datasheet (Fizoptika, 2010) states the following specifications,

- The instrument bias Ω_0 is smaller than $8.33(3) \times 10^{-3}$ deg.s^{-1}
- The instrument scale factor SF_1 is within $41.6(6) \pm 15\%$ deg.s^{-1}.V^{-1}
- The nonlinearity at half of the gyro range is smaller than $nl|_{V=\frac{V_M}{2}} < 3\%$
- The nonlinearity at maximum working range is smaller than $nl|_{V=V_M} < 15\%$
- The noise PSD is constant in the instruments working frequency and is about $10\mu\text{V}.\sqrt{Hz}^{-1}$. This means that the RMS of the noise $\mathbf{e}$ can be computed has follows,

$$\begin{aligned}\sigma_{\mathbf{e}} &= \text{PSD} \times \sqrt{f_s} \\ &= 10 \times 10^{-06} \times \sqrt{300} \\ &= 1.73205 \times 10^{-04}\,\text{V}\end{aligned}$$

multiplying by the nominal scalefactor,

$$\begin{aligned}&= 1.73205 \times 10^{-04} \times 41.6667 \\ &= 7.21572 \times 10^{-03}\,\text{deg.s}^{-1}\end{aligned}$$

The nonlinearity term can be written as the quotient between the nonlinear part and the linear part of the model disregarding the bias,

$$\Omega - \Omega_0 = \underbrace{SF_1 V}_{\text{linear}} + \underbrace{SF_3 \frac{V^3}{V_M^2}}_{nonlinear} \tag{3.10}$$

so the nonlinearity can be easily computed as,

$$nl = \frac{SF_3 \frac{V^3}{V_M^2}}{SF_1} \tag{3.11}$$

The gyro noise RMS value can be estimated from the formal error of the LS fit. More precisely,

$$\sigma_{\mathbf{e}} = \mathbf{e}^T.\mathbf{e} = (\mathbf{y} - A\mathbf{x})^T.(\mathbf{y} - A\mathbf{x}) \tag{3.12}$$

with,

$$\mathbf{y} = \begin{bmatrix} \Omega_1 & \Omega_2 & \cdots & \Omega_N \end{bmatrix}^T$$

$$A = \begin{bmatrix} 1 & V_1 & \frac{V_1^3}{V_M^2} \\ 1 & V_2 & \frac{V_2^3}{V_M^2} \\ & \vdots & \\ 1 & V_N & \frac{V_N^3}{V_M^2} \end{bmatrix}$$

$$x = \begin{bmatrix} \Omega_0 & SF_1 & SF_3 \end{bmatrix}^T$$

and the computed value of $\sigma_{\mathbf{e}}$ accounts for the gyro noise and mismodeling errors. When using an appropriate model, the computed value should approximate the noise level of the instrument. When the computed value is excessive compared with the specification, this often means that the model used is inadequate to describe the data and as such the resulting fit has poor quality.

In November 2007, a flight test was performed by the GAIN project using a commercial INS system alongside the IMU currently in development. Unfortunately, the gathered accelerometer data did not meet the required accuracy but much has been learned from this experience. In this test flight, the angular velocities measured by the gyro triad were never bigger that $10\,^\circ.\text{s}^{-1}$. For that reason, the range of interest for the calibration is shortened to $\pm 15\,^\circ.\text{s}^{-1}$ range to obtain a better fit to the instruments' parameters (the full range of the instrument is $\pm 80\,^\circ.\text{s}^{-1}$). The mechanical input to the instrument was selected to be a sinusoidal wave with an amplitude of $15\,^\circ.\text{s}^{-1}$ and a frequency of 0.74 Hz.

In Table 3.2 the results of the fit are shown and crosschecked with the figures from the datasheet. Notice the high RMS value of the residuals and then notice Figure 3.6 where the residuals are plotted. The residuals exhibit a deterministic behavior and this means that the obtained fit has poor quality and the model used does not correctly describe the relation between the gyro and the rate table measurements. It is imperative to understand what is happening to obtain a better description of the instrument.

Table 3.2: Results of the LS fit to the model in Eqn. 3.9 compared with the gyro specifications.

Parameter		Fit	Datasheet	
Ω_0	deg.s^{-1}	4.40252×10^{-03}	$< 8.33(3)\times10^{-3}$	✓
SF_1	$\text{deg.s}^{-1}/\text{V}$	37.2285	$\in 41.66(6)\pm15\%$	✓
$nl\|_{V=\frac{V_M}{2}}$		1.37%	$< 3\%$	✓
$nl\|_{V=V_M}$		10.9%	$< 15\%$	✓
RMS($\mathbf{e}$)	deg.s^{-1}	3.77860×10^{-01}	$< 7.21572\times10^{-03}$	✗

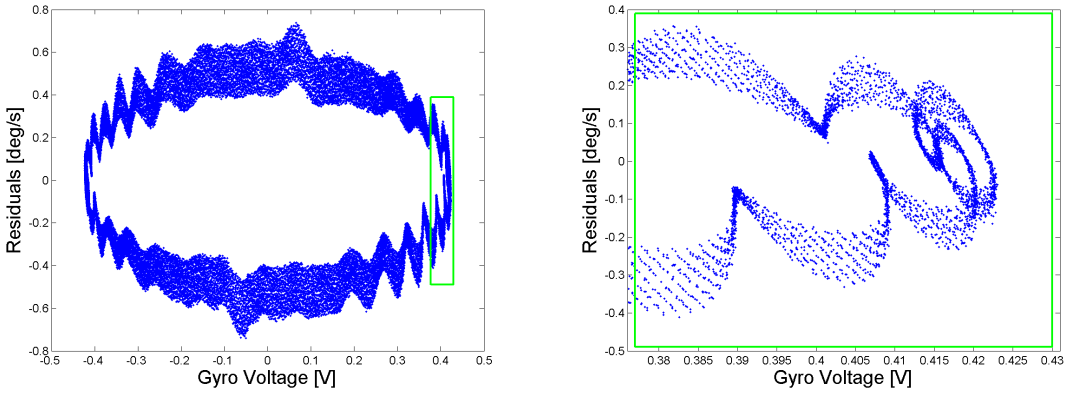

(a) Residuals vs. Gyro Voltage

(b) Zoom-in

Figure 3.6: Residuals of the LS fit between the VG951 FOG and rate table measurements. Note that the residuals are *not* plotted vs. time but vs. the measured voltage.

There are some features in the residuals that need to be acknowledged. First notice in Figure 3.6a the circular trajectory that the residuals describe with each cycle of the sinusoidal input. After some investigation it was possible to conclude that this is caused by a time delay between the measurements made by the gyro (or the rate table) and their time of registration. Notice also in Figure 3.6b the stripe pattern in the residuals which was found to be caused by an oversampling of the gyro measurements. Both of these problems severely degrade the performance of the parameter estimation and need to be appropriately dealt with.

3.2.1 Data Downsampling

The datalogging setup is quite complex and several considerations have to be made before applying the LS fit. The first critical problem lies in the different sampling rates of the gyro and logging system. The rate table is responsible for logging its own angular velocity along with several other important variables. The gyro sampling rate is 300 Hz and it is connected to a dSPACE system which is responsible for logging the gyro messages. To implement the synchronization of both datalogging systems the rate table clock is fed to the dSPACE system in a way that the logging of the gyro and table is coordinated by the table clock. The problem is that, the rate table has an internal 2000 Hz clock that can only be divided by integers resulting in the nearest possible 333.33 Hz. This means that, during the datalogging, the gyro is being oversampled, creating several repeated messages throughout the dataset. This creates two immediate problems: repeated gyro messages are being used throughout the LS fit and the delay between the time of measurement and the corresponding registration time varies with each gyro sample. The stripe pattern of the residuals in Figure 3.6b is caused precisely by this oversampling. The oversampling phenomenon is illustrated in Figure 3.7,

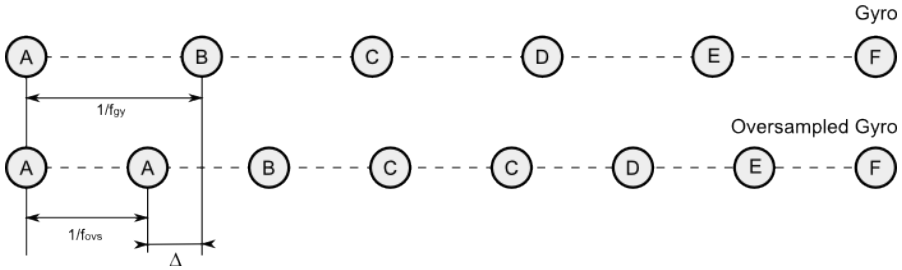

Figure 3.7: The oversampled gyro as logged by the DSPACE system. f_{gy} and f_{ovs} stand for the gyro and oversampling frequencies respectively.

It is necessary to have both datasets at the same sampling frequency and aligned in time if any useful results are to be obtained from the calibration. To have both datasets aligned in time we need to correct the oversampling of the gyro data and downsample the table data to 300 Hz. This is done using the following algorithm,

1. Find the gyro repeated messages. The best way to do this is to use the COUNTER status of the gyro message. It counts from 1 to 16 and, if it is repeated, then it implies the message is repeated.

2. Delete the repeated gyro samples.

3. Create a new time vector starting at the first repeated message, with f_{gy}^{-1} s increments for the whole range of the data, and interpolate the table data into the new time vector, downsampling it to the gyro frequency. The interpolation method used is a standard cubic interpolation provided by MATLAB.

This procedure is exemplified in Figure 3.8 where the recovered gyro signal has a constant unknown time delay $\delta \leq \Delta$. The time alignment of both data streams is considered in the following section.

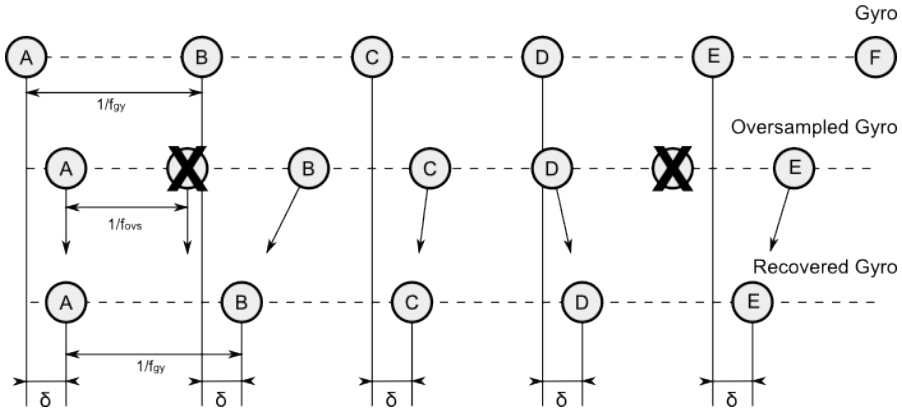

Figure 3.8: Correcting the oversampled gyro measurements. Notice that the processed gyro measurements will have a constant time offset relative to the original data.

3.2.2 Time Alignment

Correcting the unknown delay between both data streams is critical to the calibration procedure. The table is rotating with a certain angular velocity, $\omega(t)$. This function is observed by both gyro and rate table at slightly different times. Then, using a Taylor expansion of $\omega(t)$, one can write

$$\omega(t+\delta t) = \omega(t) + \dot{\omega}(t)\delta t + \frac{1}{2}\ddot{\omega}(t)\delta t^2 + \dots$$

Assuming that δt is small, terms beyond first order can be neglected and rearranging the equation gives

$$\omega(t+\delta t) - \omega(t) = \dot{\omega}(t)\delta t \tag{3.13}$$

If the table and gyro measurements have a certain time delay between them, their difference should be proportional to the table acceleration. For a sinusoidal input, the maximum angular acceleration happens at zero angular velocity while the zero angular acceleration happens for the maximum and minimum angular velocities. The circular shape described by the residuals in Figure 3.6a shows exactly this behavior which indicates the presence of a time delay between the gyro and table measurements.

We now intend to estimate this time delay and compensate the gyro measurements for it. It would be possible to include the time delay parameter in the model Eqn. 3.9; however, to maintain a separation between preprocessing of the data and parameter estimation, another (equivalent) approach was taken. Assume that the gyro measurements are delayed relatively to the table measurements, such that, $\Omega_{tbl} \equiv \omega(t)$ and $\Omega_{gy} \equiv \omega(t+\delta t)$. Then, according to Eqn. 3.13 the residuals of the fit, e, can be written,

$$e \equiv \Omega_{gy} - \Omega_{tbl} = \dot{\Omega}_{tbl}\delta t + \mu$$

and the time delay can be estimated also in a LS from the residuals of the fit as:

$$\hat{\delta t} = (\dot{\Omega}_{tbl}^T \dot{\Omega}_{tbl})^{-1} \dot{\Omega}_{tbl}^T \mathbf{e} \tag{3.14}$$

To correct for the time delay between the gyro and table measurements the following iterative scheme is applied,

1. Make a LS fit between the gyro and the table using model in (3.9).
2. Estimate the time delay between both streams from the residuals of the fit using (3.14).
3. If the estimated delay is smaller than 1% of the sample time, stop. Otherwise continue to 4.

4. With the estimated time delay, correct the gyro measurements by interpolating them to the correct time instant.

5. Go back to 1.

Ths algorithm normally stops after 2 or 3 iterations.

After using the above algorithm in the dataset, it became apparent that a varying time delay remained. This is well observed by inspecting the residuals versus the table acceleration depicted in Figure 3.9. The color of each point translates the time at which the sample was measured, allowing the distinction between different parts of the dataset. Notice that at the beginning of the dataset (in blue) the slope of the points is negative while at the end of the dataset (in red) the slope is opposite.

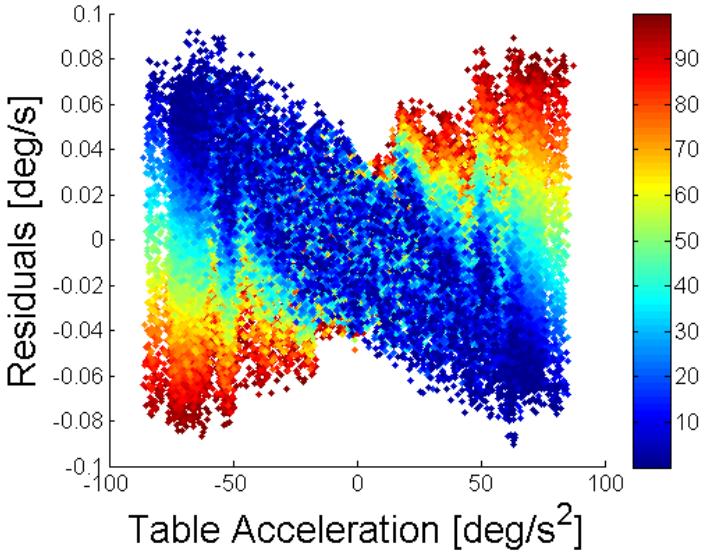

Figure 3.9: Residuals vs. Table Acceleration. The color indicates the time at which the sample was recorded. The changing slope shows that a variable delay exists in the dataset.

To correct for this varying time delay, the dataset is segmented in smaller parts; for each part a time delay is estimated in the same way as before (eq. Eqn. 3.14). After having a set of time delays for each different part of the dataset a continuous delay function is linearly interpolated from this discrete set to correct as accurately as possible the delay of each sample.

3.2.3 LS Fit with the processed data

At this point the datasets are aligned in time, sampled with the same frequency and a final LS fit can be made. The results can be seen in Table 3.3 and the residuals are plotted in Figure 3.10.

Table 3.3: New estimated parameters after processing and comparison with the gyro specifications

Parameter		Fit	Datasheet	
Ω_0	deg.s^{-1}	4.27807×10^{-03}	$< 8.33(3)\times10^{-3}$	✓
SF_1	deg.s^{-1}/V	37.2535	$\in 41.66(6)\pm15\%$	✓
$nl\|_{V=\frac{V_M}{2}}$		1.34%	$< 3\%$	✓
$nl\|_{V=V_M}$		10.7%	$< 15\%$	✓
RMS(**e**)	deg.s^{-1}	1.76490×10^{-02}	$< 7.21572\times10^{-03}$	✗

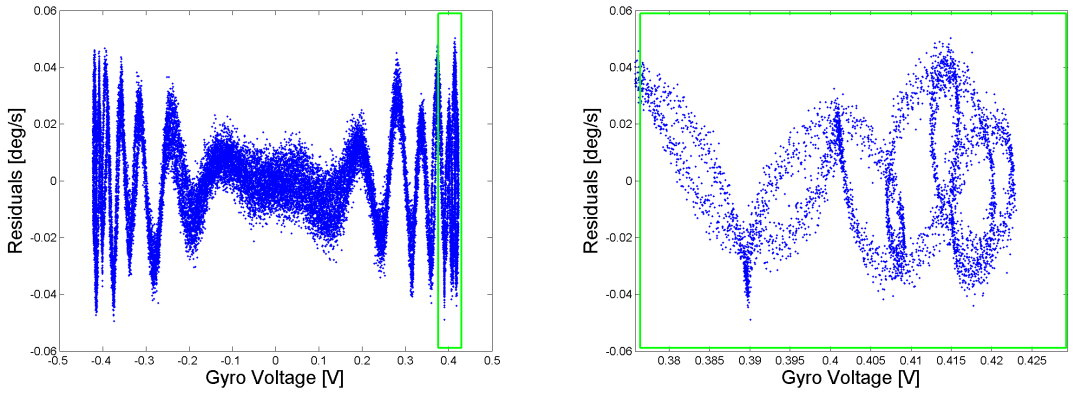

(a) Residuals vs. Gyro Voltage

(b) Zoom-in

Figure 3.10: Residuals of the LS fit after processing the gyro and table measurements. Note that the residuals are *not* plotted vs. time but vs. the measured voltage

The obtained fit is better and has succeeded in eliminating the circular shape and stripe patterns present in the previous residuals; however, an unknown oscillating signal still permeates the residuals. The cause of this signal is unknown and it is important to point out that this signal is already observed in the first fit made. This means that it was not introduced by any of the preprocessing routines applied. The argument is made here that this signal is not introduced by the gyro but instead by some systematic error in the data logging or by the rate table controller. To illustrate this argument, consider the following situation. The table records several variables in its dataset. In the first attempts of calibration the variable RATE_EST was used as the instantaneous rate of the table. However, it was later found out that this signal is actually filtered by the table controller and thus, it is not, in a proper sense, an observation of the table angular velocity. Using this variable was affecting the LS fit. To avoid this, the instantaneous rate, $\dot{\Omega}_{tbl}$, was instead computed by numerically differentiating the logged position of the table in time. This is an example of how unexpectedly the table recorded variables introduced error in the LS residuals. Accepting that this unknown signal is not a

part of the gyro's output, it is possible to observe two distinct ribbons of data in the residuals with a hysteresis-like behavior. These ribbons are the gyro's signal and from their thickness it is possible to conclude that their standard deviation is well within the value specified for the instrument.

On a final note about this chapter, notice that no temperature dependency was included in the gyro model. There is however, an influence of the temperature on the sensor and it is important to properly calibrate it. However a technical solution that allows the control of the gyro's temperature while rotating on the calibration table is being developed by the C&S group and therefore was not yet available for the work performed in this thesis. Omitting the temperature dependency from the gyro model in the presented results is, nonetheless, argued as valid since the gyro is much less temperature sensitive than the accelerometer and during the calibrations the temperature within the lab was kept stable to within 1°C.

3.3 Sensor Error Models

In a pre-flight calibration, the parameters of the gyro model Eqn. 3.9 are determined to the best possible extent. These parameters will be used during the flight to transform the voltage measurements provided by the gyro into the corresponding angular velocity as accurately as possible. However the instrument parameters are slightly volatile, i.e., they change with time, working conditions, temperature, with each instrument reset, etc. Having calibrated the model parameters pre-flight, the real parameters during the mission are, generally speaking, slightly different. Exactly the same is true for the accelerometers and therefore it is necessary to know how much do the inertial sensor parameters change with time. This is depicted in Table 3.4 where the repeatability of the gyro and accelerometer parameters is shown.

Table 3.4: The repeatability of the inertial sensor parameters as stated in the respective datasheets.

Acc	Bias repeatability	$\sigma(b_a) < 40$ mGal
	Scale Factor repeatability	$\sigma(\kappa_a) < 100$ ppm
Gyro	Bias repeatability	$\sigma(b_g) < 8.33(3)\ \times 10^{-4}$ deg.s^{-1}
	Scale Factor repeatability	$\sigma(\kappa_g) < 80$ ppm

The measurement done by an accelerometer, f, is computed from the measured voltage V and temperature T according to the model Eqn. 3.2 using previously calibrated values for each of the coefficients,

$$f = b + \kappa_v V + \kappa_T T + \mu_a \tag{3.15}$$

If the bias and scale factor parameters slightly deviate from their calibrated state,

then the computed acceleration $\tilde{f}$ will also deviate from the real value such that,

$$\begin{aligned}
\tilde{f} &= (\kappa_v - \delta\kappa_v)V - (b - \delta b) - \kappa_T T + \mu_a \\
\tilde{f} &= \underbrace{\kappa_v V - b - \kappa_T T}_{=f} + \delta b + \delta\kappa_v V + \mu_a \\
\tilde{f} - f &= \delta b + \delta\kappa_v V + \mu_a \\
\delta f &= \delta b + \frac{\delta\kappa_v}{\kappa_v} \underbrace{\kappa_v V}_{\approx\tilde{f}} + \mu_a \\
\delta f &= \delta b + \delta\kappa\tilde{f} + \mu_a
\end{aligned} \tag{3.16}$$

This is then the error model used to relate the computed acceleration $\tilde{f}$ and the real acceleration f. The same model can be used for the gyros, and Eqn. 3.16 can be expanded to a vectorial form for the accelerometer and gyro triads. Letting the term diag( ) represent a function that transforms a 3D vector into a diagonal matrix, we have,

$$\begin{aligned}
\delta\mathbf{f}^b &= \delta\mathbf{b}_a + \mathrm{diag}(\tilde{\mathbf{f}}^b)\delta\boldsymbol{\kappa}_a + \boldsymbol{\mu}_a \\
\delta\boldsymbol{\omega}_{ib}^b &= \delta\mathbf{b}_g + \mathrm{diag}(\tilde{\boldsymbol{\omega}}^b)\delta\boldsymbol{\kappa}_g + \boldsymbol{\mu}_g
\end{aligned} \tag{3.17}$$

Where,

- $\delta\mathbf{b}_a$ – is vector with the bias for each accelerometer.
- $\delta\boldsymbol{\kappa}_a$ – is the vector with the scale factor errors for each accelerometer.
- $\boldsymbol{\mu}_a$ – is the white noise vector of the accelerometer triad.
- $\delta\mathbf{b}_g$ – is vector with the bias for each gyro.
- $\delta\boldsymbol{\kappa}_a$ – is the vector with the scale factor errors for each gyro.
- $\boldsymbol{\mu}_g$ – is the white noise vector of the gyro triad.

This error model for the inertial sensors will be later applied within the Kalman filter responsible for the estimation of the IMU errors.

4 The Simulation Software

A collection of MATLAB routines was developed to simulate the GAIN strapdown airborne gravimetry system. The software was designed with multiple goals in mind; the first and most important is that it allows the data gathered in an airborne gravimetry system to be processed into the gravity disturbance vector at flight level. Beyond this, the software was developed with the intention of studying the airborne gravimetry system through simulation; it allows us to understand the effect that each instrument has on the accuracy of the output and which of them are critical to the performance of the system.

A short overview of the developed software is given below and all the mentioned steps are clearly detailed in the following sections of this chapter.

The software is divided in two major parts as depicted in Figure 4.1. The first part deals with the generation of data that GPS and IMU systems would record when flown along a given trajectory and attitude. The second part deals with the actual processing of the GPS and IMU measurements into a gravity disturbance vector at flight level.

The dataset generation part was implemented with flexibility in mind. The inputs are a sufficiently smooth[1] timeseries of coordinates and attitudes of the platform. The routine then generates the measurements that would be recorded

[1] discontinuities in the accelerations will results in problems during the processing

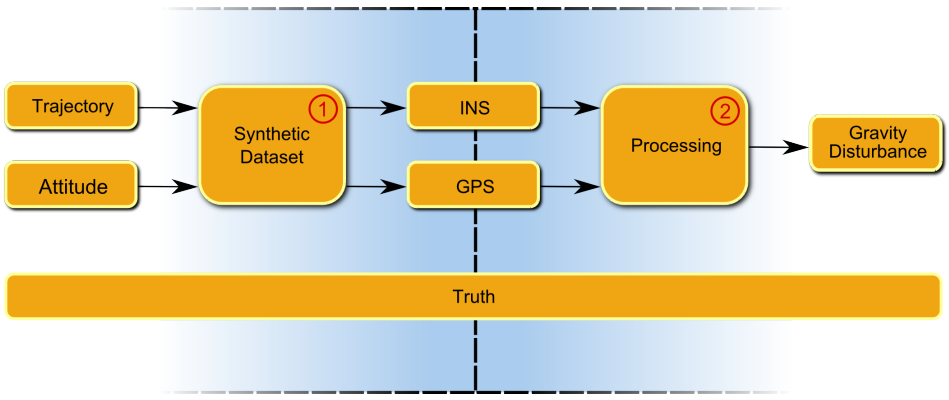

Figure 4.1: Division of the software in two parts: synthetic dataset generation (1) and dataset processing (2). The synthetic dataset generation receives a list of positions and attitudes to yield the corresponding GPS and IMU measurements. The processing part accepts a dataset of GPS and IMU measurements to yield the gravity disturbance vector at flight level.

by the accelerometers, gyros and GPS system while the platform moves through the given trajectory. Additionally it was made possible to configure the gyros, accelerometers and GPS sampling frequencies, their model parameters, noise and the gravity disturbance model.

At the end of the processing a dataset is created with the simulated GPS and IMU measurements along the desired path. At the same time a *truth dataset* is created with all the error-free information relevant to the simulation. This truth dataset establishes the reference to which every processed variable can be easily compared allowing us to debug the software during development phase and to evaluate the performance of the system at the end of each simulation.

The data processing part is divided into several distinct tasks. First the GPS positions are transformed from the e-frame into the i-frame where the processing of the data will take place. The kinematic acceleration, $\ddot{\mathbf{x}}^i$, is computed from the transformed positions.

As mentioned in Chapter 1, the accelerometry approach will be implemented, where the gravity disturbance vector is obtained from the difference between the total acceleration, as measured by the IMU and the kinematic acceleration, as measured by the GPS system. However, GPS is primarily used to obtain the position of the platform and to use GPS as an acceleration sensor one must double differentiate the measured positions. Before computing the gravity disturbance vector it is necessary to deal with the errors in the INS and GPS accelerations. The GPS errors exist mainly in the high frequencies due to the double differentiation of the position measurements and these errors are removed with a low-pass filter. The INS contains significant noise in the low-frequency, due to the biases and scale factors, and in the high-frequency parts of the spectrum due to the intrinsic noise of the accelerometers. To remove the high-frequency noise, low-pass filtering is applied, equivalent to the one used on the GPS-accelerations and the low-frequency errors are corrected with the parameters estimated by the Kalman filter.

The first step is then to low-pass filter the IMU specific force and GPS acceleration measurements. After this, a loop through all the data begins where one or more of the following tasks are performed:

- the most recent angular velocity measurements are integrated and the attitude matrix of the platform is updated. With the newly computed attitude the specific measurements, f^b, are rotated into the inertial frame, f^i.

- to keep track of the evolution of the errors in the system the Kalman filter continuously propagates the error state vector in time.

- at a GPS epoch, an observation of the acceleration and attitude[2] of the platform becomes available. By comparing the GPS and IMU accelerations and attitudes, an observation of the errors in the system is made and this new information is used by the Kalman filter to update the current estimate.

[2]attitude observations are actually optional.

As soon as the Kalman filter is updated with an observation, the estimated attitude error is used to correct the attitude integrator, and the roll, pitch, yaw errors in the state vector are reset to zero. This estimation procedure is called *closed-loop estimation*, (Jekeli, 2001; Tapley, 2004) and it becomes necessary in nonlinear systems such as this one. The reason is that the IMU gyros contain bias terms which, when integrated, continuously divert the computed attitude from the real one where the linearized model is not valid. Continuously correcting the integrated attitude bounds the attitude errors within the region of validity of the model.

When all of the data has been processed within the Kalman filter, the specific force measurements are corrected with the estimated bias and scale factors and the gravity disturbance vector is computed and compared to the true one to assess the performance of the system.

4.1 Gravity Model

The gravity model used within the software is divided in two parts. One is the *normal gravity* model, which approximates the real gravity field. This *normal gravity* can be a simple point-mass model as used in this thesis or any other more sophisticated models that exist to describe the gravity field of the Earth. The choice of normal gravity model is not important within the simulator since this is not the one that will be measured by the system. The system is only sensitive to gravity disturbances which are the deviations of the real field from the normal model and these are introduced in the *gravity disturbance model*. Both of them are described in detail in the following sections.

4.1.1 Normal Gravity Model

At several points in the generation of datasets and of the processing a normal gravity model is necessary. At all of these points the gravity model used is the one detailed in this section.

The normal gravity vector model $\boldsymbol{\gamma}^i(\mathbf{r}^i)$ used in the software is also presented in Jekeli (2001). A very simple point-mass model will be used where the whole mass of the Earth is compacted to single point located at the origin of the inertial frame. With this assumption the Earth's gravity model is fully described by Newton's Law of Gravitation,

$$\boldsymbol{\gamma}^i = -GM_E \frac{\mathbf{r}^i}{\|\mathbf{r}^i\|^3} \tag{4.1}$$

The GM_E parameter is called geocentric gravitational constant and is defined as the product of the universal gravitational constant, G, and the mass of the

Earth, M_E. The value used for this parameter is presented in Moritz (1992) and is one of the defining constants of the GRS80 ellipsoid.

$$GM_E = 3.986005 \times 10^{14}\,\mathrm{m}^3/\mathrm{s}^2 \tag{4.2}$$

Notice that the input to the model is the position in the i-frame, $\mathbf{r}^i$. Since most of the variables used in the software are defined in the i-frame, there was no need to implement alternative inputs to the function (e.g., the e-frame position).

4.1.2 Gravity Disturbance Model

The most important gravity model, however, is the model for the gravity disturbance that we wish to estimate within the (simulated) airborne gravimetry system.

The gravity disturbance, $\Delta\mathbf{g}$, is defined as the difference between the real gravity vector, $\mathbf{g}$, and a model, $\boldsymbol{\gamma}$, at the same position in space. This model can be as simple as the one discussed in the previous section, or any other more complex one. Independently of the chosen model, the gravity disturbance represents the deviation of the real gravity field from the one we know (or assume) to be true,

$$\Delta\mathbf{g} \equiv \mathbf{g} - \boldsymbol{\gamma} \tag{4.3}$$

The considered gravity disturbance model has previously been used in Alberts (2009, chap. 5, data set 2). The gravity disturbance is computed in a 6.5×6.5 degrees (630x730 km) area over Texas/Oklahoma in the USA, with a coordinate center at 33.25° N 100.00° W. The gravity disturbance values were computed from several global geopotential models, EGM96[3], GPM98b[4] and EIGEN-CG03c[5] in the following way:

- From degrees 121 to 360 data is computed from EGM96.
- From degrees 361 to the maximum degree 1800, data is computed from GPM98b.
- To simulate realistic gravity disturbances, the more recently published model EIGEN-CG03c was subtracted from degrees 121 to 360.

The values of the gravity disturbances were computed on a grid consisting of 66 East-West profiles at an altitude of 2 km. The distance between each profile is 0.1° ($\approx 10\,km$) and the spacing of points along the grid is 1 arc-min. A surface plot of the whole dataset can be seen in Figure 4.2. All the performed simulations obtain their gravity disturbance vector from this dataset and the continuous gravity disturbance function is emulated by using cubic interpolation between the nodes of the provided grid.

[3] Lemoine et al. (1998)
[4] Wenzel (1998)
[5] Förste et al. (2008)

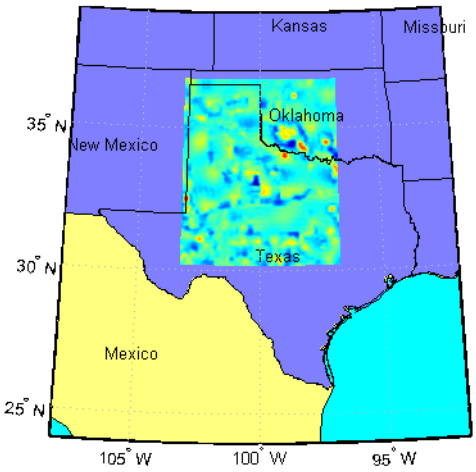

Figure 4.2: Surface plot of the gravity disturbance model over a map of the region.

The provided grid contained only scalar values instead of a real 3d gravity vector. To accommodate this into a gravity disturbance vector as computed by the airborne gravimetry system, the scalar values are assumed represent the vertical component along the n-frame and the horizontal components are assumed to be null.

4.2 Synthetic Dataset

In this section, the tasks involved with the synthetic dataset generation (i.e., step 1 in Figure 4.1) will be explored in detail.

The synthetic dataset is created with a routine that generates the measurements taken by the GPS and INS systems in a simulated flight. The routine was designed to be independent of any particular flight path; therefore, to actually use the routine one must first generate a time series of positions and angles describing the trajectory and attitude of the aircraft. First, an example will be shown of how the positions and attitude were generated for a specific flight path and some techniques that have been applied to ensure good results. After this, it will be shown how the IMU and GPS measurements are generated for any specified given flight path.

4.2.1 Creating a flight path

In this section the creation of the flight path shown in Figure 4.3, later used for the simulations, will be illustrated. To fully describe the kinematics of the platform the attitude of the platform at every time epoch also needs to be defined. For convenience, the set of positions is described with geodetic coordinates and the attitude angles describe the transformations between the body axes and the local naviga-

tion frame (i.e., the n-frame). The shown trajectory was built by concatenating

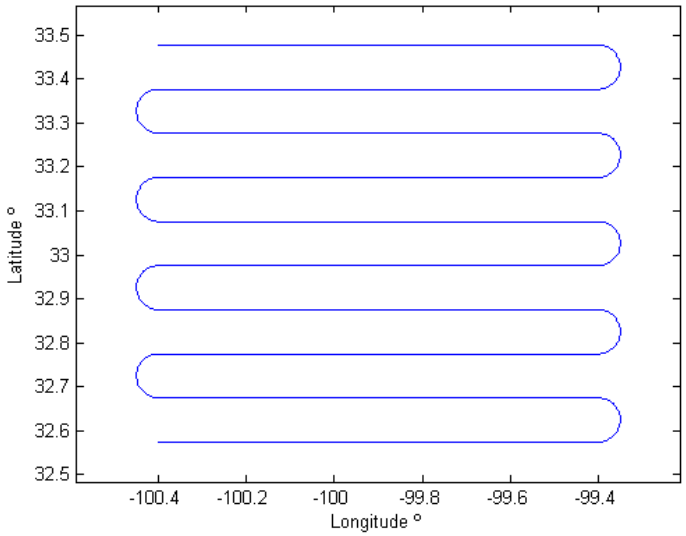

Figure 4.3: The trajectory built for the simulations

straight flight paths with half-circles defined in the geodetic coordinate space. The straight paths have constant latitude and the samples are equally distributed in space according to the desired sampling frequency and airplane speed. The half circles are built using *sin* and *cos* functions maintaining the linear velocity of the airplane. During the half-circles, to keep a certain degree of realism, a 5° roll angle is set and the yaw angle is such that the body x-axis is tangent to the circle at every sample.

A major difficulty arises in this kind of exercise whenever changing from a straight section to the half-circle one. At the point of transition, a discontinuity in the aircraft acceleration naturally arises. Since the attitude is also different in both segments, a discontinuity also occurs in the attitude angles. To ensure that the acceleration computed from the positions and the angular velocities computed from the attitude are continuous, one must ensure that the transitions between the segments are done smoothly. A B-spline smoother tool was found to provide good results in this context. Consider a set of values $\mathbf{x}$ at a discrete set of time samples. To minimize the discontinuities in the second derivative a new set of smoothed values $\mathbf{x}_s$ can be found by minimizing the following functional,

$$\mathbf{x}_s = \underset{\tilde{\mathbf{x}}_i}{\operatorname{argmin}} \left(P \sum_i \|\mathbf{x}_i - \tilde{\mathbf{x}}_i\|^2 + (1-P) \sum_i \left\| D^2 \tilde{\mathbf{x}}_i \right\|^2 \right) \tag{4.4}$$

where D is the differentiation functional.

The smoothing parameter, P, is the only choice controlling the amount of smoothing done by the method. When P=1, the method does nothing as the

smoothed points will be the same as the initial ones. When P=0, the smoothing fully minimizes the norm of the second derivative which results in a LS fit of a line to the given points. Anywhere in between is the ideal amount of smoothing which can be chosen by trial and error. More details can be seen in the documentation of the MATLAB function `csaps` from the spline toolbox. This tool is remarkably flexible and can be used for almost all imaginable trajectories one wishes to build. An example of the results obtained with this method is shown in Figure 4.4, where the roll angle around the transition point between a straight path and a half-circle path is depicted. In the former the roll angle is set to 0° and in the latter the angle is set to 5°. Here you can see the before and after smoothing where the P parameter has been chosen such that the transition spans over roughly 30 seconds of data.

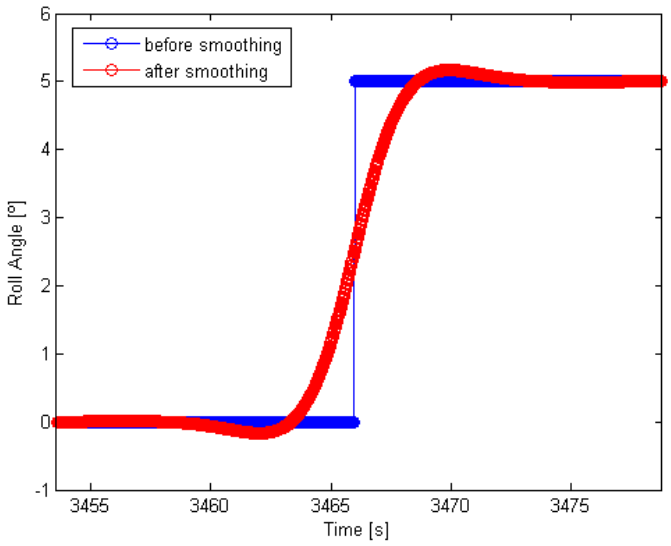

Figure 4.4: B-Spline smoother results with smoothing parameter P = 0.02

At this point, a set of geodetic coordinates describing the trajectory and a set of angles describing the attitude have been created and smoothed ensuring that no sharp discontinuities exist in the derivatives of the generated values. An abstraction of this specific flight path is now possible, and the problem becomes more general: for a given set of positions and attitude angles, how can the corresponding measurements of the IMU and GPS systems be generated?

4.2.2 Creating the IMU and GPS measurements

The IMU system uses a triad of accelerometers to measure the acceleration vector of the vehicle. The gyro triad is responsible for measuring the angular velocity vector of the platform. The hardware is aligned with the body frame and therefore it records this data in the b-frame. Typically the GPS system provides positions

in the e-frame. In the specific case of the L&R Cessna Citation II airplane, a triad of GPS antennas is placed at the fuselage, wing and nose of the aircraft which enables the post-mission computation of attitude measurements (Alberts et al., 2010). The assumption is made that GPS-attitude observations are provided as direction cosine matrices, C_b^i, describing the transformation between the b-frame and the i-frame.

Most of the equations used in this section have been seen in Section 2; however, they will be repeated when convenient.

Recalling equation Eqn. 1.3, describing the specific force $\mathbf{f}$ measurement, we will add the superscripts $\square^i$ to clarify the frame in which the variables are defined,

$$\mathbf{f}^i = \ddot{\mathbf{r}}^i - \mathbf{g}^i \tag{4.5}$$

This is the equation that defines the specific force measurements made by the accelerometer triad. There are two ingredients in this equation: the inertial acceleration of the platform, $\ddot{\mathbf{r}}^i$, and the gravitational acceleration at the accelerometer position, $\mathbf{g}^i$.

To compute the inertial acceleration, the positions of the platform in the i-frame must be computed first and then double-differentiated in time. The set of positions provided is in geodetic coordinates, $\mathbf{r}^{geo}$, and to transform them into the i-frame one must first convert them to the equivalent Cartesian set of coordinates, $\mathbf{r}^e$, as in equation Eqn. 2.37,

$$\mathbf{r}^e \equiv \begin{pmatrix} x^e \\ y^e \\ z^e \end{pmatrix} = \begin{pmatrix} (N+h)\cos\phi\cos\lambda \\ (N+h)\cos\phi\sin\lambda \\ (N\,(1-e^2)+h)\sin\phi \end{pmatrix} \tag{4.6}$$

The positions in the e-frame are then rotated into the i-frame using the transformation C_b^i. The transformation between the e-frame and the i-frame is platform independent since it is governed only by the rotation of the earth. It can be computed by expanding equation Eqn. 2.33.

$$C_i^e = R_z(-\omega_e \Delta t) = \begin{bmatrix} \cos\omega_e\Delta t & -\sin\omega_e\Delta t & 0 \\ \sin\omega_e\Delta t & \cos\omega_e\Delta t & 0 \\ 0 & 0 & 1 \end{bmatrix} \tag{4.7}$$

and the positions in the i-frame can be computed as,

$$\mathbf{r}^i = C_e^i \mathbf{r}^e \tag{4.8}$$

The angular velocity of the Earth, ω_e, is one of the defining constants of the GRS80 model published in Moritz (1992),

$$\omega_e = 7292115 \times 10^{-11}\,\text{rad/s} \tag{4.9}$$

Finally, the computed positions are double-differentiated into the inertial acceleration using the central finite differences method in equation Eqn. 2.53,

$$\ddot{\mathbf{r}}_k^i = \frac{\mathbf{r}_{k+1}^i - 2\mathbf{r}_k^i + \mathbf{r}_{k-1}^i}{l^2} \tag{4.10}$$

where,

l – is the IMU sampling time
k – is an indexation of the positions such that $\mathbf{r}_k \equiv \mathbf{r}(t_0 + kh)$

With the newly computed positions in the i-frame it is also possible to compute the normal gravity vector $\mathbf{g}^i$ with Eqn. 4.1, and all the ingredients necessary to compute the specific force measurements are ready.

At this point, the accelerometer measurements $\mathbf{f}^i$ can be computed in the inertial frame. Notice that the accelerometers measure the specific force in the b-frame and therefore the final step involves the rotation of the computed accelerometer measurements into the body frame $\mathbf{f}^b = C_i^b\,\mathbf{f}^i$. The C_i^b transformation required to do this is defined as,

$$C_i^b = C_n^b\,C_e^n\,C_i^e \tag{4.11}$$

with,

$$C_e^n = \begin{bmatrix} -\sin\phi\cos\lambda & -\sin\phi & -\cos\phi\cos\lambda \\ -\sin\phi\sin\lambda & \cos\lambda & -\cos\phi\sin\lambda \\ \cos\phi & 0 & -\sin\phi \end{bmatrix} \tag{4.12}$$

C_i^e has been computed in Eqn. 4.7 and $C_n^b = (C_b^n)^{-1}$, the attitude of the platform relative to the navigation frame, one of the inputs to this function.

The gyros in the IMU record the angular velocity of the body frame relative to inertial space in the coordinates of the body frame, $\boldsymbol{\omega}_{ib}^b$. The angular velocity must be computed from the successive attitude angles of the platform. There are as many ways of solving this problem, as ways to represent rotations all with their advantages and disadvantages. The quaternion approach will be used for its singularity-free representation. The first step is then to translate the set of C_b^i rotation matrices into their corresponding quaternion form $\mathbf{q}_i^b$. This is done by using Eqn. 2.31 and Eqn. 2.32.

The differential equation of the attitude in quaternion form can be seen in Eqn. 4.30, however, Lizarralde and Wen (1996) proposed an alternative form of this equation, which is very convenient for the calculation of the angular velocity. In the following derivation the subscripts of $\boldsymbol{\omega}_{ib}^b$ and $\boldsymbol{q}_i^b$ will be omitted for simplicity.

$$\dot{\mathbf{q}} = \frac{1}{2}E(\mathbf{q})\boldsymbol{\omega} \tag{4.13}$$

with

$$E(\mathbf{q}) = \begin{bmatrix} -q_1 & -q_2 & -q_3 \\ q_0 & q_3 & -q_2 \\ -q_3 & q_0 & q_1 \\ q_2 & -q_1 & q_0 \end{bmatrix} \tag{4.14}$$

The Jacobian, $E(\mathbf{q})$, satisfies the following properties,

$$E(\mathbf{q})^T E(\mathbf{q}) = I$$
$$E(\mathbf{q})^T \mathbf{q} = 0$$

The velocity vector can be computed then as,

$$\boldsymbol{\omega} = 2E(\mathbf{q})^T \dot{\mathbf{q}} \tag{4.15}$$

with,

$$\dot{\mathbf{q}}_i = \frac{\mathbf{q}_{i+1} - \mathbf{q}_{i-1}}{2l} \tag{4.16}$$

Finally the GPS positions and GPS attitude observations need to be generated. Typically GPS has a lower sampling rate (between 1 and 10 Hz) than the IMU system (typically 50 Hz). The GPS and IMU sampling rates are additional inputs to the dataset generation routine, but nonetheless it is assumed that GPS has a lower sampling rate.

GPS provides position measurements in the e-frame, and therefore they are copied from the already computed $\mathbf{r}^e$ appropriately down sampled. As for the attitude, the transformation matrix between the inertial and the b-frame C_b^i is also accordingly down sampled.

The accelerometers and gyros in the IMU and the GPS receivers are not perfect instruments and their measurements contain noise and other errors like biases and scale factors in the case of the inertial sensors. In the final part of this section these errors are added to the computed measurements, thus simulating the errors present in the real measurements.

According to the sensor error model in equation Eqn. 3.17 the accelerometer measurements contain a bias, a scale factor and white noise for each accelerometer. Values for these parameters are chosen a-priori for each accelerometer and added to the computed accelerometer measurements $\mathbf{f}^b$, yielding the noisy accelerometer measurements $\tilde{\mathbf{f}}^b$.

$$\tilde{\mathbf{f}}^b = \delta\mathbf{b}_a + (1 + \delta\boldsymbol{\kappa}_a)\,\mathbf{f}^b + \mu_a \tag{4.17}$$

The same procedure is done for the gyros,

$$\tilde{\boldsymbol{\omega}}_{ib}^b = \delta\mathbf{b}_g + (1 + \delta\boldsymbol{\kappa}_g)\,\boldsymbol{\omega}_{ib}^b + \mu_g \tag{4.18}$$

As for the GPS measurements, the standard deviation of the GPS positions is previously defined and the corresponding white noise realization is added to the positions,

$$\tilde{\mathbf{r}}^e_{GPS} = \mathbf{r}^e_{GPS} + \mu_r \tag{4.19}$$

The GPS attitude measurements are first transformed using a direction cosine matrix to the corresponding attitude angles according to equation Eqn. 2.19. We denote $\boldsymbol{\psi}$ as the set of obtained Euler angles. To this set of angles, a white noise realization with an a-priori defined standard deviation is added, yielding the noisy GPS attitude observations $\tilde{\boldsymbol{\psi}}$,

$$\tilde{\boldsymbol{\psi}} = \boldsymbol{\psi} + \mu_\psi \tag{4.20}$$

The attitude angles are then transformed back into the corresponding noisy direction cosine matrix $\tilde{C}^i_b$ according to Eqn. 2.18.

All of the above information is summarized and illustrated in the flowchart depicted in Figure 4.5.

4.3 Processing

In this section, the dataset gathered by the IMU and GPS is processed into a gravity disturbance vector at flight level, as indicated in Step 2 in Figure 4.1. There are three major tasks involved with this process: the computation of the GPS accelerations, the computation of the platform attitude and the estimation of the biases and scale factors in the IMU instruments. These three tasks are outlined in the following sections.

4.3.1 GPS Processing

For the processing of the GPS measurements the assumption is made that a list of GPS positions of the aircraft in the e-frame is provided. The task is now to compute the GPS accelerations in the inertial frame and the attitude of the aircraft relative to the inertial frame.

The first step is to rotate the measured position to the i-frame where the gravity disturbance vector will be computed. The position in the i-frame is simply computed by appropriately rotating the measured position in the e-frame,

$$\mathbf{x}^i = C^i_e \mathbf{x}^e \tag{4.21}$$

To compute the kinematic acceleration of the aircraft, the GPS position has to be differentiated; however, as pointed out by Kreye and Hein (2003), GPS cannot directly provide the accuracy required for airborne gravimetry without any reduction of the high-frequency noise. Several publications are dedicated to the differentiation of GPS measurements and there are two methods of computing the

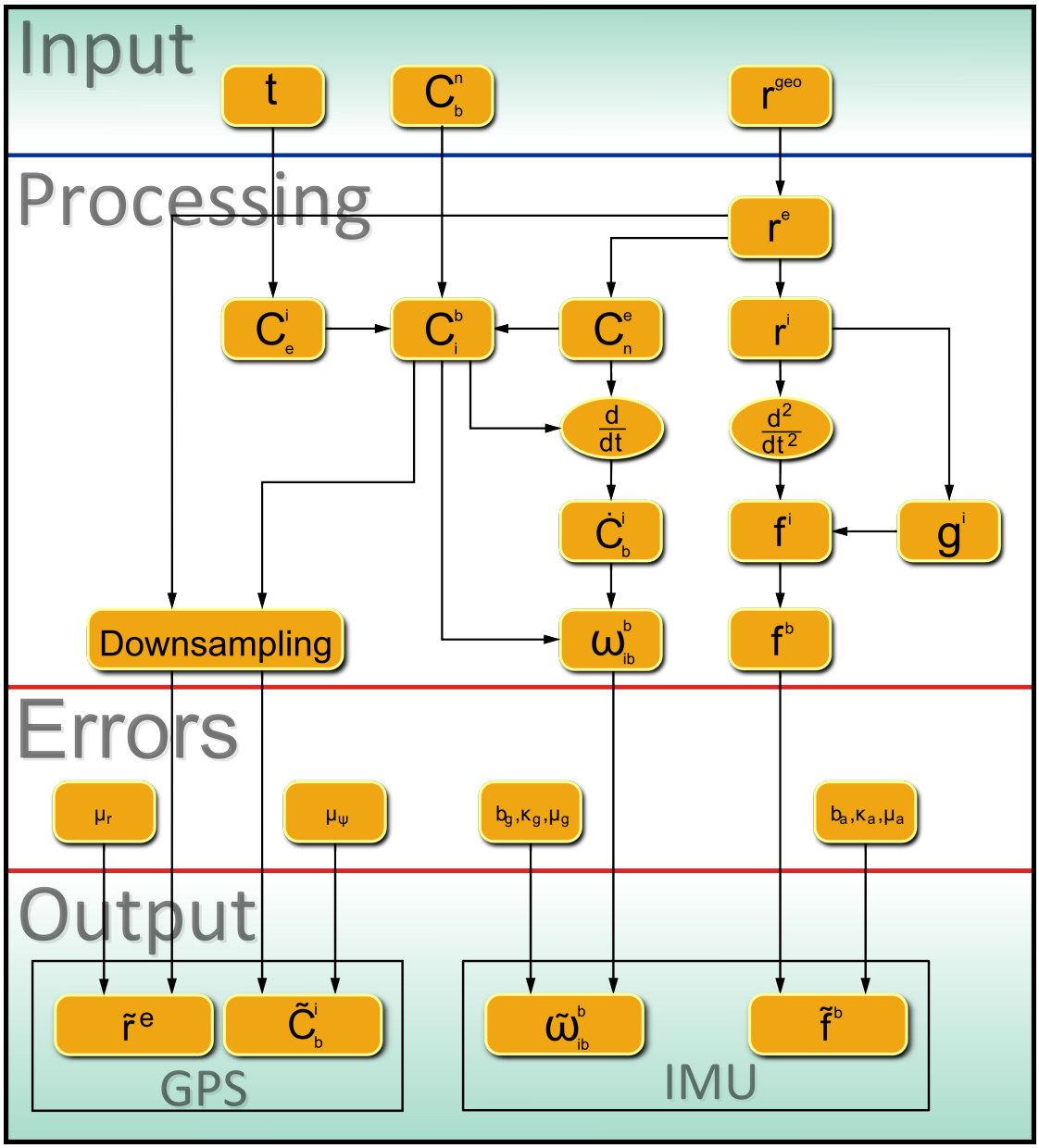

Figure 4.5: Illustration of the synthetic dataset generation. An arrow from A to B indicates B depending on A.

kinematic acceleration. Jekeli and Garcia (1997) proposed the computation of the acceleration by differentiating the phase measurements of the GPS signal instead of differentiating the computed positions. For obvious reasons, the first one is the *phase* method and the latter the *position* method. The motivation for the phase approach lies with the fact that the GPS-positions are already a quantity processed from GPS measurements, and therefore obtaining the acceleration from

the raw phase measurements is argued to be a more natural use of GPS as an acceleration sensor. The biggest advantage of the phase method is that the phase cycle slips, which affect the position determination, will not affect the precision of the computed accelerations. However in this thesis, the GPS sensor will not be modeled to the extent of generating phase measurements and therefore the option of directly differentiating the GPS positions will instead be pursued.

Bruton et al. (1999) presents an extensive study of different numerical differentiators and their performance. For its simplicity and good results the Savitzky-Golay smoothing (Savitzky and Golay, 1964) presented in this publication has been chosen for implementation. Using this technique, a polynomial is fit to the GPS positions in a LS sense, and the computation of the velocity and acceleration are straightforward from the estimated coefficients of the polynomial.

Consider the function, $f(t)$, and within this function a window of length l is defined, centered around sample f_k with an indexation $i = [-l/2 : l/2]$. To the function f inside the defined window the following polynomial of order n will be fit:

$$P_i = a_0 + a_1 i + a_2 i^2 + ... + a_n i^n \tag{4.22}$$

with the 2nd derivative,

$$\frac{\mathrm{d}P^2}{\mathrm{d}t^2} = 2a_2 + 6a_3 i + n(n-1)a_n i^{n-2} \tag{4.23}$$

Substituting for the point at middle of the window,

$$\left.\frac{\mathrm{d}P^2}{\mathrm{d}t^2}\right|_{i=0} = 2a_2 \tag{4.24}$$

Using unweighted least squares, the coefficients of the polynomial can be computed as:

$$\mathbf{a} = \left(A^T A\right)^{-1} A^T \mathbf{f} \tag{4.25}$$

where

$$\mathbf{a} = \begin{bmatrix} a_0 & a_1 & a_2 & ... & a_n \end{bmatrix}^T \tag{4.26}$$

$$\mathbf{f} = \begin{bmatrix} f_{k-\frac{l}{2}} & \cdots & f_k & \cdots & f_{k+\frac{l}{2}} \end{bmatrix}^T \tag{4.27}$$

$$A = \begin{bmatrix} \left.\frac{\mathrm{d}P}{\mathrm{d}a_0}\right|_{i=-\frac{l}{2}} & \left.\frac{\mathrm{d}P}{\mathrm{d}a_1}\right|_{i=-\frac{l}{2}} & \left.\frac{\mathrm{d}P}{\mathrm{d}a_2}\right|_{i=-\frac{l}{2}} & \cdots & \left.\frac{\mathrm{d}P}{\mathrm{d}a_n}\right|_{i=-\frac{l}{2}} \\ & & \vdots & & \\ \left.\frac{\mathrm{d}P}{\mathrm{d}a_0}\right|_{i=0} & \left.\frac{\mathrm{d}P}{\mathrm{d}a_1}\right|_{i=0} & \left.\frac{\mathrm{d}P}{\mathrm{d}a_2}\right|_{i=0} & \cdots & \left.\frac{\mathrm{d}P}{\mathrm{d}a_n}\right|_{i=0} \\ & & \vdots & & \\ \left.\frac{\mathrm{d}P}{\mathrm{d}a_0}\right|_{i=\frac{l}{2}} & \left.\frac{\mathrm{d}P}{\mathrm{d}a_1}\right|_{i=\frac{l}{2}} & \left.\frac{\mathrm{d}P}{\mathrm{d}a_2}\right|_{i=\frac{l}{2}} & \cdots & \left.\frac{\mathrm{d}P}{\mathrm{d}a_n}\right|_{i=\frac{l}{2}} \end{bmatrix} \tag{4.28}$$

There are two important details that can be used to minimize the computation time of the algorithm. First, the A matrix is independent of function $f(t)$ and therefore $(A^TA)^{-1}A^T$ needs to be computed only once. Second, since we are only interested in the acceleration vector, only the a_2 coefficient needs to be computed for each sample. Therefore only the 3$^{\text{rd}}$ line of $(A^TA)^{-1}A^T$ needs to be used in Eqn. 4.25. Computing the acceleration is then straightforward using Eqn. 4.24.

Applying this algorithm still requires the appropriate choice of the polynomial order n and the window length l. The frequency analysis of this method can be seen in the same publication (Bruton et al., 1999) and the choice of parameters is linked with the desired system resolution. The actual choice of filter parameters is discussed in Section 5.1.

At this point, a low-pass filtered set of GPS-accelerations have been computed in the i-frame.

4.3.2 IMU Processing

As pointed out in Section 1.4 the accelerometry approach will be implemented and to compute the gravity disturbance vector as in Eqn. 1.6 the specific force measurements have to be rotated into the i-frame. To do this, the transformation matrix C_b^i has to be integrated from the angular velocity measurements made by the gyros.

Starting from the differential equation of rigid body rotation Eqn. 2.50

$$\dot{C}_b^i = C_b^i \Omega_{ib}^b \tag{4.29}$$

This relation can also be expressed in quaternion form (Jekeli, 2001),

$$\dot{\mathbf{q}} = \frac{1}{2} A \mathbf{q} \tag{4.30}$$

$$A \equiv \begin{bmatrix} 0 & \omega_x & \omega_y & \omega_z \\ -\omega_x & 0 & \omega_z & -\omega_y \\ -\omega_y & -\omega_z & 0 & \omega_x \\ -\omega_z & \omega_y & -\omega_x & 0 \end{bmatrix}$$

where no confusion is anticipated by using the simplified notation $\mathbf{q} \equiv \mathbf{q}_i^b$ and $\boldsymbol{\omega} \equiv \boldsymbol{\omega}_{ib}^b$

The problem is now to integrate the above equation to obtain the attitude of platform $\mathbf{q}(t)$ at every time instant. Notice that equation Eqn. 4.29 can be expressed as

$$\dot{\mathbf{q}}(t) = \mathbf{f}(t, \mathbf{q}(t)) \tag{4.31}$$

with,

$$\mathbf{f} = \frac{1}{2} A(t) \mathbf{q}(t) \tag{4.32}$$

falling into the class of problems described in Section 2.4. Therefore the a 3^{rd}-order Runge Kutta method will be used to integrate equation Eqn. 4.30.

The considered method evaluates function $\mathbf{f}$ at three points, the integration start point t_n, the mid-point $t_{n+h/2}$ and the final point of the integration t_{n+h}. This means that a datapoint is necessary in the middle of every integration step. We denote with index l the discrete set of measurements taken by the gyros, and define the integration step size $h \equiv 2l$. One can now apply Eqn. 2.62 explicitly to the quaternion differential equation with the new index notation

$$\mathbf{q}_l = \mathbf{q}_{l-2} + \frac{h}{6}\left(\mathbf{k}_1 + 4\,\mathbf{k}_2 + \mathbf{k}_3\right) \tag{4.33}$$

$$\begin{aligned} \mathbf{k}_1 &= \mathbf{f}(t_{l-2},\, \mathbf{q}_{l-2}) \\ \mathbf{k}_2 &= \mathbf{f}(t_{l-1},\, \mathbf{q}_{l-2} + \frac{h}{2}\mathbf{k}_1) \\ \mathbf{k}_3 &= \mathbf{f}(t_l,\, \mathbf{q}_{l-2} - h\mathbf{k}_1 + 2h\mathbf{k}_2) \end{aligned} \tag{4.34}$$

Expanding each of the $\mathbf{k}$'s using the explicit expression of $\mathbf{f}$

$$\mathbf{k}_1 = \frac{1}{2}A_{l-2}\mathbf{q}_{l-2} \tag{4.35}$$

$$\begin{aligned} \mathbf{k}_2 &= \frac{1}{2}A_{l-1}\left[\mathbf{q}_{l-2} + \frac{h}{2}\left(\frac{1}{2}A_{l-2}\mathbf{q}_{l-2}\right)\right] \\ &= \frac{1}{2}A_{l-1}\left[I + \frac{h}{4}A_{l-2}\right]\mathbf{q}_{l-2} \end{aligned} \tag{4.36}$$

$$\begin{aligned} \mathbf{k}_3 &= \frac{1}{2}A_l\left[\mathbf{q}_{l-2} - h.\left(\frac{1}{2}A_{l-2}\mathbf{q}_{l-2}\right) + 2h.\left(\frac{1}{2}A_{l-1}\left[I + \frac{h}{4}A_{l-2}\right]\mathbf{q}_{l-2}\right)\right] \\ &= \frac{1}{2}A_l\left[I - \frac{h}{2}A_{l-2} + hA_{l-1}\left(I + \frac{h}{4}A_{l-2}\right)\right] \end{aligned} \tag{4.37}$$

where once again the notation has simplified with $A_l \equiv A(t_l)$ and $\mathbf{q}_l \equiv \mathbf{q}(t_l)$.

Replacing equations Eqn. 4.35, Eqn. 4.36 and Eqn. 4.37 in Eqn. 4.33 yields after simplification

$$\begin{aligned} \mathbf{q}_l = \Bigg[I + \frac{h}{12}\left(A_{l-2} + A_{l-1} + A_l\right) + \frac{h^2}{12}\left(I + \frac{h}{4}A_l\right)A_{l-1}A_{l-2} \\ + \frac{h^2}{12}A_l\left(A_{l-1} - \frac{A_{l-2}}{2}\right)\Bigg]\mathbf{q}_{l-2} \end{aligned} \tag{4.38}$$

Equation Eqn. 4.38 allows the calculation of the attitude $\mathbf{q}$ of the platform at every 2^{nd} sample of gyro data. ~Note that the algorithm requires the initial attitude $\mathbf{q}_0$ to be provided. When working with simulated dataset the initial conditions are set to their true values. When dealing with a real dataset, however, this is not possible. In this situation, special alignment procedures are done with a static

IMU until the alignment of the platform is accurately known (Jekeli, 2001, chap. 8).

Note also that the unit norm condition is not ensured by the integration method. To avoid this numerical problem in the computed attitude, the computed quaternion can be normalized at the end of every integration step in the following way

$$\mathbf{q}_l = \frac{\mathbf{q}_l}{\| \mathbf{q}_l \|} \tag{4.39}$$

Finally, the integrated quaternion $\mathbf{q}_l$ can be easily transformed into the corresponding direction cosine matrix $C^i_{b_l}$ using equation Eqn. 2.30 and the INS accelerations are rotated to the i-frame.

The routine described in this section is iterated through all datapoints in parallel with a Kalman filter estimating the errors in the inertial sensors. The used Kalman filter is outlined in the following section.

4.3.3 Kalman Filtering

The Kalman filter is one of the most successful estimation theories that has been consistently applied to numerous applications since the 60's. It is a recursive filter that estimates the state of a dynamic system from a set of noisy measurements in a statistically optimal sense. It was first developed by Rudolf E. Kalman in a publication of 1960 (Kalman, 1960). There is a very wide range of topics covered in a Kalman filter and a more specialized reference is Brown and Hwang (1997).

There are several reasons to use a Kalman filter to estimate the errors in the strapdown system instead of other estimation approaches. It allows the optimal combination of information provided by various independent sensors, and this means that it can be effectively used to combine the measurements of the GPS and IMU systems to estimate the errors in them. It is with this intention that the Kalman filter is applied in this section. The IMU error parameters are continuously changing and they need to be estimated on a per-epoch basis. With typical 50 Hz sampling rate, the number of estimated parameters rapidly becomes too big for any batch approach. Furthermore the Kalman filter is especially suited to the kind of problem at hands; the GPS system works typically at a lower rate than the IMU providing observations of the errors in the IMU. The Kalman filter is able to propagate the current estimate through time until an observation (GPS sample) becomes available. As GPS data gaps can be expected, especially for the attitude solution as seen in the GAIN flight in November 2007 (Alberts et al., 2010), the Kalman filter is flexible to accommodate these gaps in an optimal manner. Precisely for this characteristic the Kalman filter has proven results in navigation application since the 80's and more recent results in airborne gravimetry can be seen in e.g., Kwon and Jekeli (2001); Li (2007); Studinger et al. (2008).

Other techniques have been attempted such as neural networks (Wang et al., 2006) and particle filters (Gustafsson et al., 2002) but the Kalman filter remains

the standard estimation technique for airborne gravimetry as all other attempts require complicated training procedures and are not ideal (Li, 2007).

The Kalman filter has some drawbacks in that it requires precise knowledge of the dynamic model used and the noise statistics for the observations and model variables must be completely known. Too 'loose' a-priori information (the variance-covariance matrices) and the filter will diverge from the real state, too 'narrow' and the resulting estimate will be biased (Mohamed and Schwarz, 1999). In the specific case of airborne gravimetry, even if the model and noise statistics are perfectly known a-priori the Kalman filter estimates are still influenced by vehicle dynamic variations, filter tuning, environment changes, etc. (Wang et al., 2006). To relax this requirement adaptive techniques are introduced where the filter parameters are continuously adjusted to better adapt to the current conditions. Two different adaptive concepts are proposed in Mohamed and Schwarz (1999) and Li (2007) uses a Two-Stage Extended Kalman Filter implementation. In the work done in this thesis the adaptive schemes were not implemented as in the simulated environment because the models and noise statistics are not considered to change during simulation time. Nonetheless these ideas should be taken into consideration when processing any real dataset.

In the following the Kalman filter is introduced in Section 4.3.3.1 and it is then applied to the airborne gravimetry model in Section 4.3.3.2.

4.3.3.1 Kalman Filter Model

Consider the following model:

$$\mathbf{x}_k = \Phi_{k,k-1}\mathbf{x}_{k-1} + G\,\mathbf{w}_k \tag{4.40}$$

$$\mathbf{y}_k = H_k\mathbf{x}_k + \mathbf{v}_k \tag{4.41}$$

with,

$$\mathbf{w}_k \hookrightarrow \mathcal{N}(0, Q_k)$$
$$\mathbf{v}_k \hookrightarrow \mathcal{N}(0, R_k)$$

Where,

- $\mathbf{x}_k$ – is the state vector at time instant k.
- $\Phi_{k,k-1}$ – is the state transition matrix from time instant k-1 to k.
- G – is the matrix relating the random variable $\mathbf{w}_k$ with the state vector $\mathbf{x}_k$.
- $\mathbf{y}_k$ – is the observation vector at time instant k.
- H_k – is the observation matrix.
- $\mathbf{w}_k, \mathbf{v}_k$ – are zero-mean random variables with the specified Gaussian distributions.

The Kalman filter is designed on the basis of this model. The state vector $\mathbf{x}$ represents the state of the system at each point in time. The transition matrix Φ

is the matrix that determines how the state at one time influences the next state of the system. The observation vector $\mathbf{y}$ represents any form of information that can be related to the state vector through the linear relation H. The $\mathbf{w}$ and $\mathbf{v}$ vectors define the statistical nature of the state and observation vector respectively; in practice these terms are used to describe the noise in the model.

The task is now to obtain the optimal estimate $\hat{\mathbf{x}}_{opt}$ of the state vector based on the previous knowledge of $\mathbf{x}$ and of it's observations $\mathbf{y}$. First what is meant by *optimal estimate* must be properly defined. To distinguish what makes one estimate better than another a metric must be defined, a cost function which quantifies the error in the estimate. There are many kinds of cost functions but the most meaningful for the current problem is the quadratic error cost function as follows,

$$J(\hat{\mathbf{x}}, \mathbf{x}) = (\hat{\mathbf{x}} - \mathbf{x})\, Q\, (\hat{\mathbf{x}} - \mathbf{x})^T \tag{4.42}$$

where $\hat{\mathbf{x}}$ is a given estimate of the real state $\mathbf{x}$ and Q is a possible weight matrix that assigns different weights to each component of the $\mathbf{x}$ vector. Q is defined as symmetric and positive definite.

The optimal estimate $\hat{\mathbf{x}}_{opt}$ is defined as the estimate $\hat{\mathbf{x}}$ that minimizes the defined cost function. However since $\mathbf{x}$ and $\hat{\mathbf{x}}$ are random variables the minimization is done on the expected value of this function of random variables. The expectancy operator $\mathcal{E}$ is defined as,

$$\mathcal{E}(x) = \int_P \mathbf{x} \cdot f(\mathbf{x}) \mathrm{d}\mathbf{x} \tag{4.43}$$

Where,

x	–	is any random variable.
P	–	is the probability domain of x.
$f(x)$	–	is the probability density function of x.

So the explicit expression for $\hat{\mathbf{x}}_{opt}$ is found to be

$$\hat{\mathbf{x}}_{opt} = \underset{\hat{\mathbf{x}}}{\operatorname{argmin}}\ \mathcal{E}\left(J(\hat{\mathbf{x}}, \mathbf{x})\right) \Rightarrow \tag{4.44}$$

$$0 = \left.\frac{\mathrm{d}\,\mathcal{E}\left(J(\hat{\mathbf{x}}, \mathbf{x})\right)}{\mathrm{d}\hat{\mathbf{x}}}\right|_{\hat{\mathbf{x}}=\hat{\mathbf{x}}_{opt}} \tag{4.45}$$

$$0 = \left.\frac{\mathrm{d}}{\mathrm{d}\hat{\mathbf{x}}} \int_P (\hat{\mathbf{x}} - \mathbf{x})\, Q\, (\hat{\mathbf{x}} - \mathbf{x})^T f(\mathbf{x})\, \mathrm{d}\mathbf{x}\right|_{\hat{\mathbf{x}}=\hat{\mathbf{x}}_{opt}} \tag{4.46}$$

$$0 = \int_P (\hat{\mathbf{x}}_{opt} - \mathbf{x})\, Q + (\hat{\mathbf{x}}_{opt} - \mathbf{x})\, Q^T\, f(\mathbf{x})\, \mathrm{d}\mathbf{x} \tag{4.47}$$

Since Q is a symmetric matrix and $\hat{\mathbf{x}}_{opt}$ is a constant value,

$$0 = 2Q\,\hat{\mathbf{x}}_{opt} \underbrace{\int_P f(\mathbf{x})\,\mathrm{d}\mathbf{x}}_{\equiv 1} - 2Q \underbrace{\int_P \mathbf{x} f(\mathbf{x})\,\mathrm{d}\mathbf{x}}_{\equiv \mathcal{E}(x)} \Leftrightarrow \tag{4.48}$$

$$\hat{\mathbf{x}}_{opt} = \mathcal{E}(x) \tag{4.49}$$

This is the Minimum Mean Square Error (MMSE) estimator and it's usefulness lies in the fact that it is independent of the chosen Q matrix and only the knowledge of the expected value of the density $f(\mathbf{x})$ is required.

The MMSE estimator will now be applied to the model in Eqn. 4.40 and the optimal estimates of $\mathbf{x}_k$ will be obtained based on the previous state $\mathbf{x}_{k-1}$, this is the *prediction* step. When an observation $\mathbf{y}_k$ becomes available the current estimate $\mathbf{x}_k$ is updated with this new source of information, this is the *filtering* step.

The prediction step equations are obtained assuming that $\mathbf{x}_{k-1}$ is a Gaussian random variable with known expected value $\hat{\mathbf{x}}_{k-1} = \mathcal{E}(\mathbf{x}_{k-1})$ and known autocovariance matrix $P_{k-1} = \mathrm{cov}(\mathbf{x}_{k-1}, \mathbf{x}_{k-1})$. The covariance is a linear function of two random variables defined as,

$$P = \mathrm{cov}(x, y) \equiv \mathcal{E}\left[(x - \mathcal{E}(x))\left(y - \mathcal{E}(y)^T\right)\right] \tag{4.50}$$

The optimal estimate of $\mathbf{x}_k$ is given by,

$$\begin{aligned}
\hat{\mathbf{x}}_k &= \mathcal{E}(\mathbf{x}_k) \\
&= \mathcal{E}(\Phi_{k,k-1}\mathbf{x}_{k-1} + G_k\mathbf{w}_k) \\
&= \Phi_{k,k-1}\mathcal{E}(\mathbf{x}_{k-1}) + G_k\mathcal{E}(\mathbf{w}_k) \\
&= \Phi_{k,k-1}\hat{\mathbf{x}}_{\mathbf{k-1}} + 0
\end{aligned} \tag{4.51}$$

The covariance matrix is obtained then,

$$\begin{aligned}
P_k &= \mathrm{cov}(\mathbf{x}_k, \mathbf{x}_k) \\
&= \mathcal{E}\left[\left(\mathbf{x}_k - \mathcal{E}(\mathbf{x}_k)\right)\left(\mathbf{x}_k - \mathcal{E}(\mathbf{x}_k)\right)^T\right] \\
&= \mathcal{E}\left[\left(\Phi_{k,k-1}\mathbf{x}_{k-1} + G_k\mathbf{w}_k - \Phi_{k,k-1}\hat{\mathbf{x}}_{\mathbf{k-1}}\right)\left(\Phi_{k,k-1}\mathbf{x}_{k-1} + G_k\mathbf{w}_k - \Phi_{k,k-1}\hat{\mathbf{x}}_{\mathbf{k-1}}\right)^T\right] \\
&= \Phi_{k,k-1}\mathcal{E}\left[(\mathbf{x}_{k-1} - \hat{\mathbf{x}}_{\mathbf{k-1}})(\mathbf{x}_{k-1} - \hat{\mathbf{x}}_{\mathbf{k-1}})^T\right]\Phi_{k,k-1}^T + G_k\mathcal{E}(w_k w_k^T)G_k^T \\
&= \Phi_{k,k-1}P_{k-1}\Phi_{k,k-1}^T + G_kQ_kG_k^T
\end{aligned} \tag{4.52}$$

At any point an observation $\mathbf{y}_k$ of the state vector becomes available and it is necessary to *update* the current state vector $\mathbf{x}_k$ with this additional source of information. This is the filtering step and it can be formally written as the optimal

estimate of $\mathbf{x}_k$ given the observation $\mathbf{y}_k$. If we denote the updated state vector with a '+' superscript, then the following can be written,

$$\hat{\mathbf{x}}_k^+ = \mathcal{E}(\mathbf{x}_k|\mathbf{y}_k) \tag{4.53}$$

To evaluate the above expression better insight on the conditional probability density function $f(\mathbf{x}_k|\mathbf{y}_k)$ is necessary. Using Bayes' rule one can write,

$$f(\mathbf{x}_k|\mathbf{y}_k) = \frac{f(\mathbf{y}_k|\mathbf{x}_k)f(\mathbf{x}_k)}{f(\mathbf{y}_k)} \tag{4.54}$$

Notice Eqn. 4.54. Once $\mathbf{y}_k$ is known the term $f(\mathbf{y}_k)$ is a constant and only works as a scaling factor of $f(\mathbf{x}_k|\mathbf{y}_k)$ not changing its shape. We will assume that $\mathbf{x}_k$ follows an a-priori known Gaussian distribution $\mathcal{N} \hookrightarrow (\mathbf{u}_k, P_k)$.

Finally notice that Eqn. 4.41 can be rewritten in the following way,

$$\mathbf{v}_k = \mathbf{y}_k - H_k\mathbf{x}_k \tag{4.55}$$

and that once the value of $\mathbf{x}_k$ is known, and assuming that the observation noise and the state vector are independent, the probability distribution of $\mathbf{y}_k|\mathbf{x}_k$ is *equal* to the density $\mathbf{v}_k$ only *shifted* by the value $H\mathbf{x}$. Explicitly $f(\mathbf{y}_k|\mathbf{x}_k) = \mathcal{N} \hookrightarrow (H_k\mathbf{x}_k, R_k)$.

So according to Bayes' rule the density that we seek to know $f(\mathbf{x}|\mathbf{y})$ is the product of two gaussian distributions scaled by a constant. It can be shown that the product of two guassian distributions is also a gaussian distribution, scaled by a constant (see Jekeli (2001, chap. 7)) and therefore,

$$f(\mathbf{x}_k|\mathbf{y}_k) = \frac{\mathcal{N}_y(H_k\mathbf{x}_k, R_k)\,.\,\mathcal{N}_x(\mathbf{u}_k, P_k)}{K_1} \tag{4.56}$$

$$f(\mathbf{x}_k|\mathbf{y}_k) = \frac{\mathcal{N}_x\Big((P_k^{-1} + H_k^T R_k^{-1} H_k)^{-1}(H_k^T R_k^{-1}\mathbf{y} + P_k^{-1}\mathbf{u}_k), (P_k^{-1} + H_k^T R_k^{-1} H_k)^{-1}\Big)}{K_2} \tag{4.57}$$

So accordingly, the updated state vector is defined as, $x_k^+ = \mathcal{N}(u_k^+, P_k^+)$ and,

$$\mathbf{u}_k^+ \equiv \mathcal{E}(\mathbf{x}_k|\mathbf{y}_k) = P_k^+\,(H_k^T R_k^{-1}\mathbf{y} + P_k^{-1}\mathbf{u}_k) \tag{4.58}$$

$$P_k^+ \equiv \mathrm{cov}(\mathbf{x}_k|\mathbf{y}_k) = \Big(P_k^{-1} + H_k^T R_k^{-1} H_k\Big)^{-1} \tag{4.59}$$

The expression for the covariance matrix in Eqn. 4.59 requires three matrix inversions to be computed. As the size of the state vector and observation vector increase this becomes computationally heavy. The most common form of these equations introduces the Kalman gain matrix K,

$$\mathbf{u}_k^+ = \mathbf{u}_k + K(\mathbf{y} - H\mathbf{u}_k) \tag{4.60}$$

$$P_k^+ = (I - KH)P_k \tag{4.61}$$

$$K \equiv P_k H^T\Big(HP_kH^T + R\Big)^{-1} \tag{4.62}$$

where only one matrix inversion is necessary. The equivalence between both forms is shown in Section A.

So finally the Kalman filter can be resumed to the following equations. Given the previous time step estimate $\hat{\mathbf{x}}_{k-1}$ and the corresponding covariance matrix P_{k-1} the prediction step of the Kalman filter is applied to obtain,

$$\hat{\mathbf{x}}_k = \Phi_{k,k-1}\hat{\mathbf{x}}_{\mathbf{k-1}} \tag{4.63}$$

$$P_k = \Phi_{k,k-1}P_{k-1}\Phi_{k,k-1}^T + G_k Q_k G_k^T \tag{4.64}$$

When an observation $\mathbf{y}_k$ becomes available its information is used to update the current state vector. This is the update step of the Kalman filter,

$$\hat{\mathbf{x}}_k^+ = \hat{\mathbf{x}}_k + K_k(\mathbf{y}_k - H\hat{\mathbf{x}}_k) \tag{4.65}$$

$$P_k^+ = (I - K_k H_k)P_k \tag{4.66}$$

$$K_k = P_k H_k^T \Big(H_k P_k^+ H^T + R_k\Big)^{-1} \tag{4.67}$$

4.3.3.2 Application to the strapdown-GPS airborne gravimetry system.

The aim of this section is to apply the general Kalman filter model as outlined in equations Eqn. 4.40 and Eqn. 4.41 to the errors of a strapdown-GPS system. The following error dynamics formulation can be found in Kwon and Jekeli (2001). Other examples are applied for the inertial positioning method can be found in Jekeli (2001) where the author derived a general formulation of the system errors for an arbitrary frame a-frame. Salychev (1998) also derives the system error equations but specifically for the n-frame.

In the following derivation the fundamental equation of airborne gravimetry will be expressed in terms of the errors and noise of the inertial sensors. This is accomplished by systematically applying the linear perturbations method outlined in Section 2.5.

The fundamental equation of airborne gravimetry Eqn. 1.6, restated here for convenience,

$$\mathbf{g}^i = \ddot{\mathbf{x}}^i - \mathbf{f}^i \tag{4.68}$$

Perturbing the above equation yields,

$$\delta\mathbf{g}^i = \delta\ddot{\mathbf{x}}^i - \delta\mathbf{f}^i \tag{4.69}$$

The statistical model considered for the error in the GPS computed acceleration is assumed to contain only white noise,

$$\begin{aligned} \delta\ddot{\mathbf{x}}^i &= \boldsymbol{\mu}_G \\ \boldsymbol{\mu}_G &= \mathcal{N} \hookrightarrow (0, D_G) \end{aligned} \tag{4.70}$$

This is not a totally realistic assumption since the double differentiation amplifies the noise in the higher frequencies, however after appropriate low-pass filtering, the white noise approximation becomes valid (Kwon and Jekeli, 2001).

As for the error in the IMU acceleration,

$$\mathbf{f}^i = C_b^i\,\mathbf{f}^b \Rightarrow \delta\mathbf{f}^i = \delta C_b^i\,\mathbf{f}^b + C_b^i\,\delta\mathbf{f}^b \tag{4.71}$$

The term $\mathbf{f}^b$ has already been considered in Eqn. 3.17,

$$\delta\mathbf{f}^b = \mathbf{b}_a + \mathrm{diag}(\mathbf{f}^b)\boldsymbol{\kappa}_a + \boldsymbol{\mu}_a \tag{4.72}$$

The error in the computed attitude, δC_b^i, represents the small misalignment between the real transformation C_b^i and the erroneously computed one $\tilde{C}_b^i$. Using the small angle approximation in Eqn. 2.44 one can write,

$$\tilde{C}_b^i = \left(I - \Psi^i\right) C_b^i \tag{4.73}$$

where Ψ^i is the skew-symmetric matrix of the small angles vector $\boldsymbol{\psi}^i$ representing the error in the computed attitude. Substituting in the linear perturbation of C_b^i

$$\delta C_b^i \equiv \tilde{C}_b^i - C_b^i = -\Psi^i C_b^i \tag{4.74}$$

and finally substituting Eqns. 4.74 and 4.72 in Eqn. 4.71 yields

$$\delta\mathbf{f}^i = C_b^i\,\mathbf{b}_a + C_b^i\,\mathrm{diag}(\mathbf{f}^b)\boldsymbol{\kappa}_a + C_b^i\,\boldsymbol{\mu}_a - \Psi^i C_b^i\,\mathbf{f}^b$$

note that,

$$-\Psi^i C_b^i\,\mathbf{f}^b = \mathbf{f}^i \times \boldsymbol{\psi}^i \tag{4.75}$$

to obtain,

$$\delta\mathbf{f}^i = C_b^i\,\mathbf{b}_a + C_b^i\,\mathrm{diag}(\mathbf{f}^b)\boldsymbol{\kappa}_a + C_b^i\,\boldsymbol{\mu}_a + \mathbf{f}^i \times \boldsymbol{\psi}^i \tag{4.76}$$

The term $\boldsymbol{\psi}^i$ still needs to be expressed in terms of instrument errors. Let's apply the perturbation theory to Puasson's equation shown in 2.50

$$\delta\dot{C}_b^i = \delta C_b^i\,\Omega_{ib}^b + C_b^i\,\delta\Omega_{ib}^b \tag{4.77}$$

Replacing δC_b^i and $\delta\dot{C}_b^i$ with Eqn. 4.74 and its time derivative,

$$\begin{aligned}
\frac{\mathrm{d}}{\mathrm{d}t}\left(-\Psi^i C_b^i\right) &= -\Psi^i C_b^i\,\Omega_{ib}^b + C_b^i\,\delta\Omega_{ib}^b \\
-\dot{\Psi}^i C_b^i - \Psi^i\dot{C}_b^i &= -\Psi^i C_b^i\,\Omega_{ib}^b + C_b^i\,\delta\Omega_{ib}^b
\end{aligned}$$

Using again Puasson's equation, $\dot{C}_b^i = C_b^i\,\Omega_{ib}^b$, both $-\Psi^i C_b^i\,\Omega_{ib}^b$ terms cancel out and,

$$\begin{aligned}
-\dot{\Psi}^i C_b^i &= C_b^i\,\delta\Omega_{ib}^b \\
\dot{\Psi}^i &= -C_b^i\,\delta\Omega_{ib}^b C_i^b
\end{aligned}$$

which in vector form can be equivalently expressed as

$$\dot{\boldsymbol{\psi}}^{i} = -C_b^i \, \delta\boldsymbol{\omega}_{ib}^b \tag{4.78}$$

and $\delta\boldsymbol{\omega}_{ib}^b$ is the error in the angular velocity vector measured by the IMU gyros. Finally from the model of the gyro errors in Eqn. 3.17,

$$\delta\boldsymbol{\omega}_{ib}^b = \mathbf{b}_g + \mathrm{diag}(\boldsymbol{\omega}_{ib}^b)\boldsymbol{\kappa}_g + \boldsymbol{\mu}_g \tag{4.79}$$

Substituting equation Eqn. 4.79 into Eqn. 4.78 and reshaping it to matrix form we obtain the following system,

$$\frac{\mathrm{d}}{\mathrm{d}t}\begin{bmatrix}\boldsymbol{\psi}^i\\ \mathbf{b}_a\\ \mathbf{b}_g\\ \boldsymbol{\kappa}_a\\ \boldsymbol{\kappa}_g\end{bmatrix} = \begin{bmatrix}0 & 0 & -C_b^i & 0 & -C_b^i\ \mathrm{diag}(\boldsymbol{\omega}_{ib}^b)\\ 0 & 0 & 0 & 0 & 0\\ 0 & 0 & 0 & 0 & 0\\ 0 & 0 & 0 & 0 & 0\\ 0 & 0 & 0 & 0 & 0\end{bmatrix} \cdot \begin{bmatrix}\boldsymbol{\psi}^i\\ \mathbf{b}_a\\ \mathbf{b}_g\\ \boldsymbol{\kappa}_a\\ \boldsymbol{\kappa}_g\end{bmatrix} + \begin{bmatrix}-C_b^i & 0 & 0 & 0 & 0\\ 0 & 0 & 0 & 0 & 0\\ 0 & 0 & 0 & 0 & 0\\ 0 & 0 & 0 & 0 & 0\\ 0 & 0 & 0 & 0 & 0\end{bmatrix} \cdot \begin{bmatrix}\mu_g\\ 0\\ 0\\ 0\\ 0\end{bmatrix} \tag{4.80}$$

where the biases and scale factors of the inertial sensors are modeled as random constants, e.g., $\dot{b}_a = 0$. Every 0 in the matrices represents a [3x3] null matrix and every zero in the vector represents a [3x1] null vector.

The form of the equation Eqn. 4.80 is typically the starting point of any Kalman filter implementation. This is due to the fact that the above system of first-order differential equations can be rewritten as,

$$\dot{\mathbf{x}}(t) = F(t)\mathbf{x}(t) + G(t)\boldsymbol{\mu}(t) \tag{4.81}$$

This differential equation can be solved for $\mathbf{x}(t)$ and evaluated at a discrete set of points as,

$$\mathbf{x}(t+\delta t) = \Phi_{t+\delta t,t}\mathbf{x}(t) + \mathbf{w}(t) \tag{4.82}$$

where the transition matrix Φ as seen in the Kalman filter model in Eqn. 4.40 has appeared in the solution. Considering the high sampling rate of the INS, the following first order solutions are accurate,

$$\Phi = e^{F\delta t} \approx I + F\delta t \tag{4.83}$$

$$\mathbf{w}(t) \hookrightarrow \mathcal{N}(0, GD_g\delta tG^T) \tag{4.84}$$

More details on discretization of the continous system can be seen in Jekeli (2001, chap. 7.4).

At this point it is still necessary to define which observations will be used in the Kalman filter and apply the filter observation model in Eqn. 4.41.

The observations that will be used in the Kalman filter are the differences between the accelerations provided by the INS and GPS systems and the differences

between the integrated INS attitude and the GPS attitude measurements. The differences between both systems expose the low-frequency errors in the IMU and allow the Kalman filter to estimate them correctly. This will be done formally in the following paragraphs. Consider the following observation model,

$$\mathbf{y}_1 = \tilde{\mathbf{f}}^i - (\tilde{\ddot{\mathbf{x}}}^i - \tilde{\boldsymbol{\gamma}}^i) \tag{4.85}$$

where,

- $\mathbf{y}_1$ – is the acceleration residual.
- $\tilde{\mathbf{f}}^i$ – is the measured INS acceleration.
- $\tilde{\ddot{\mathbf{x}}}^i$ – is the computed GPS kinematic acceleration.
- $\tilde{\boldsymbol{\gamma}}^i$ – is the gravity model in Section 4.1 evaluated at the GPS indicated position.

Expanding the computed variables in terms of their errors and their true value,

$$\mathbf{y}_1 = \mathbf{f}^i + \delta\mathbf{f}^i - (\ddot{\mathbf{x}}^i + \delta\ddot{\mathbf{x}}^i - \boldsymbol{\gamma}^i - \delta\boldsymbol{\gamma}^i)$$

and using equation Eqn. 4.68,

$$\mathbf{y}_1 = \delta\mathbf{f}^i - \delta\ddot{\mathbf{x}}^i + \delta\boldsymbol{\gamma}^i + \underbrace{\boldsymbol{\gamma}^i - \mathbf{g}^i}_{\equiv -\Delta\mathbf{g}^i}$$

$$\mathbf{y}_1 = \delta\mathbf{f}^i - \delta\ddot{\mathbf{x}}^i + \delta\boldsymbol{\gamma}^i - \Delta\mathbf{g}^i \tag{4.86}$$

In Eqn. 4.86, $\delta\mathbf{f}^i$ reflects the error in the INS system and this term is expanded with Eqn. 4.76. $\delta\ddot{\mathbf{x}}^i$ reflects the errors in the computed GPS acceleration and this term has been modeled as white-noise in equation Eqn. 4.70. The term $\delta\boldsymbol{\gamma}^i$ translates the error in the computed normal gravity vector and with the considered model in Section 4.1, this error can be explicitely written as,

$$\delta\boldsymbol{\gamma}^i = \frac{\mathrm{d}\boldsymbol{\gamma}^i}{\mathrm{d}\mathbf{r}^i}\delta\mathbf{r}^i_{GPS} = \Gamma^i\,\delta\mathbf{r}^i_{GPS} \tag{4.87}$$

The highest value of the gravitational tensor, Γ^i, happens along the radial direction near the surface of the Earth and is approximately 0.3×10^{-5} m/s^2/m change in the gravity vector. This means that a positioning error of 1 m in the radial direction will cause an error in the observations of about 0.3 mGal and since DGPS accuracies are well below the 1 m level, the error $\delta\boldsymbol{\gamma}^i$ is small enough to be left unmoddeled.

As for the term $\Delta\mathbf{g}^i$ it represents the difference between the model and the real gravity vector. This is called the *gravity disturbance* vector and it is precisely the quantity we wish to measure. Following the approach taken by Kwon and Jekeli (2001) and as pointed in Section 1.4, no stochastic model of the gravity disturbance vector will be introduced in the Kalman filter and therefore this term will be left unmodeled. The observation model is then finally written as,

$$\mathbf{y}_1 + \Delta\mathbf{g}^i = C^i_b\,\mathbf{b}_a + C^i_b\,\mathrm{diag}(\mathbf{f}^b)\boldsymbol{\kappa}_a + C^i_b\,\boldsymbol{\mu}_a + \mathbf{f}^i \times \boldsymbol{\psi}^i - \boldsymbol{\mu}_G \tag{4.88}$$

The next observation, $\mathbf{y}_2$, is the difference between the IMU integrated attitude and the GPS attitude observations and it is an innovation introduced in this thesis. The attitude error $\boldsymbol{\psi}^i$ is obtained from the the difference between the INS and GPS attitude matrices. At every GPS epoch, the $C^i_{b_{\text{GPS}}}$ solution is compared to the integrated attitude matrix $C^i_{b_{\text{INS}}}$ and the difference between both can be seen as the rotation δC such that,

$$\begin{aligned} C^i_{b_{\text{INS}}} &= \delta C\, C^i_{b_{\text{GPS}}} \\ \delta C &= C^i_{b_{\text{INS}}}\, C^b_{i_{\text{GPS}}} \end{aligned} \tag{4.89}$$

Having computed δC it can be transformed into the small angle vector $\boldsymbol{\psi}^i$ using equation Eqn. 2.19. The statistical model for the observations is then,

$$\mathbf{y}_2 = \boldsymbol{\psi}^i + \mu_\psi \tag{4.90}$$

Gathering both observation vectors from equations Eqn. 4.90 and Eqn. 4.88 and expressing them in matrix form,

$$\begin{bmatrix} \mathbf{y}_1 \\ \mathbf{y}_2 \end{bmatrix} = \begin{bmatrix} [\mathbf{f}^i\times] & C^i_b & 0 & C^i_b\,\text{diag}(\mathbf{f}^b) & 0 \\ I & 0 & 0 & 0 & 0 \end{bmatrix} \cdot \begin{bmatrix} \boldsymbol{\psi}^i \\ \mathbf{b}_a \\ \mathbf{b}_g \\ \boldsymbol{\kappa}_a \\ \boldsymbol{\kappa}_g \end{bmatrix} + \begin{bmatrix} \mathbf{v}_1 \\ \mathbf{v}_2 \end{bmatrix} \tag{4.91}$$

with,

$$\mathbf{v}_1 \hookrightarrow \mathcal{N}(0, D_G + C^i_b\, D_a C^b_i) \tag{4.92}$$

$$\mathbf{v}_2 \hookrightarrow \mathcal{N}(0, D_\psi) \tag{4.93}$$

which can be written in more compact form as,

$$\mathbf{y}_k = H\mathbf{x}_k + \mathbf{v}_k \tag{4.94}$$

Notice that equation Eqn. 4.94 is already suited to the Kalman filter observation model as expressed in Eqn. 4.41.

At this point the Kalman filter model has been defined for a strapdown/GPS system and, remembering Section 4.3.3.1, the system error state vector is propagated through time using the prediction equations. As soon as a GPS observation is available, an observation of the system state, $\mathbf{y}_k$, can be computed and the filtering equations are applied.

It is important to note that the observation model used in the Kalman filter (see equations Eqn. 4.80 and Eqn. 4.91) are obtained from the linearization of a non-linear model. The most obvious implication of this fact is that these models are only adequate within a small neighborhood of the linearization point, or more accurately when $\mathbf{x}_k \approx 0$. In general, the gyro measurements contain a bias error

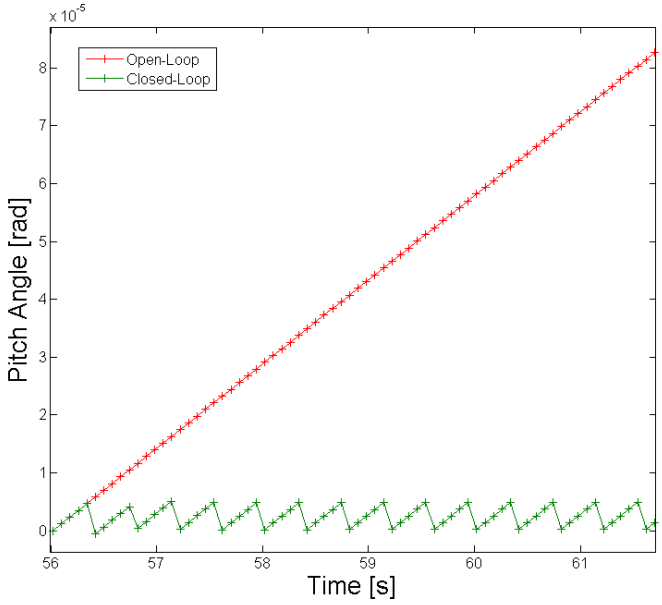

Figure 4.6: The difference between the computed and the GPS observed pitch angles for a open and closed-loop estimation schemes.

and the integrated attitude will continually drift away from the real attitude which, if left uncorrected, will very soon leave the validity region of the linearized models, and the Kalman filter will diverge from the real state. To avoid this problem we will use the *Closed-Loop Estimation* (Jekeli, 2001, chap. 7) where after each observation the estimated attitude error is used to correct the attitude integrator. An illustration of this is given in Figure 4.6 where the difference between the computed and the GPS observed pitch angle is plotted for the open and closed-loop approaches. As you can see, due to the bias in the pitch gyro, the integrated pitch angle continually departs from the unbiased GPS measurement. With a closed-loop approach, the integrator is reset to the best estimate of the pitch angle whenever a GPS observation is available.

Consider that at time instant $t = t_k$ a GPS observation is available, the observation vector $\mathbf{y}_k$ has been computed, and the update state $\mathbf{x}_k^+$ is determined. The first three components of the state vector $\mathbf{x}_k^+$ represent the estimate of the attitude error $\hat{\boldsymbol{\psi}}_k^i$ and they are used to reset the current integrated attitude $\tilde{C}_{b_k}^i$. First transform the estimated attitude error $\hat{\boldsymbol{\psi}}_k^i$ into the corresponding DCM, δC, using Eqn. 2.18. Now reset the integrated attitude matrix $\tilde{C}_{b_k}^i$ according to Eqn. 4.74,

$$\tilde{C}_{b_k}^{i+} = \delta C^T \tilde{C}_{b_k}^i \tag{4.95}$$

and reset the state vector,

$$\psi_k^{i+} = \begin{bmatrix} 0 & 0 & 0 \end{bmatrix}^T \tag{4.96}$$

Before the Kalman filter is fully specified one must define the initial conditions and the variance-covariance matrices of the observations and model. The initial state is set to 0's and the initial autocovariance matrix was tuned to the values seen in Table 4.2. The Q and R matrices that describe the errors in the model and measurements are shown in Table 4.3 and Table 4.4 respectively.

The state covariance matrix, P_0, was first approximated by squaring the repeatability parameters given by the instrument datasheets (see Table 3.4) and squaring the expected accuracy of the GPS-attitude system found later in this thesis in Table 5.2. After this initial approximation the P_0 matrix is empirically tuned to maximize the performance of the obtained results, a common procedure whenever Kalman filters are used.

The scaling parameters found in the R matrix intend to approximate the attenuation of the errors in the INS and GPS accelerations due to low-pass filtering, where W represents the length of the low pass filter used. These scaling parameters have been also empirically determined using a small set of different length low pass filters.

Notice how the Q and R matrices are expressed in terms of the dispersion matrices of each of the models considered for the accelerometers, gyros, GPS-positioning and GPS-attitude. Later on, simulations will be run for different noise levels of each instrument, and instead of tuning the Kalman filter to each specific combination of the noise in each dataset, the specified filter is tuned for all the datasets and low pass filters used.

Table 4.1: Initial State Vector $\mathbf{x}_0$.

		X	Y	Z	Unit
Attitude Error	$\boldsymbol{\psi}^i$	0	0	0	rad
Acc Bias	$\mathbf{b}_a$	0	0	0	mGal
Gyro Bias	$\mathbf{b}_g$	0	0	0	deg/hr
Acc Scale Factor	$\boldsymbol{\kappa}_a$	0	0	0	
Gyro Scale Factor	$\boldsymbol{\kappa}_g$	0	0	0	

Table 4.2: Diagonal of Initial State Dispersion Matrix P_0.

		X	Y	Z	Unit
Attitude Error	$\boldsymbol{\psi}^i$	0.01	0.01	0.01	deg^2
Acc Bias	$\mathbf{b}_a$	100	100	100	mGal^2
Gyro Bias	$\mathbf{b}_g$	400	400	400	deg^2/hr^2
Acc Scale Factor	$\boldsymbol{\kappa}_a$	1×10^{-16}	1×10^{-16}	1×10^{-16}	
Gyro Scale Factor	$\boldsymbol{\kappa}_g$	1×10^{-16}	1×10^{-16}	1×10^{-16}	

Table 4.3: Diagonal of Model Noise Covariance Matrix Q.

		X	Y	Z
Attitude Error	$\boldsymbol{\psi}^i$	D_{g_x}	D_{g_y}	D_{g_z}
Acc Bias	$\mathbf{b}_a$	0	0	0
Gyro Bias	$\mathbf{b}_g$	0	0	0
Acc Scale Factor	$\boldsymbol{\kappa}_a$	0	0	0
Gyro Scale Factor	$\boldsymbol{\kappa}_g$	0	0	0

Table 4.4: Diagonal of Observation Noise Covariance Matrix R.

		X	Y	Z
Acceleration Difference	$\mathbf{y}_1$	$C_b^i D_a C_i^b (\frac{4}{80.W})^2 + D_G (\frac{1}{10W})^2$		
Attitude Difference	$\mathbf{y}_2$	D_ψ		

5 The Simulations

In this chapter the results obtained from different simulations will be presented. First, the resolution of the system will be defined and an appropriate low-pass filter will be presented that is used to remove the high-frequency noise of the GPS and IMU measurements. After that we will look at the results of the Kalman filter and draw some conclusions on how to correct the low-frequency errors in the IMU system. Finally, the computed gravity disturbance values are computed and conclusions about the expected performance of the system can be made.

If a need to improve the airborne gravimetry system exists, then it becomes very important to know where efforts should be placed in order to maximize the improvement in the overall accuracy of the system. To understand which parts of the system play a bigger role in the overall error budget an analysis is done on the sensitivity of the system's accuracy to different precisions of the measurements taken by the IMU and GPS systems. Conclusions can then be made about which parts of the system should be improved in the future.

While hardware improvements can become extremely expensive or even impossible in the near future, additional concepts are also studied which could have an impact on the accuracy of the system. Multi-sensor, multi-pass systems and different vehicle speeds are considered with the goal of achieving the 0.5 mGal accuracy.

There are many different hardware solutions for INS systems with the consequence of many different configurations. Because the GAIN IMU is still under development, specific information about sampling frequencies not yet available. There isn't a predefined optimal sampling frequency for the inertial sensors to work. One of the strapdown datasets which has been used by many publications (Wei and Schwarz, 1998; Jekeli, 2001, to name a few) has been recorded at 50 Hz for the IMU and 2 Hz for the GPS system. In another publication Salychev et al. (2000) describes a strapdown system outputting inertial data at 46 Hz and GPS at 1 Hz. Meyer et al. (2003) shows a 50 Hz INS with 1 Hz GPS. These two parameters are configurable in the implemented software, but for the simulations the chosen values are similar to the ones here mentioned. The values used in the simulations consider IMU measurements taken at 50 Hz and GPS measurements taken at 2.5 Hz. This means that every 20 INS samples a GPS sample is expected.

In the following simulations a 100 km flight path is used as shown in Figure 5.1. The trajectory of the airplane is plotted in the black line over the gravity disturbance surface. The profile was flown with constant 220 Km/h speed at constant altitude of 2 Km. The airplane is at steady leveled flight with the body x-axis pointing in the direction of movement and the z-axis pointing towards the Earth

along the local vertical direction.

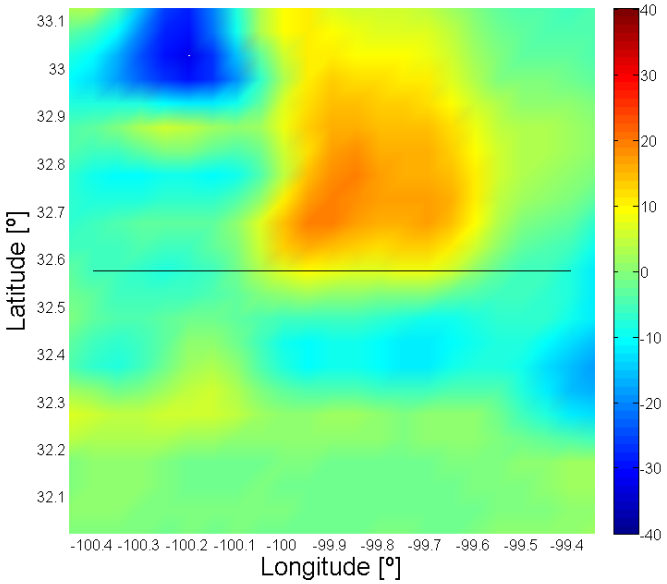

Figure 5.1: The 100 km flight path simulated in the presented results plotted over a colormap of the vertical gravity disturbance.

Ideally through calibration the instrument biases would be known a-priori. However, since these parameters change with temperature, time and other factors errors representing these deviations from the calibrated state are introduced in the simulated instruments as mentioned in Section 4.2.2. The following biases are added to the instruments' measurements where the values were chosen to be within the repeatability specifications stated by the manufacturer and depicted in Table 3.4. By doing this it will be possible to demonstrate the capability of the Kalman filter to identify these residual biases of each instrument and correct them effectively when processing the data.

Table 5.1: Biases added to the INS measurements.

	ACC		GYRO	
x^b	10	mGal	3.0	deg/hr
y^b	40	mGal	-3.0	deg/hr
z^b	-20	mGal	1.5	deg/hr

One simplification made here is that no scale factor errors will be introduced in the dataset. The reason to do so is related to the trajectory of the airplane. Since the airplane's attitude is kept constant relative to the navigation frame and no changes in the acceleration's occur in the data, the forces and angular velocities acting on each of the body axes are approximately constant during the whole flight.

Noticing the sensor errors model in equation Eqn. 3.17, if the accelerations and angular velocities are constant, then the error introduced by the scale factor term is also constant and therefore indistinguishable from a bias. Being indistinguishable, nothing will be gained by trying to estimate them and the option was taken to leave out of the measurements. Accordingly, since no scale-factor errors are introduced in the data, the scale-factor errors $\delta\kappa$ *will not be estimated* in the Kalman filter.

Finally it is necessary to define the level of noise in each of the measurements within the airborne gravimetry system. This is presented in table Table 5.2. These values reflect the expected performance level of the GAIN SINS/DGPS system.

Table 5.2: White noise realizations added to the measurements.

Measurement	Source	STD of the noise	
Accelerometer	Honeywell (2010)	$\sigma(\boldsymbol{\mu}_a)$	$<70\,\text{mGal}$
Gyro	Fizoptika (2010)	$\sigma(\boldsymbol{\mu}_g)$	$<2.95\times10^{-3}\,^\circ/\text{s}$
GPS Position	Personal communication with MGP	$\sigma(\mathbf{r})$	$<1\,\text{cm}$
GPS Attitude	Alberts et al. (2010)	$\sigma(\boldsymbol{\psi})$	$<0.1^\circ$

Whenever two simulations are compared the seed of the random generator is the same for all of them. This means that the actual noise realization is the same for both simulations.

5.1 Low-Pass Filtering

Before processing the IMU and GPS data in the Kalman filter the high frequency noise has to be removed from the measurements. The low pass filter used in the simulations is the Savitzky-Golay smoother presented in Section 4.3.1. Recalling the content of that section, it was stated that the GPS accelerations are computed by fitting a n^{th}-order polynomial to the set of GPS-positions spread over an l-second window. Equivalent low-pass filtering has to be used on the IMU specific force measurements for consistency.

If the position of the platform is assumed to be a n^{th}-order polynomial, then the acceleration of the platform is a $(n-2)^{\text{th}}$-order polynomial because $a(t) \equiv \frac{\mathrm{d}^2\mathbf{r}(t)}{\mathrm{d}t^2}$. The equivalent low-pass filter used in the INS specific force measurements is then a $(n-2)^{\text{nd}}$-order with an l second window Savitzky-Golay smoother.

The parameters of the low-pass filter, the window length l and the filter order n have to be chosen. The most important factor is the design of the low-pass filter is the cutoff frequency. Different applications of airborne gravimetry require different resolutions, but the goal is set to have an airborne gravimetry system with enough accuracy for any application, and as seen in Chapter 1 the most demanding application is natural resource exploration which requires a system resolution of at least 2 Km.

The resolution of an airborne gravimetry system has two limiting factors. In the cross-track direction the system is limited by the spacing between consecutive

flight lines. In the along track component the system is limited by the ratio between airplane speed and the cutoff frequency of the low-pass filter (Bruton, 2000). The Cessna Citation II airplane has a nominal speed of 220 Km/hr, and if the resolution of the system is defined at 2 Km, than this equates to a cutoff frequency of 1.53×10^{-2} Hz. Three low-pass filters have been designed to match this cutoff frequency: a 5^{th}-order filter with 110 s length, a 15^{th}-order filter with 315 s length and a 25^{th}-order filter with 480 s length. The frequency response of these filters shown shown in Figure 5.2.

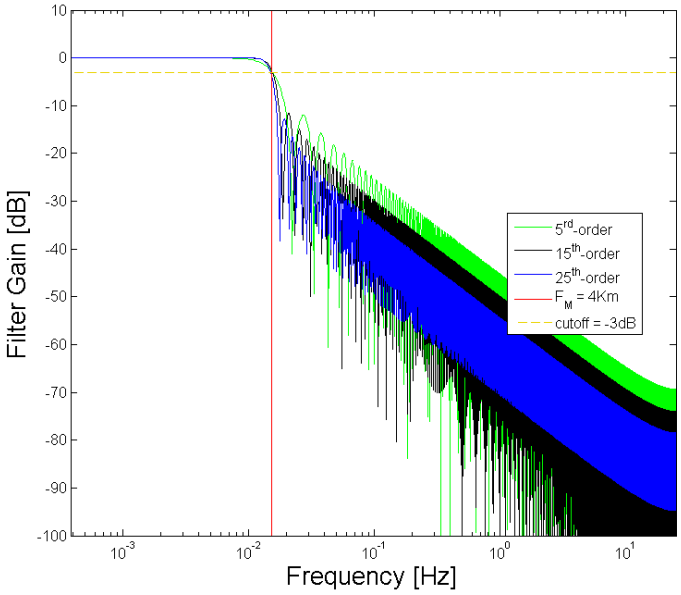

Figure 5.2: Comparison of low-pass filters with 5^{th}, 15^{th} and 25^{th}-order polynoms.

In this figure it can be seen that the higher order filters have a sharper transition between the pass- and stop-bands, which results in a higher attenuation of the unwanted signal. Bruton et al. (1999) have obtained the best results with 25^{th}-order filters, however this leads to a comparatively large filter length which results in some numerical instability of the method and larger amounts of unprocessed data. For this reason, and since simplistic white noise is being used, the 5^{th}-order filter will be used during the simulations. In a real dataset the actual implementation of the low-pass filter will depend on the assumptions made about the noise in the data and the frequency content of the gravity disturbance vector, which is also related to the actual vehicle speed and to the application requirement. The 5^{th}-order filter is deemed appropriate for the current simulations and additional, more sophisticated filter designs are not pursued in the context of this thesis.

In the simulation plots it will be noticeable that the simulation starts at not a t=0 s but a few seconds later. The explanation for this is related to the width of the low pass filter used in the GPS and IMU measurements. To compute the

kinematic acceleration at any point a number of GPS positions centered around this point is required where the actual number of samples depends on the filter length, as described in Section 4.3.1. The start of the simulation is then only possible at t = $l/2$ s where l is the filter length in seconds.

5.2 Kalman Filter Results

In this section a comparison will be established between the results of the *normal dataset* and the *perfect dataset*. The normal dataset is the one that reflects the expected noise from the hardware that will be used in the real system as seen in Table 5.2. To the perfect dataset no noise is added to the measurements, reflecting an ideal strapdown airborne gravimetry system.

The comparison between both datasets is done for two reasons: the perfect dataset illustrates the correct functioning of the software. Secondly, by comparing the normal dataset with the perfect one, some conclusions can be drawn about the observability of certain estimated components.

5.2.1 Estimated Gyro Biases

The estimated gyro biases are depicted in Figure 5.3. It can be seen that for the perfect dataset they are immediately well estimated. As for the normal dataset they rapidly converge to their true values except, the yaw gyro bias, which is the least observable one as it requires the most time to settle around the correct value.

The yaw bias is the least observable because, in a leveled flight, a change in the yaw angle does not change the orientation of the gravity vector in the b-frame and therefore no error in the residual acceleration can be observed.

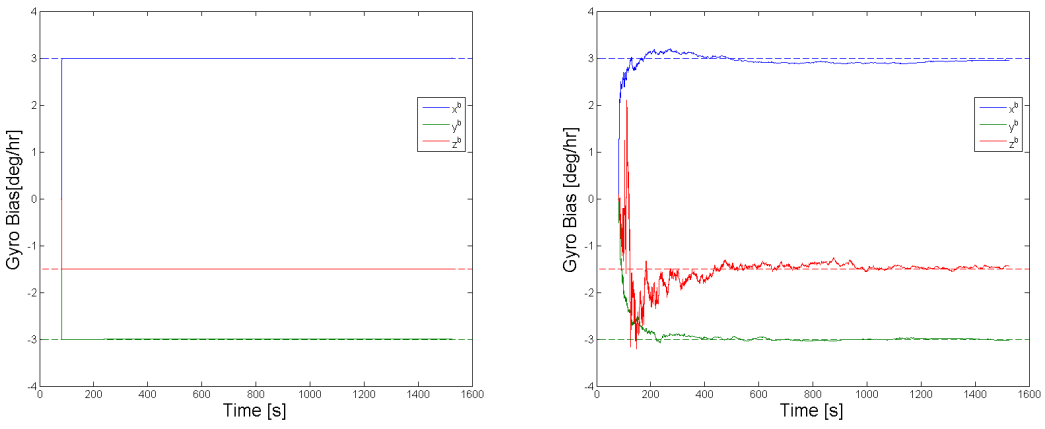

(a) Perfect Dataset

(b) Normal Dataset

Figure 5.3: Gyro Biases estimated by the Kalman filter. The dashed line represents the true errors introduced in the synthetic dataset.

5.2.2 Estimated Accelerometers Biases

For the correct interpretation of the results it is necessary to notice that the x- and y-accelerometers are kept horizontal and the z-accelerometer is kept in the vertical during the simulations, because the b-frame is leveled with the n-frame (see Section 4.2.1). The major difference between the horizontal and vertical accelerometers is that only the latter is exposed to the gravity signal.

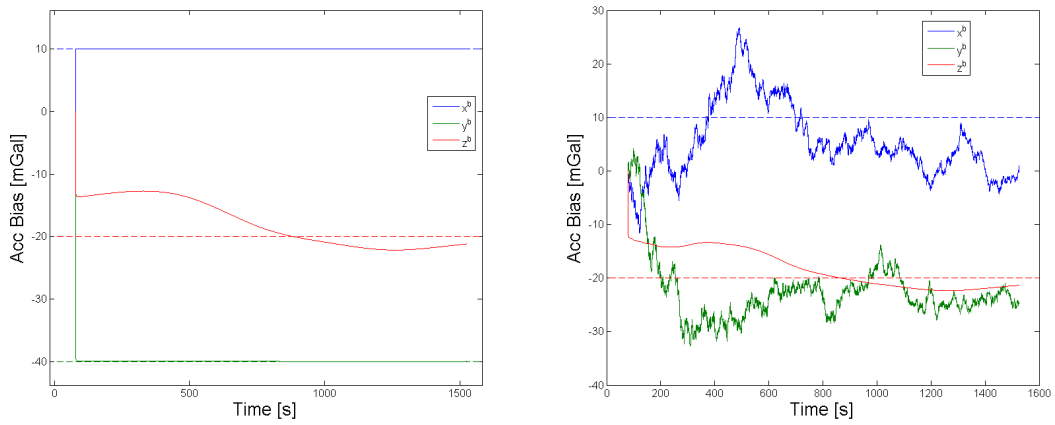

(a) Perfect Dataset

(b) Normal Dataset

Figure 5.4: Accelerometer biases estimated by the Kalman filter. The dashed lines represent the true errors introduced in the synthetic dataset.

Looking at Figure 5.4a it is seen that the horizontal biases immediately converge to their real values. The vertical bias, however, seems to wander around the true value. Since in the perfect dataset there are no measurement errors, this deviation is attributed to the gravity disturbance felt along the vertical axis. Recall the observation equation (Eqn. 4.88), where the gravity disturbance error $\Delta\mathbf{g}^i$ was left unmodeled, and this unmodeled signal is now disturbing the estimation of the vertical bias. To illustrate this argument consider Figure 5.5. The real accelerometer bias is plotted as the red dashed line, constant at -20 mGal. The accelerometer biases were modeled in the Kalman filter as random constants (Eqn. 4.80) and therefore the filter estimates them by simply averaging the error along the respective channel. If the only error source was the -20 mGal accelerometer bias then this process would work perfectly; however, for the vertical channel, the error is not only the z-accelerometer bias but also the gravity disturbance signal and therefore the estimated bias follows the average gravity disturbance. This can seen by comparing the estimated bias (red line) with the average of the error (green line).

A very thorough study of bias estimation applied to real data can be found in Bruton et al. (1999), where the author has used a similar Kalman filter without any stochastic assumptions for the gravity disturbance. The author realizes the

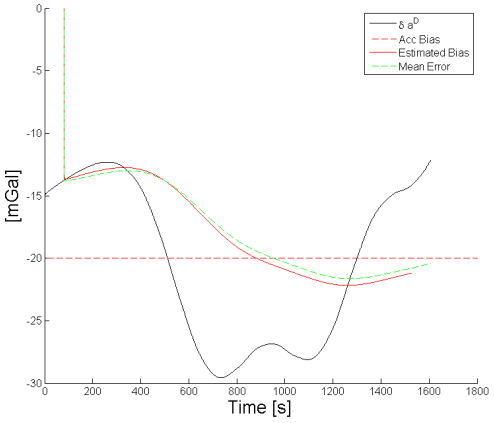

Figure 5.5: Estimated bias (red) follows the mean of the error along the vertical channel (green)

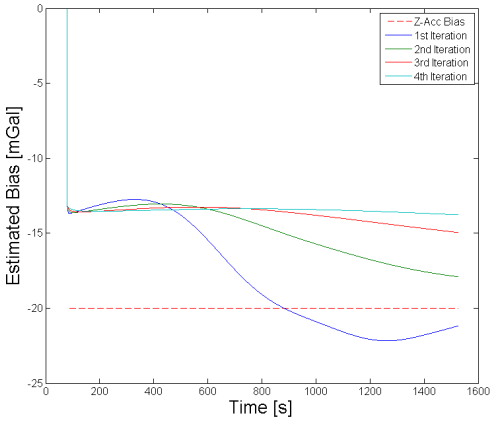

Figure 5.6: The iterative approach applied to the vertical bias estimation. The real bias is depicted with red dashed line.

accelerometer biases from real flight data were not constant and not even linear. Several stochastic models were attempted as bias models with limited success. The author finally argues that the gravity disturbances might be affecting the vertical bias estimation, in a manner all similar to the perfect dataset results, and an iterative approach is proposed to tackle this difficulty:

1. Run the Kalman filter to estimate the accelerometer biases and obtain a first approximation of the gravity disturbance.

2. Rerun the Kalman filter and, to the normal gravity model, add the approximate gravity disturbance obtained in the previous step, thus removing it from the filtering process. The rationale for this is that by including more information about the gravity field in the estimation process the accelerometer biases should be more accurately estimated.

3. This process is iterated until the differences between consecutive gravity disturbances are smaller than a threshold value.

This iterative process has been attempted with the perfect dataset and the results are plotted in Figure 5.6. Notice how with each iteration the estimated bias progresses towards a constant value; however, the final estimate of any iteration still differs from the real one by a constant and therefore the real value is not still not correctly estimated which was the motivation for using this method in the first place.

Estimating the accelerometer bias correctly through the specified Kalman filter is only feasible if it can be completely separated from the gravity disturbance. However, as pointed out by Jekeli (2001), this is still the case with any other Kalman approach, even when using the most sophisticated stochastic models of

the gravity disturbance. The stochastic nature of the gravity disturbance has to be different from that of the sensor errors in a way that the Kalman filter is able to distinguish them correctly. In practice, this means that, in these simulations the accelerometer biases are not distinguishable from the average gravity disturbance value. To obtain the correct bias, external information is required to correctly estimate the vertical accelerometer bias. This will be discussed in Section 5.3

Examining the results of the normal dataset in Figure 5.4b, the vertical channel is very observable and follows the expected trajectory as seen in the perfect dataset. As for the horizontal biases, they are much less observable and they do not seem to converge to their real values. Jekeli (2001, chap. 5.4) points out that in stabilized platforms, aligned with the navigation frame, the horizontal biases are indistinguishable from a horizontal attitude error, a *tilt* error. If a small error in the computed roll angle exists it will introduce a component of the gravity vector into the y-accelerometer. In the same way, a bias in the y-accelerometer can be translated into an error in the roll angle of the platform attitude. This is true for stabilized platforms, slaved to the navigation frame, but a strapdown system can make use of special maneuvers that will expose the horizontal accelerometer biases. In the performed simulations, despite using a strapdown IMU, the attitude of the platform was kept aligned with the navigation frame, the conditions under which the horizontal biases become unobservable.

The only way of decoupling the tilt error from the horizontal biases is by using external information such as the GPS-attitude measurements. Unfortunately, as seen in the results of the normal dataset, the accuracy of the GPS-attitude is not enough to estimate the correct values of the accelerometer biases. To illustrate this, notice Figure 5.7 where the estimated y-bias is plotted for different accuracies of the GPS-attitude observations. It is obviously seen that increasing the accuracy of the GPS-attitude measurements allows the correct estimation of the accelerometer biases. This will be seen with more detail in Section 5.5.4.

5.3 Correcting the IMU Measurements

At the end of the Kalman filter processing, the biases of the gyros and accelerometers have been estimated and it is now time to correct the IMU measurements before computing the gravity disturbance vector.

Since a closed-loop estimation (page 76) has been used, the attitude of the IMU is continuously corrected by the latest Kalman filter estimate. At the end of the processing the integrated attitude is already corrected and reflects the best estimate of the real attitude of the platform.

The accelerometer biases were modeled as random constants in the Kalman filter and therefore the IMU specific force measurements are corrected by subtracting the final estimate of the filter. The final estimate represents the most accurate knowledge of the constant bias along the respective b-frame axis. However, as seen in Section 5.2.2 the vertical bias is not correctly estimated and some

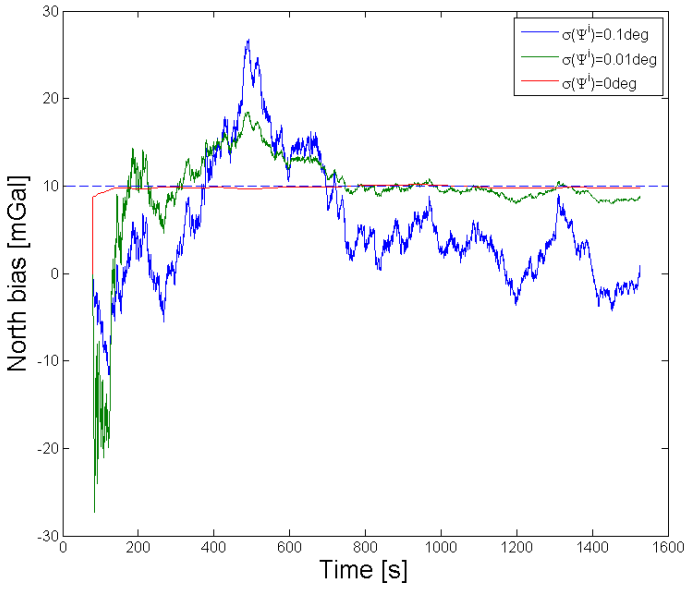

Figure 5.7: The estimated y-accelerometer bias for different accuracies of the GPS-attitude observations. The normal dataset has an accuracy of 0.1 deg. The true y-acc. bias is shown in the blue dashed line.

source of additional information is required.

With a real dataset Glennie (1999) noticed that the accelerometer bias was not constant, or even linear in time. It was, in fact, a non-linear parameter, and to alleviate this problem the author proposed a *crossover adjustment*. A crossover adjustment can be applied to a flight path consisting of several segments which intersect themselves with any other at least two times. A simple illustration of a possible flight path is given in Figure 5.8. The crossover adjustment means that a bias and slope are considered for each straight segment. Two segments intersecting at a crossover point must yield the same gravity anomaly value, since it does not change with time. All the crossover points provide enough constrains to compute the bias and slope of each segment of the full flight path. By subtracting these computed terms the full flight path is made *self-consistent*, meaning that two different segments will yield the same gravity disturbance at the crossovers. This technique reduces the impact of a possible non-linearity of the accelerometer bias. This kind of crossover adjustment can be seen as fitting the computed gravity disturbance to an arbitrary plane in the region which then can be related to the absolute gravity field with at least three ground measurements of the absolute gravity field.

To apply this crossover adjustment to the specific case of our simulations, notice that the bias in the accelerometer is constant and this fact simplifies the complexity of the adjustment. With a constant bias there is no need to compute a slope for

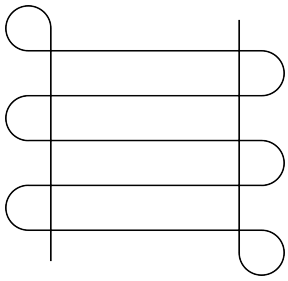

Figure 5.8: Example of self intersecting flight path required for a crossover adjustment

each segment or any crossover points, because all the segments will have the same bias value; Only one ground observation (e.g., from an absolute gravimeter) is then required to observe the real bias. This is how the accelerometer bias is assumed to be determined in the simulations, and despite looking like an over-simplification, this is a direct consequence of a crossover adjustment with the assumption of a constant bias.

Bruton (2000) proposes an alternative way of correcting the low-frequency errors in the strapdown system. The author noticed that the accelerometer biases, despite being hard to describe in the time domain, are confined to the very low frequency part of the spectrum, i.e., half-wavelengths bigger than 200 km. In that sense, using a high-pass filter above this region should conceptually remove all the errors in this area. This would yield a relative gravity field which could be related to the absolute one, once again using a crossover adjustment or even using a global geopotential model, which, with recent gravity missions, are expected to achieved the required accuracy in this low frequency region (Sneeuw et al., 2002). This implementation is attractive but would not bring any advantage to the current simulations where the bias is actually only a constant. It is then left as a recommendation for further investigation.

At this point, the high-frequency errors have been removed with the low-pass filtering depicted in Section 5.1 and the low-frequency errors of the INS have been corrected above. The gravity disturbance vector can now be computed.

5.4 Computed Gravity Disturbance Vector

By subtracting the GPS acceleration and IMU specific-force measurements in the i-frame, as seen in equation Eqn. 1.6, the gravity disturbance vector is computed. It is then rotated to the navigation frame and the resulting $\Delta\hat{\mathbf{g}}^n$ is plotted in Figure 5.9. In this plot the real gravity disturbance is depicted as the black line and in Figure 5.10 the difference between the computed and the real gravity disturbance vectors is plotted. This is the error of the strapdown airborne gravimetry system.

The standard deviations of the error in the gravity disturbance are presented in Table 5.3. The values of the perfect dataset are very small and are due to small

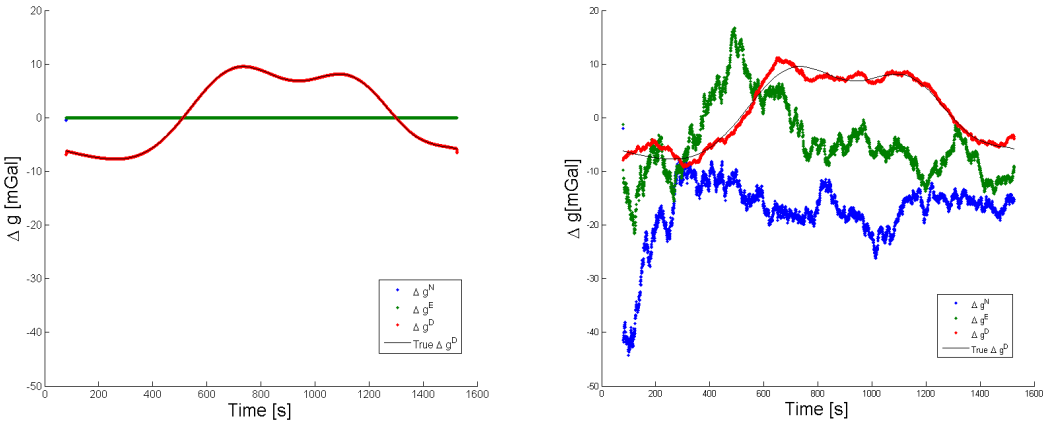

(a) Perfect Dataset (b) Normal Dataset

Figure 5.9: The computed gravity disturbance vector for the perfect dataset (a) and the normal dataset (b).

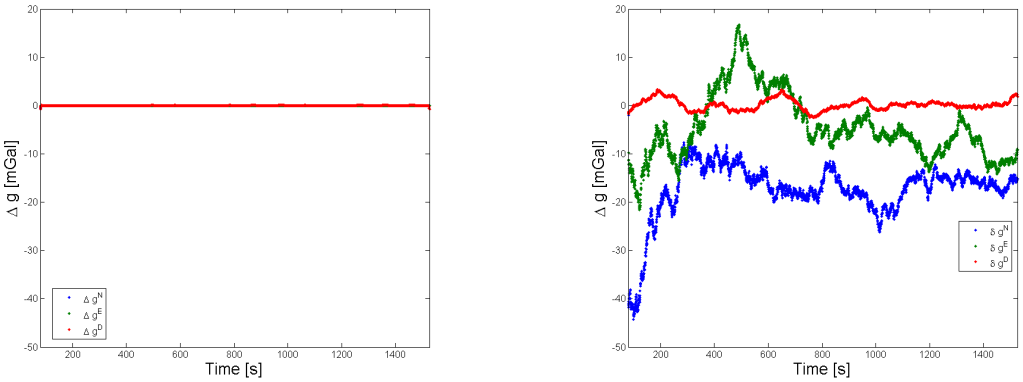

(a) Perfect Dataset (b) Normal Dataset

Figure 5.10: The error in the computed gravity disturbance vector for the perfect dataset (a) and the normal dataset(b).

Table 5.3: Standard deviations of the computed gravity disturbance for the normal and perfect datasets.

Description	RMS($\Delta\mathbf{g}^n$) [mGal]		
	N	E	D
Perfect	0.006	0.000	0.011
Normal	16.355	8.949	1.259

numerical errors in the integration of the attitude and the transformation matrices.

While this specific simulation yielded 1.259 mGal accuracy (in the vertical channel), the average result of nine different simulations places the performance of the GAIN strapdown system at 1.4 mGal with 2 Km resolution for scalar gravimetry. This is in line with the results claimed by Bruton (2000) with 1.5 mGal at 2km wavelength, and in a more recent field test Studinger et al. (2008) which show results between 0.9-1.4 mGal at 5 Km resolution.

5.5 Sensitivity of the strapdown system to different measurement accuracies.

In the following sections the sensitivity of the strapdown system accuracy is evaluated against variations in the accuracy of each measuring subsystem, namely: accelerometer, gyro, GPS positioning and attitude. This is useful to determine which of the mentioned devices constitutes the 'bottleneck' that limits the performance of the strapdown system. Additionally, any possible improvements in the performance of e.g., GPS positioning, can be linked to an improvement of the overall system accuracy.

The discussion in the following sections is divided between the vertical and the horizontal channels as they are quite different in nature and have different sensitivities as will be seen in the following sections. When the term scalar gravimetry is used, it refers to the vertical channel, and vector gravimetry refers to all three components of the gravity disturbance vector.

5.5.1 Impact of Accelerometer Accuracy

Description	$\sigma(\boldsymbol{\mu}_a)$ [mGal]	RMS($\Delta\mathbf{g}^n$) [mGal]		
		N	E	D
2x worse INS Acc	140	16.361	9.122	2.484
Normal	70	16.355	8.949	1.259
2x better INS Acc	35	16.416	8.845	0.666
5x better INS Acc	14	16.594	8.945	0.356
10x better INS Acc	7	16.688	9.063	0.288
Perfect Accelerometers	0	16.781	9.221	0.264

- The vertical component is very sensitive to accelerometer accuracy and between 2 and 5 times better accuracy the results cross the 0.5 mGal accuracy level. It seems the accelerometer noise is the dominant error source for scalar airborne gravimetry.

- Increasing the accuracy of the accelerometers does not significantly improve the horizontal components because most of the error is due to the uncorrected biases and not the actual noise of the accelerometers.

5.5.2 Impact of Gyro Accuracy

Description	$\sigma(\boldsymbol{\mu}_g)$ [°/s]	RMS($\Delta\mathbf{g}^n$) [mGal]		
		N	E	D
2x worse Gyros	5.90×10^{-3}	16.436	9.017	1.259
Normal	2.95×10^{-3}	16.355	8.949	1.259
2x better Gyros	1.48×10^{-3}	16.329	8.926	1.259
5x better Gyros	0.59×10^{-3}	16.329	8.924	1.259
10x better Gyros	0.30×10^{-3}	16.339	8.928	1.259
Perfect Gyros	0	26.118	33.261	1.258

- The vertical component is not sensitive to changes in the gyros accuracy. The roll and pitch angles are very observable and they are always kept by the Kalman filter within a region where they do not affect the vertical component of the gravity disturbance.

- The accuracy in the gyros measurements does not affect the horizontal components of the gravity disturbance. The major part of the error in these channels is owed to the uncorrected bias in the corresponding accelerometers. In the performed simulation, as stated in Section 5.2.2, the lateral biases are indistinguishable from the tilt error. One could think that an improvement in the gyros accuracy would improve this situation however, this is not the case. The gyros measurements provide only a reference between epochs, the change in attitude between two epochs rather than an absolute observation of the attitude. Therefore improving the gyros measurements doesn't improve the information of the absolute attitude and no improvement is obtained in the estimation of the lateral biases. Notice that the results are slightly different for the dataset where the gyros measurements are perfect because, in this extreme situation, the GPS-attitude observations are completely disregarded by the Kalman filter which aggravates the horizontal bias estimation.

5.5.3 Impact of GPS position accuracy

Description	$\sigma(\boldsymbol{\mu}_G)$ [cm]	RMS($\Delta\mathbf{g}^n$) [mGal]		
		N	E	D
2x worse GPS pos.	2	16.447	9.028	1.329
Normal	1	16.355	8.949	1.259
2x better GPS pos.	0.5	16.318	8.917	1.243
5x better GPS pos.	0.2	16.303	8.905	1.240
10x better GPS pos.	0.1	16.300	8.902	1.240
Perfect GPS positioning	0	16.298	8.900	1.241

- The vertical component is slightly sensitive to the GPS position accuracy but already at the normal dataset the results stabilize. This indicates the accelerometers introduce the major component of the noise in the results.

- The horizontal components necessary for vector gravimetry are not improved by using better GPS positioning. Most of the error in the horizontal components is due to the uncompensated accelerometer biases.

5.5.4 Impact of GPS attitude accuracy

Description	$\sigma(\boldsymbol{\mu}_\psi)$	RMS($\Delta\mathbf{g}^n$)		
		N	E	D
No Observations		39.379	9.178	1.260
2x worse GPS att.	0.2°	28.336	9.622	1.260
Normal	0.1°	16.355	8.949	1.259
2x better GPS att.	0.05°	5.731	7.660	1.257
5x better GPS att.	0.02°	6.196	4.663	1.256
10x better GPS att.	0.01°	4.532	2.567	1.255
Perfect GPS attitude	0°	1.443	1.419	1.256

- For the vertical component of the gravity disturbance the GPS attitude observations are not helpful and they do not improve the performance of the system along this direction.

- For the horizontal channels the GPS-attitude observations are critical to correctly estimate the gravity disturbance. They provide the absolute information that allows the decoupling between the horizontal biases and the tilt of the platform, but they must be at least an order of magnitude better before the accuracy of the solution approximates that of the vertical channel enabling vector gravimetry.

5.6 Sensitivity to Accelerometer and DGPS accuracies

It can be noticed from the above results that the accuracy of the vertical component of the gravity disturbance vector is mostly sensitive to the GPS position accuracy and the IMU accelerometer accuracy. With the goal of obtaining an airborne gravimetry system with a 0.5 mGal accuracy it is important to predict where will improvements in any of these two systems maximize the overall accuracy of the system. With this in mind, a number of simulations with varying parameters was run to yield Figure 5.11. In this figure, the axes are non-linear and point towards the direction of improvement in the accuracy of each system. The predicted performance of the GAIN strapdown system is marked by the red star and each black dot represents one simulation performed. The surface is interpolated from the results of all the simulations performed, and marked with a green band is the border of the sub-0.5 mGal accuracy region.

As expected, it can be seen that the shortest path towards the 0.5 mGal region corresponds to an improvement by a factor of three in the accuracy of the QA3000

accelerometer measurements. Improvements in the GPS positioning do not significantly improve the results, since the accelerometers are the dominant source of the error.

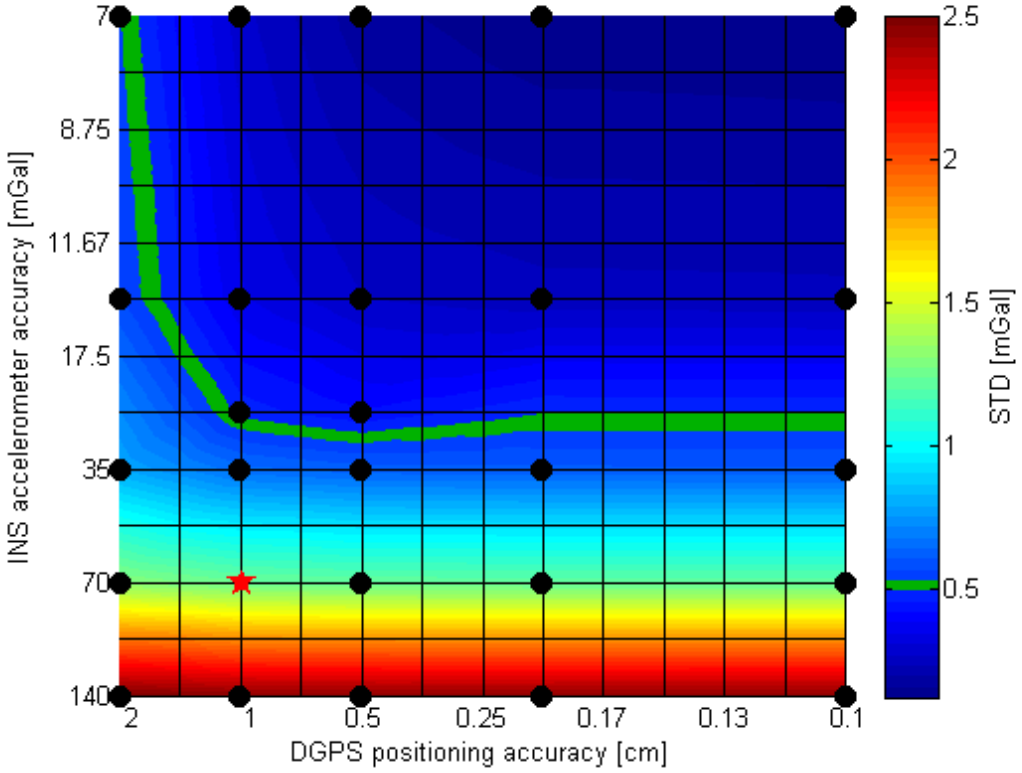

Figure 5.11: Estimated accuracy (1σ) of the strapdown system as a function of accelerometer and DGPS accuracies.

5.7 Achieving 0.5 mGal accuracy

In the previous section it has been seen that a factor improvement of three is required in the IMU accelerometers accuracy before the desired 0.5 mGal accuracy can be achieved. This might be technologically impossible or extremely expensive in the near future and alternative ways of improving the solution can be though about.

Glennie (1999) studied multi-sensor configurations as a way to improve the computed solution. With the measurements of N *independent* devices the accuracy of the combined solution should increase by a factor of $\sqrt{N}$. This assumption is valid only in the scenario where redundant sensors are independent and do not share any common errors which are not reduced in the combination.

Table 5.4: Improvement in the accuracy of the system with increasing number of passes over the same region.

#Passes	$\sigma(\Delta\mathbf{g}^D)$ [mGal]
1	1.39
2	1.00
4	0.79
9	0.46

Using multiple GPS receivers would then result in a more accurate GPS solution, but GPS receivers onboard the same platform typically suffer from common errors (e.g., ionospheric and tropospheric delays) and in reality the improvements could be very small. Additionally, as seen in the previous chapter, an increase in the accuracy of the GPS solution would not significantly increase the performance of the system.

A multiple-IMU architecture would become rapidly very expensive and easily result in very complex system before any significant improvements in the solution would be noticed. Both these kinds of redundancies (IMU and GPS) were analyzed in the same publication with data from a real campaign using two GPS and two IMU systems, where the author concludes that the improvement was negligible with any of these combinations.

Instead of using multi-sensor systems, one can think of a multi-pass system where several passes are made above the same region, and in the combination the overall results would increase by the same factor. Since the gravity signal does not change (significantly) within campaign time spans this would be a feasible technique of improving the accuracy at an increased operational cost per area of survey. This technique has been applied successfully in Studinger et al. (2008). This is also demonstrated with the simulated system and the results are gathered in Table 5.4

An additional way of increasing the accuracy of the system is to fly at lower speed. The low-pass filter cutoff frequency is defined by the product of the resolution and the aircraft speed, $f = \frac{v}{\lambda}$. For the same resolution, λ, if the vehicle speed is reduced, then the cutoff frequency of the low-pass filter can be equally reduced to remove a higher portion of noise from the data. A few simulations were run with different cutoff frequencies until the accuracy of the computed gravity reached 0.5 mGal. This happened at a cutoff frequency of 0.005 Hz which, aiming for a 2 km resolution, places the maximum vehicle speed at 72 km/hr (instead of the 220 km/hr used as nominal value for the Cessna).

5.8 Full flight path

To close the results section a survey campaign was simulated to measure the gravity disturbance vector over a larger target area. The $\approx 100 \times 100$ km region marked in

Figure 5.12a was chosen and an artificial flight path was generated to survey the area. The selected region contains two very large features with high and low values. Additionally, it also contains a smaller feature in the top-right corner. All this can be seen in Figure 5.12b, where a zoom of the region is shown along with the chosen flight path. The flight path itself consists of 10 straight paths, 10 km apart, with half-circles connecting them. The profile was flown with a constant 220 km/hr speed at a constant altitude of 2 km. During the straight flight segments, the airplane is at steady leveled flight in the same conditions as stated in the beginning of this section. At the start of the turn the airplane rotates around its roll axis with constant speed 0.5 °/s for 10 seconds reaching the bank angle of 5 °. During the turn, the yaw axis of the airplane is also appropriately rotated such that the airplane is always facing the direction tangent to the trajectory. At the end each turn the airplane returns to the leveled flight state.

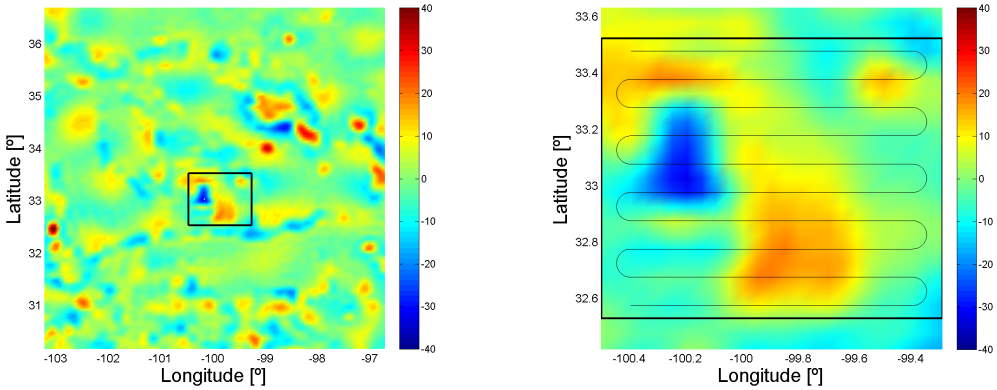

(a) Gravity Disturbances at 2 km height

(b) Trajectory of the simulated flight

Figure 5.12: Gravity disturbances dataset in panel (a) and simulated flight path over the selected region in panel (b).

The results obtained in the simulation are plotted in Figure 5.13. The computed gravity disturbance map has a resolution of 10 km in the across track direction due to the spacing between consecutive lines. In the along-track direction the resolution is improved to 2 km due to the cutoff frequency of the filter. This explains some elongation of the errors along the across-track component. In this specific simulation, the standard deviation of the errors in the computed gravity disturbance was 1.452 mGal.

The implemented simulator performed well in this more realistic scenario. The presence of small and large, high an low features did not have an impact on the recovered gravity anomaly.

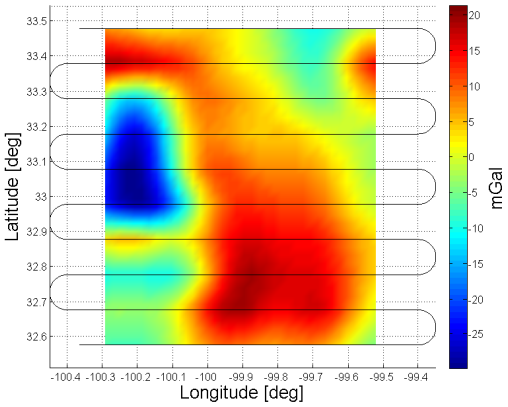

(a) True gravity disturbance

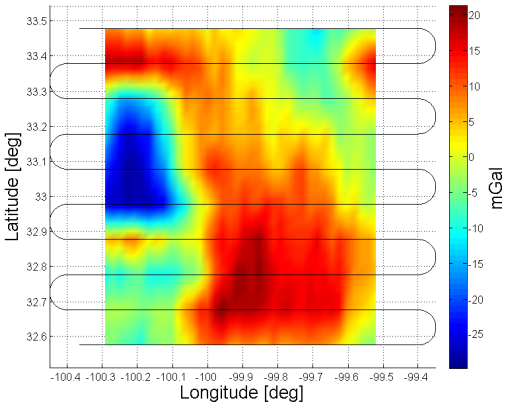

(b) Computed gravity disturbance

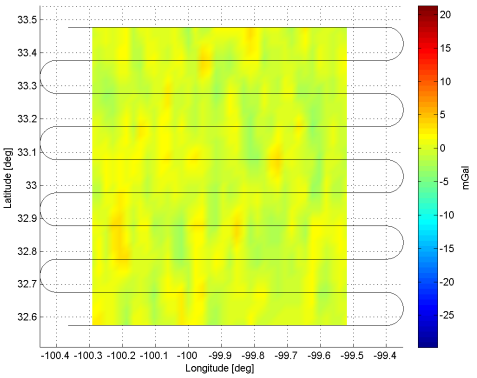

(c) Error with same scale

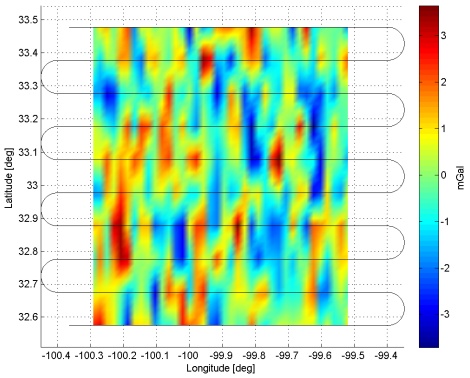

(d) Error with auto scale

Figure 5.13: Results of the full campaign.

Conclusions and Recommendations

6

The purpose of this thesis work was to assess the accuracy of the GAIN strapdown airborne gravimetry system, currently under development, and its applicability high-resolution applications of airborne gravimetry data. For this purpose, the inertial sensors acquired by the GAIN project have been calibrated and the knowledge gathered about them was transported to the simulations domain, where the performance of the complete system has been measured. In this chapter the main results and recommendations are summarized, which directly address the research questions outlined in Chapter 1.

6.1 Calibration

- An initial calibration of one of the accelerometers was performed and the scale factor was observed to be within specifications. It was also observed that the accelerometers are very sensitive to small variations in the temperature.
- A calibration of the gyros was also performed where the instrument was found to be within product specifications.

6.2 Simulation

To obtain the results of this thesis, a strapdown airborne gravimetry simulator was implemented. It was used to,

- Predict the expected accuracy of the GAIN strapdown system under ideal conditions.
- Investigate the sensitivity of the system's accuracy to different precisions in each measurement.
- Investigate the impact of aircraft velocity on the accuracy of the system.
- Investigate the impact of multiple passes over the survey area.

6.3 Results

A realistic model of the GAIN strapdown airborne gravimetry system has been simulated using the expected performance of the inertial sensors, as seen in the calibrations. The following results were obtained,

- The predicted accuracy of the GAIN strapdown system is 1.4 mGal at 2 km resolution.
- The target accuracy of 0.5 mGal at 2 km can be achieved by improving the accuracy of the inertial acceleration by a factor of three. This can be accomplished through one of the following:
    1. Reducing the aircraft speed from 220 km/hr to 72 km/hr. Whether this is possible for the Cessna Citation II or not was not investigated.
    2. Taking a minimum of 9 passes over each surveyed area. Repeated passes over the same area reduce the uncertainty of the measurements.
    3. Improving the accelerometer accuracy by a factor three.
    4. Any sufficient combination of the above three.
- Under ideal conditions, GPS-attitude measurements do not improve the results of scalar airborne gravimetry.
- Vector gravimetry requires improved observability of the horizontal biases. This can be achieved by,
    1. Improving the accuracy of the GPS-attitude measurements by at least an order of magnitude.
    2. Performing special maneuvers with the SINS to decouple the horizontal biases from the tilt error.
    3. Any sufficient combination of the above two.

6.4 Recommendations

Some recommendations can be made to improve the results obtained in this thesis. The calibration setup of the gyros is complex and the two synchronized data loggers should be reduced to a single data logging system to avoid delays and systematic errors. Additionally, the implemented GPS system is extremely simplistic and more sophisticated models can be introduced to take into account atmospheric delays, loss of lock, cycle slips, multipath and many other phenomena that might have an impact in the accuracy of the system.

Since the IMU system is currently under development, the knowledge of the hardware was far from complete. As soon as the electronics that will be used in the IMU are finished, the accelerometers can be calibrated at the sampling frequency in which they will operate. This will allow a more realistic characterization of the noise in the instruments, which then can be included in the simulations.

A thorough temperature calibration has to be performed for the accelerometers and gyros. It is necessary to know if any kind of temperature control over the accelerometers is necessary, to obtain sufficiently stable measurements during the time span of typical airborne surveys.

No calibrations have been done with the complete IMU system and therefore this important task still needs to be completed. As soon as the electronics are ready and the individual sensors have been calibrated, they can be assembled in the IMU and further calibrations are then required. These regard the placement of each instrument inside the IMU, and the placement of the IMU inside the Cessna Citation II aircraft. Furthermore the calibration process should be automated, such that it can be rapidly used before and after any campaign. The calibration process of the IMU should yield, besides the individual sensor parameters (biases and scale factors) presented in this thesis, additional ones regarding the placement of the inertial sensors within the IMU casing: the misalignment of the each instrument's sensitive axis inside the IMU has to be known and compensated for; the positions of the accelerometers inside the IMU have to be accurately known to account for lever-arm effects. A lever-arm effect is a consequence of the accelerometer triad geometry. Since not all the accelerometers can be placed at the origin of the IMU frame, a rotation over the e.g., y-axis will create an acceleration measured by the x- and z-axis accelerometers which must be compensated.

6.5 Future Work

This thesis work has set the foundations for additional studies regarding airborne gravimetry and as such it leaves many open possibilities for future work. The airborne gravimetry simulator can also be used to,

- Investigate the impact of airplane dynamics on the accuracy of a vector gravimeter system. Airplanes exhibit typical flight dynamic modes (dutch roll, phugoid, etc.) in which the aircraft motion excites frequencies that can overlap with the region of interest. This is seen in published results (e.g., Kwon and Jekeli (2001)), where the aircraft dynamics are evidently influencing the horizontal components of the computed gravity disturbance.
- Investigate the impact of the trajectory on parameter observability and on the accuracy of the system. Rotating the aircraft relative to the navigation frame is an efficient way of exposing the biases in the horizontal accelerometers. However increased rotation dynamics degrade the performance of the attitude computation.
- Investigate the impact of the instruments sampling rate on the accuracy. A higher sampling rate provides a better description of the continuous kinematic state of the aircraft at the cost of higher noise levels in the measurements.
- Investigate the observability and the importance of estimating the scale factors in the accelerometers and gyros for typical airborne gravimetry flight paths.

Of course many improvements are still required for more realistic simulations; the used gravity disturbance model was limited to 10 km resolution. This can be

expanded at least up to the system resolution of 2 km. Furthermore the gravity disturbances were pre-computed at the target altitude of 2 km. In reality, the power in the higher frequencies of the gravity field is rapidly attenuated with altitude. A more realistic model would take this effect into account, which would enable an investigation on the impact of altitude in the system's accuracy. At the same time, the simulator should be able to downward continue the computed gravity disturbance to allow the comparison of results between flights at different altitudes.

Bibliography

Alberts, B. (2009). *Regional gravity field modelling using airborne gravimetry data*. Ph. D. thesis, Technical University of Delft.

Alberts, B. A., B. C. Gunter, A. Muis, Q. P. Chu, G. Giorgi, L. Huisman, P. J. Buist, C. C. J. M. Tiberius, and H. Lindenburg (2010). Correcting strapdown GPS/INS gravimetry estimates with GPS attitude data. In *Gravity, Geoid and Earth Observation*, Volume Vol. 135 of *International Association of Geodesy Symposia*, pp. 93–100. Springer Berlin Heidelberg.

Brown, R. G. and P. Y. C. Hwang (1997). *Introduction to Random Signals adn Applied Kalman Filtering*. John Wiley & Sons.

Brozena, J. M. (1984). A preliminary analysis of the NRL airborne gravimetry system. *Geophysics 49*(7), 1060–1069.

Bruton, A. M. (2000). *Improving the Accuracy and Resolution of SINS/DGPS Airborne Gravimetry*. Ph. D. thesis, University of Calgary.

Bruton, A. M., C. L. Glennie, and K. P. Schwarz (1999). Differentiation for high-precision gps velocity and acceleration determination. *GPS Solutions Vol. 2, No. 4*, 7–21.

Chapra, S. and R. Canale (2010). *Numerical Methods for Engineers*. Mcgraw Hill.

Fizoptika (2010). Fiber optic rotation sensor VG951. Technical report, Fizoptika.

Förste, C., R. Schmidt, R. Stubenvoll, F. Flechtner, U. Meyer, R. König, H. Neumayer, R. Biancale, J. Lemoine, S. Bruinsma, S. Loyer, F. Barthelmes, and S. Esselborn (2008, June). The GeoForschungsZentrum Potsdam/Groupe de Recherche de Gèodésie Spatiale satellite-only and combined gravity field models: EIGEN-GL04S1 and EIGEN-GL04C. *Journal of Geodesy 82*, 331–346.

Glennie, C. (1999). *An Analysis of Airborne Gravity by Strapdown INS/DGPS*. Ph. D. thesis, University of Calgary.

Glennie, C. and K. P. Schwarz (1999). A comparison and analysis of airborne gravimetry results from two strapdown inertial/dgps systems. *Journal of Geodesy Volume 73, No. 6*, 311–321.

Gustafsson, F., F. Gunnarsson, N. Bergman, U. Forssell, J. Jansson, R. Karlsson, and P.-J. Nordlund (2002). Particle filters for positioning, navigation, and tracking. *IEEE Transactions on Signal Processing Vol. 50, No. 2*, 425–437.

Honeywell (2010). Q-flex QA3000 accelerometer. Technical report, Honeywell.

ICRS (2010, January). ICRS product center. http://hpiers.obspm.fr/icrs-pc/.

IERS (2010, July). The international terrestrial reference system (ITRS). http://www.iers.org/IERS/EN/DataProducts/ITRS/itrs.html.

Jekeli, C. (1994). Airborne vector gravimetry using precise, position-aided inertial measurement units. *Bulletin Géodésique Vol.69*, 1–11.

Jekeli, C. (2001). *Inertial Navigation Systems with Geodetic Applications*. Walter de Gruyter.

Jekeli, C. and R. Garcia (1997). Gps phase accelerations for moving-base vector gravimetry. *Journal of Geodesy 71*, 630–639.

Jekeli, C. and J. H. Kwon (1999). Results of airborne vector (3-d) gravimetry. *Geophysical Research Letters Vol. 26, No. 23*, 3533–3536.

Kalman, R. E. (1960). A new approach to linear filtering and prediction problems. *Journal of Basic Engineering 82 (Series D)*, 35–45.

Kaula, W. (1966). *Theory of Satellite Geodesy: Applications of Satellites to Geodesy*. Blaisdell Pub. Co.

Kennedy, S. L. (2002). Acceleration estimation from gps carrier phases for airborne gravimetry. Master's thesis, University of Calgary.

King, A. (1998). Inertial navigation: Forty years of evolutio. *GEC Review vol. 13, no. 3*, 140–149.

Kreye, C. and G. W. Hein (2003). Improving the accuracy and resolution of sins/dgps airborne gravimetry.

Kuipers, J. (1999). *Quaternions and rotation Sequences: a Primer with Applications to Orbits, Aerospace, and Virtual Reality*. Princeton University Press.

Kwon, J. H. and C. Jekeli (2001). A new approach for airborne vector gravimetry using gps/ins. *Journal of Geodesy Vol 74, No. 10*, 690–700.

LaCoste, L., J. Ford, R. Bowles, and K. Archer (1982). Gravity measurements in an airplane using state-of-the-art navigation and altimetry. *Geophysics 47*(5), 832–838.

Lemoine, F., S. Kenyon, J. Factor, R. Trimmer, N. Pavlis, D. Chinn, C. Cox, S. Klosko, S. Luthcke, M. Torrence, Y. Wang, R. Williamson, E. Pavlis, R. Rapp, and T. Olson (1998). The development of the joint nasa gsfc and nima geopotential model egm96. tech. rep. nasa/tp-1998-206861. Technical report, NASA Goddard Space Flight Center, Greenbelt, MD, USA.

Li, X. (2007). *Moving Base INS/GPS Vector Gravimetry on a Land Vehicle*. Ph. D. thesis, The Ohio State University.

Lizarralde, F. and J. Wen (1996). Attitude control without angular velocity measurement: A passivity approach. *IEEE Transactions on Automatic Control Vol. 41, No. 3*, 468–472.

Mangold, U. (1997). Theory and performance prediction for continous vector gravimetry based on a dgps augmented rate bias inertial navigation system and a star tracker. *Navigation: Journal of The Institude of Navigation Vol. 44, No. 3*, 329–345.

Meyer, U., G. Boedecker, and H. Pflug (2003). Angel - airborne navigation and gravimetry ensemble & laboratory - introduction and first airborne tests. Technical report, GeoForschungsZentrum Potsdam.

Mohamed, A. H. and K. P. Schwarz (1999). Adaptive kalman filtering for ins/gps. *Journal of Geodesy 73*, 193–203.

Moritz, H. (1992). Geodetic reference system 1980. *Bulletin Geodesique Vol. 66-2*, 187–192.

Nettleton, L. L., L. LaCoste, and J. C. Harrison (1960). Tests of an airborne gravity meter. *Geophysics 25*(1), 181–202. One of the first attempts at airborne gravimetry.

Rose, R. and R. Nash (1972, april). Direct recovery of deflections of the vertical using an inertial navigator. *Geoscience Electronics, IEEE Transactions on 10*(2), 85 –92.

Rummel, R. (2003). How to climb the gravity wall. *Space Science Reviews Vol. 108, No.1/2*, 1–14.

Rummel, R., G. Balmino, J. Johannessen, P. Visser, and P. Woodworth (2002). Dedicated gravity field missions–principles and aims. *Journal of Geodynamics 33*(1-2), 3 – 20. A paper describing the three gravity dedicated missions.

Salychev, O., V. Voronov, M. Cannon, R. Nayak, and G. Lachapelle (2000). Low cost ins/gps integration - concepts and testing. *Navigating into the New Millennium; Proceedings of the Institute of Navigation National Technical Meeting, Anaheim, CA; UNITED STATES;*, 98–105.

Salychev, O. S. (1998). *Inertial Systems in Navigation and Geophysics*. Bauman MSTU Press.

Savitzky, A. and M. J. E. Golay (1964). Smoothing and differentiation of data by simplified least squares procedures. *Analytical Chemistry 36*(8), 1627–1639.

Schwarz, K. P. and Z. Li (1997). *Geodetic Boundary Value Problems in View of the One Centimeter Geoid*, Volume Volume 65 of *Lecture Notes in Earth Sciences*, Chapter An introduction to airborne gravimetry and its boundary value problems, pp. 312–358. Springer Berlin / Heidelberg.

Senobari, M. (2010). New results in airborne vector gravimetry using strapdown ins/dgps. *Journal of Geodesy Vol. 84, No. 5*, 277–291.

Sneeuw, N., J. van den IJssel, R. Koop, P. Visser, and C. Gerlach (2002). Validation of fast pre-mission error analysis of the goce gradiometry mission by a full gravity field recovery simulation. *Journal of Geodynamics 33*(1-2), 43 – 52.

Studinger, M., R. Bell, and N. Frearson (2008). Comparison of airgrav and gt-1a airborne gravimeters for research applications. *Journal of Geophysics Vol. 73, No. 6*, 151–161.

Tapley, B. (2004). *Statistical Orbit Determination*. Oxford Oxfordshire: Oxford University Press.

Teunissen, P. (2006). The LAMBDA method for the gnss compass. *Artificial Satellites Vol. 41, No.3*, 89–103.

Thompson, L. and L. LaCoste (1960). Aerial gravity measurements. *Journal of Geophysical Research 65(1)*, 305–322.

Wang, J. J., J. Wang, D. Sinclair, and L. Watts (2006). A neural network and kalman filter hybrid approach for gps/ins integration.

Wei, M. and K. P. Schwarz (1998). Flight test results from a strapdown airborne gravity system. *Journal of Geodesy 72*, 323–332.

Wenzel, G. (1998). Ultra high degree geopotential mod-els gpm98a, b and c to degree 1800. In *Proc. Joint Meeting International Gravity Commission and International Geoid Commission, 7/12 September 1998, Trieste, Italy*.

Kalman Derivation

A

In this appendix we will establish the equivalence between

$$\mathbf{u} \equiv \mathcal{E}(\mathbf{x}|\mathbf{y}) = P\left(H^T R^{-1}\mathbf{y} + P_0^{-1}\mathbf{u}_0\right) \tag{A.1}$$

$$P \equiv \mathrm{cov}(\mathbf{x}|\mathbf{y}) = \left(P_0^{-1} + H^T R^{-1} H\right)^{-1} \tag{A.2}$$

and

$$\mathbf{u} = \mathbf{u}_0 + K(\mathbf{y} - H\mathbf{u}_0) \tag{A.3}$$

$$P = (I - KH)P_0 \tag{A.4}$$

$$K \equiv P_0 H^T \left(H P_0 H^T + R\right)^{-1} \tag{A.5}$$

To prove the equivalence between both forms of the filtering step it is necessary to prove that:

1. (A.1) is equivalent to (A.3)
2. (A.2) is equivalent to (A.4)

Starting with #1

$$\mathbf{u} = P\left(H^T R^{-1}\mathbf{y} + P_0^{-1}\mathbf{u}_0\right)$$

add and subtract $PH^T R^{-1} H\mathbf{u}_0$,

$$\mathbf{u} = PP_0^{-1}\mathbf{u}_0 + PH^T R^{-1}\mathbf{y} + PH^T R^{-1} H\mathbf{u}_0 - PH^T R^{-1} H\mathbf{u}_0$$

$$\mathbf{u} = \underbrace{P(P_0^{-1} + H^T R^{-1} H)}_{=I}\mathbf{u}_0 + PH^T R^{-1}(\mathbf{y} - H\mathbf{u}_0)$$

where equation Eqn. A.2 is used and finally,

$$\mathbf{u} = \mathbf{u}_0 + PH^T R^{-1}(\mathbf{y} - H\mathbf{u}_0)$$

The above equation is equivalent to (A.3) if and only if $PH^T R^{-1} = K$. That can

be shown manipulating both sides of equation Eqn. A.2,

$$
\begin{aligned}
&P^{-1} = P_0^{-1} + H^T R^{-1} H && [\,] \times P_0 H^T \\
&P^{-1} P_0 H^T = (P_0^{-1} + H^T R^{-1} H) P_0 H^T \\
&P^{-1} P_0 H^T = H^T + H^T R^{-1} H P_0 H^T \\
&P^{-1} P_0 H^T = H^T R^{-1} (R + H P_0 H^T) && (H^T R^{-1})^{-1} \times [\,] \\
&(H^T R^{-1})^{-1} P^{-1} P_0 H^T = \underbrace{(H^T R^{-1})^{-1} H^T R^{-1}}_{=I} (R + H P_0 H^T) && [\,] \times (P_0 H^T)^{-1} \\
&R H^{T^{-1}} P^{-1} \underbrace{P_0 H^T (P_0 H^T)^{-1}}_{=I} = (R + H P_0 H^T)(P_0 H^T)^{-1} && [\,]^{-1} \\
&P H^T R^{-1} = P_0 H^T (R + H P_0 H^T)^{-1}
\end{aligned}
$$

and noticing the definition of K in Eqn. A.5, one can finally write

$$P H^T R^{-1} = K$$

thus proving the equivalence between both forms of the state vector equations.

The covariance matrix filtering equations still needs to be proven equivalent, as in #2, and this is done by showing that equation (A.4) leads to (A.2),

$$P = (I - KH) P_0$$

replacing K from equation (A.5)

$$
\begin{aligned}
&P = P_0 - P_0 H^T (H P_0 H^T + R)^{-1} H P_0 \\
&P = P_0 - P_0 \Big(H^{-1} (H P_0 H^T + R) H^{T^{-1}} \Big)^{-1} P_0 \\
&P = P_0 - P_0 \Big(P_0 + H^{-1} R H^{T^{-1}} \Big)^{-1} P_0
\end{aligned}
$$

bringing both terms to the same dividend,

$$P = P_0 \Big(P_0 + H^{-1} R H^{T^{-1}} \Big)^{-1} \Big(P_0 + H^{-1} R H^{T^{-1}} \Big) - P_0 \Big(P_0 + H^{-1} R H^{T^{-1}} \Big)^{-1} P_0$$

expanding the first term,

$$
\begin{aligned}
P = \underbrace{P_0 \Big(P_0 + H^{-1} R H^{T^{-1}} \Big)^{-1} P_0 - P_0 \Big(P_0 + H^{-1} R H^{T^{-1}} \Big)^{-1} P_0}_{=0} \\
+ P_0 \Big(P_0 + H^{-1} R H^{T^{-1}} \Big)^{-1} H^{-1} R H^{T^{-1}}
\end{aligned}
$$

$$
\begin{aligned}
P &= P_0\Big(P_0 + H^{-1}RH^{T^{-1}}\Big)^{-1}H^{-1}RH^{T^{-1}} \\
P &= \Big[\Big(H^{-1}RH^{T^{-1}}\Big)^{-1}\Big(P_0 + H^{-1}RH^{T^{-1}}\Big)^{-1}P_0^{-1}\Big]^{-1} \\
P &= \Big[H^T R^{-1} H \underbrace{P_0 P_0^{-1}}_{=I} + \underbrace{H^T R^{-1} H H^{-1} R H^{T^{-1}}}_{=I} P_0^{-1}\Big]^{-1} \\
P &= \Big[P_0^{-1} + H^T R^{-1} H\Big]^{-1}
\end{aligned}
$$

which finishes this demonstration.